Novel Nanostructured Metal Oxides for Efficient Solar Energy Conversion

by

Lite Zhou

A Dissertation

Submitted to the Faculty

of the

WORCESTER POLYTECHINC INSTITUTE

in partial fulfillment of the requirements for the

Degree of Doctor of Philosophy

in

Materials Science and Engineering

March 19, 2019

APPROVED:

_____

Pratap M Rao, Advisor

Assistant Professor, Mechanical Engineering

_____

Richard D. Sisson Jr.

George F. Fuller Professor

Director, Manufacturing and Materials Engineering

Abstract:

Metal oxide materials could offer earth-abundant, non-toxic alternatives to existing light-absorber materials in thin-film photovoltaic and photoelectrochemical cells. However, efficiency of these devices based on existing metal oxides is typically low due to poor material properties. In this research, novel $Sb:SnO_2$ nanorod and nanotube electron collectors have been synthesized, investigated and were used to improve the photo-conversion efficiency of top-performing $BiVO_4$ photoelectrochemical cell. The performance of $Sb:SnO_2/BiVO_4$ photoanode achieved a new record for the product of light absorption and charge separation efficiencies ($\eta_{abs} \times \eta_{sep}$) of ~ 57.3% and 58.5% under front- and back-side illumination at 0.6 V_{RHE} and $Sb:SnO_2/BiVO_4$ PV cell achieved 1.22% solar power conversion efficiency. In addition, a new promising metal oxide material ($CuBiW_2O_8$) has been synthesized and its optoelectronic properties have been investigated to make photovoltaic cell which has potential to achieve over 30% solar power conversion efficiency.

ACKNOWLEDGEMENTS

Table of Contents

Chapter 1 Introduction

1.1 Energy and Environment Challenges

One of the main challenges facing humans in the twenty-first century is to supply the world's population with sufficient energy. The power consumption of the current (2017) global population of nearly 7.6 billion people is about 160,000 TWh (13.7 billion tons oil equivalent)[1], and these numbers are estimated to increase to ~9 billion and 300,000 TWh (26 billion tons oil equivalent) by 2050.[2, 3] Fossil fuels currently provide about 80% of our energy supply.[4] Even though the reserve of fossil fuels may still large enough to meet our energy demands for a few decades, another concern of using fossil fuels is the emission of CO_2 and its contribution to global warming. According to the State of the Climate in 2017 report from National Oceanic and Atmospheric Administration (NOAA) and the American Meteorological Society, a new high record of global atmospheric carbon dioxide was set in 2017 of 405.0 ± 0.1 ppm. Between 2016 and 2017, global annual mean carbon dioxide increased 2.2 ± 0.1 ppm. That was slightly less than the increase of 3.0 ppm between 2015 and 2016. In the latest report, the atmospheric CO_2 in January 2019 is 410.92 ppm, which is almost 3 ppm higher than in January 2018 (407.96 ppm).
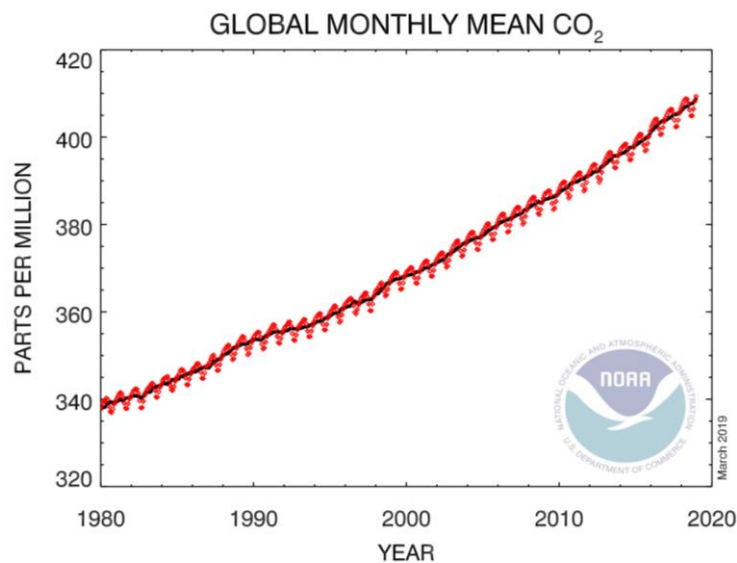
Figure 1. Global monthly average carbon dioxide concentration. (Last updated February 2019)[5]

Based on NOAA's global analysis, 2018 is the globe's fourth hottest year in NOAA's 139-year climate record, followed by 2016 (warmest), 2015 (second warmest) and 2017 (third warmest). The average global temperature during 2018 was 1.42 °F above the 20th-century average. The globally averaged sea surface temperature was 1.19 °F above average, while the land surface temperature was 2.02 °F above average, both the fourth highest on record. Figure 2 shows the land & ocean temperature percentiles of 2018.[6] Today, sustainable energy only provides ~10% of energy supply.[4] In order to decrease fossil fuels usage, CO_2 emission, and slow down the globe warming, a large-scale transition from traditional fossil fuels to new and sustainable energy is necessary.
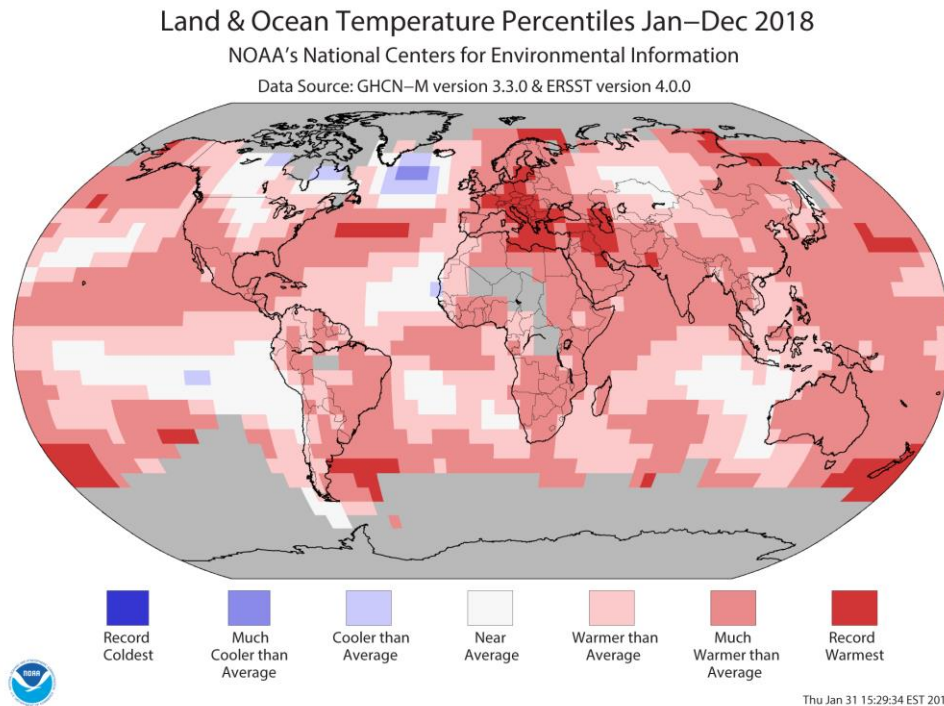
Figure 2. Land & Ocean Temperature Percentiles Jan-Dec 2018.[6]

1.2 Sustainable Energy Sources

Sustainable energy is one which can meet the growing demand of today's people without compromising the planet's ecosystem and the demand of the people that would require it in

future. There are many kinds of sustainable energy sources, and the most promising and widely used sustainable energy sources are wind energy, hydroelectric energy, tidal energy, geothermal energy, biomass energy and solar energy.

1.2.1 Wind Energy

Wind energy is the use of mechanical power in air flow to generate electricity. Compared to burning fossil fuels, wind energy is renewable, clean, and produces no greenhouse gas emissions during operation. Wind energy is also widely distributed and can be efficiently collected in wind farms with hundreds of wind towers. Figure 3 shows an image of wind farm. According to World Wing Energy Association (WWEA), after 10.8 % growth in 2017, global wind power capacity reaches 600 GW in 2018.[7] Yearly wind energy production grew 17% reaching 4.4% of worldwide electric power usage, and providing 11.6% of the electricity in the European Union.

Figure 3. Image of wind farm.[8]

1.2.2 Hydroelectric Energy

Hydroelectric energy is the electric energy generated by falling water or fast-running water. Usually, a dam is used to store water, collect hydropower, and generate hydroelectric energy. Gravity causes water to fall through a turbine propeller inside the dam, which is turned by the moving water. The shaft from the turbine goes up into the generator, which produces the electric energy. The cost of hydroelectricity is relatively low, making it a competitive source of renewable electricity. According to Renewables 2016 Global Status Report, in 2015, Hydroelectric energy generated 16.6% of the world's total electricity and 70% of all renewable electricity, and was expected to increase about 3.1% each year for the next 25 years. Figure 4 shows the dam and schematic images of hydroelectric energy.
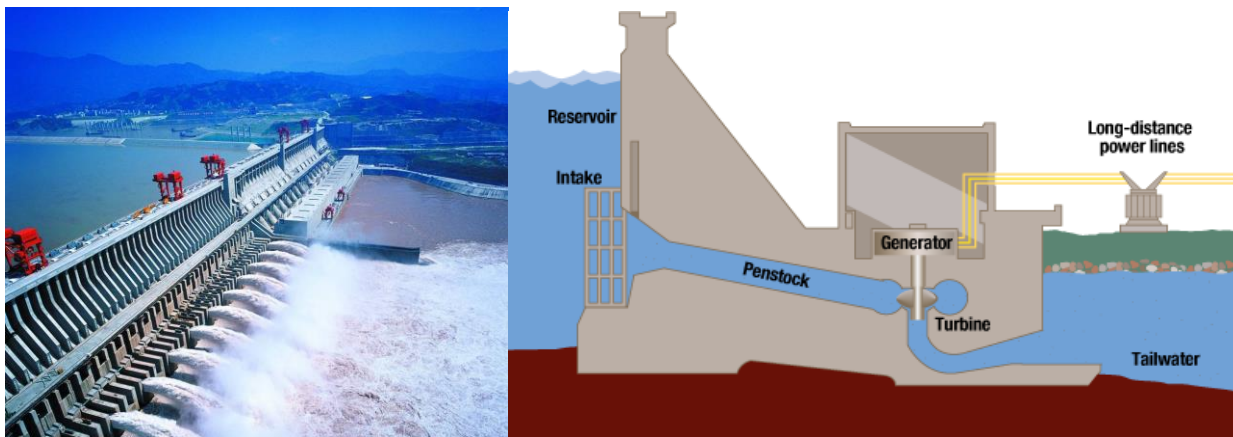
Figure 4. Dam and schematic images of hydroelectric energy.[9, 10]

1.2.3 Tidal Energy

Tidal energy is a form of hydropower that converts the energy obtained from tides into useful forms of power, mainly electricity by placing turbines in tidal streams. Compared to other sustainable energy sources, tides are more predictable. However, tidal energy has traditionally suffered from relatively high cost and limited availability of sites with sufficiently high tidal ranges or flow velocities, thus constricting its total availability. Although tidal energy not yet widely used, it has potential for future electricity generation. Many recent technological developments and improvements, both in design and turbine technology (e.g. new axial turbines,

cross flow turbines), indicate that the total availability of tidal power may be under estimated, and that economic and environmental costs may be able to bring down to competitive levels. Figure 5 shows an image of tidal turbines.
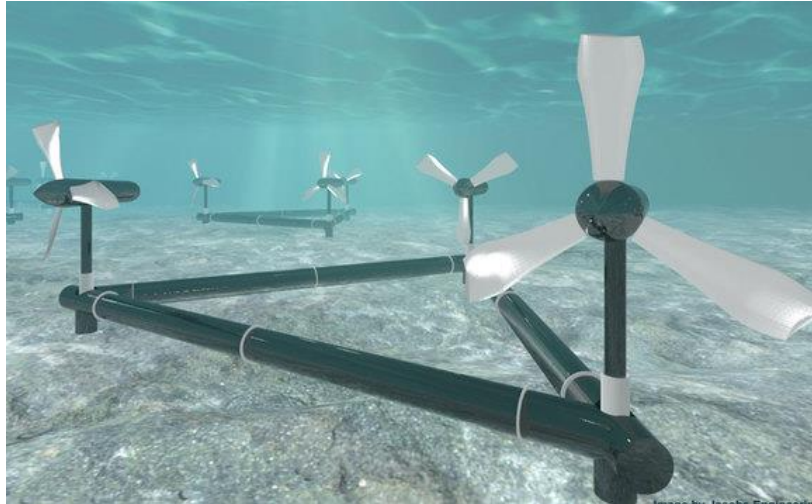
Figure 5. Image of tidal turbines.[11]

1.2.4 Geothermal Energy

Geothermal energy is thermal energy generated and stored in the Earth. The geothermal energy of the Earth's crust was generated from the original formation of the planet and from radioactive decay of materials. It drives a continuous conduction of thermal energy in the form of heat from the core to the surface. This heat is stored in water, steam and air that flow through the Earth, which can be vented and exploited. Theoretically, the Earth's geothermal resources are large enough to supply humanity's energy needs, but only a very small fraction may be profitably exploited because drilling and exploration for deep resources is very expensive. Figure 6 shows an image of geothermal energy station.

1.2.5 Biomass Energy

Biomass is waste material from plants or animals that is not used for food or feed. Materials such as forest debris, scrap lumber, certain crops, manure, and some types of waste residues are used to make up biomass fuels. Biomass is burned to produce steam that runs a

turbine to make electricity, or that supplies heat to industries and homes. Even though the process of using biomass energy to create electricity is similar to using fossil fuel, using biomass energy produces less emission and pollution than using fossil fuels. Figure 7 shows a schematic image of converting biomass into energy.

Figure 6. Image of geothermal energy station.[12]
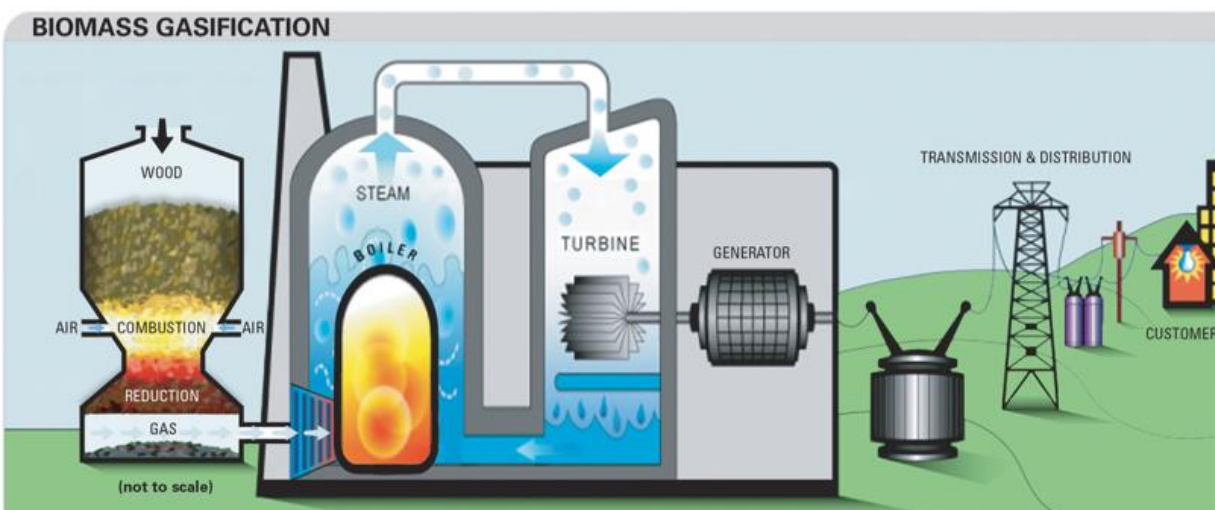
Figure 7. Schematic image of converting biomass into energy.[13]

1.2.6 Solar Energy

Solar energy is radiant light and heat from the Sun. It can be collected and converted to various types of energy such as heat, electricity, chemical potential, etc. by using different solar devices. A large portion of solar energy exploited today is converted to electricity by photovoltaic (PV) cells. In a single junction PV cell, a p-type semiconductor (which has been doped with electron acceptor atoms) and an n-type semiconductor (which has been doped with electron donor atoms) are fabricated with a common boundary, and the physical boundary between them is called the p-n junction. The device converts solar energy to electricity. When sunlight strikes the p-n junction, a voltage difference is produced between the p-type and n-type semiconductors, and electrodes connected to the p-type and n-type semiconductor layers allow current to be drawn from the device. In solar station or solar farms, large sets of PV cells can be connected together to form solar modules, arrays, or panels to generate huge amount of electricity. In the last two decades, PV has evolved from a market of small-scale applications towards becoming a mainstream electricity source. Figure 8a shows an image of a photovoltaic power station. Another promising way to use solar energy is converting solar energy to chemical potential and produce chemical fuels such as hydrogen, carbon monoxide, hydrocarbons, and oxygenates by photoelectrochemical (PEC, also known as artificial photosynthesis) cells. The solar to chemical potential conversion is a one-step process so that the chemical fuels can be directly stored without need for electrical energy storage devices such as batteries. The chemical fuels produced from the PEC cells can be used as energy source for industry manufacturing, transportation, etc. Figure 8b shows a schematic image of PEC water splitting.
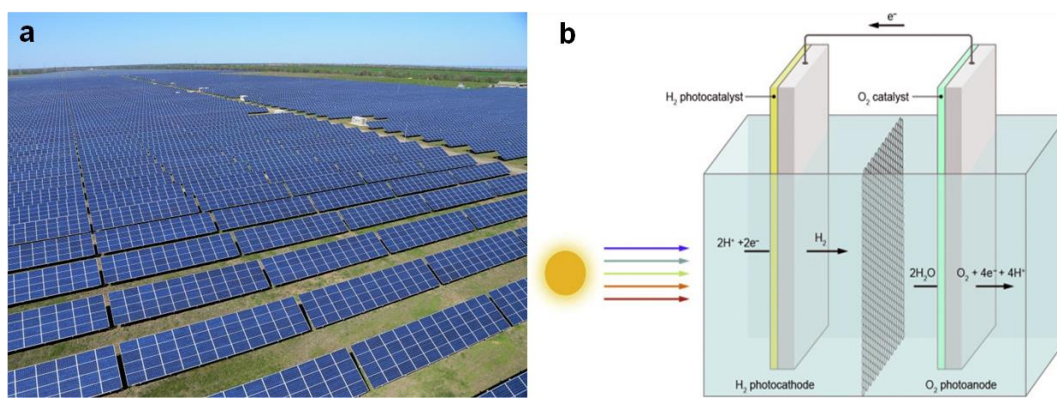
Figure 8. a) Image of a photovoltaic power station. b) Schematic image of PEC water splitting.[14]

1.2.7 Power Generating Capacities of Sustainable Energy Sources

The share of sustainable energy in meeting global energy demand is expected to grow by one-fifth in the next five years to reach 12.4% in 2023, and is predicted to reach 18% by 2040. However, that is still significantly below the benchmark of 28% from the International Energy Agency (IEA) Sustainable Development Scenario[15] In order to reach the benchmark of 28% by 2040, we need to know which sustainable energy source can possibly be used to fill the gap. Table 1 is a brief overview of global power generating capacities of sustainable energy sources. The estimated power generating capacity of wind energy is about 40,000 TWh, which represents 10%~15% of global technical potential for on- and off- shore installations. The estimated power generating capacities of hydroelectric energy and tidal energy are both less than 20,000 TWh, which are too small to meet our future energy demands. The estimated power generating capacities of geothermal energy is 120,000 TWh, however, only a small fraction of this can be exploited. Biomass energy is estimated to have potential to generate 100,000 TWh energy, however, the requirement of 10% earth's land surface coverage of switchgrass seems to be unrealistic. Among all the sustainable energy sources, solar is the only one that has the potential to meet all our energy needs. The total solar power reaching the earth's surface is about 1.2×10^9 TWh. To generate 2,000,000 TWh of energy from the sun, the area needed to be covered by 10% efficiency solar cell is about 0.16% of the earth's surface.

Energy source	Power (TW)	Remarks
Wind	4	Represents 10-15% of global technical potential for on- and off-shore installations.
Hydroelectric	1-2	Remaining untapped potential is 0.5 TW.
Tidal	<2	
Geothermal	12	Only a small fraction of this can be exploited.
Biomass	10	Requires 10% of earth's land surface to be covered with crops (e.g. switchgrass).
Solar	>20	Requires 0.16 % of the earth's surface to be covered with 10 % efficient solar cells. Total solar power reaching the earth's surface is 120,000 TW.

Table 1. Overview of global power generating capacities of sustainable energy sources

1.3 Overview of Current Solar Cells.

As we known, the cost is one of the most important factors that we need to consider when we are selecting the energy sources. Most of the solar devices we are using today are based on crystalline silicon light absorber. Figure 9 shows current and future cell production costs for different designs of crystalline silicon solar cells. As we can see, the cost of the silicon wafers represents over 60 % of the current and future total cell production costs in all types of crystalline silicon solar cells, which indicates that the light absorber is the bottleneck of limiting part of the solar cell in terms of cost. Therefore, in order to cut down the cost of solar cells, it is very important to find alternative light absorber materials.
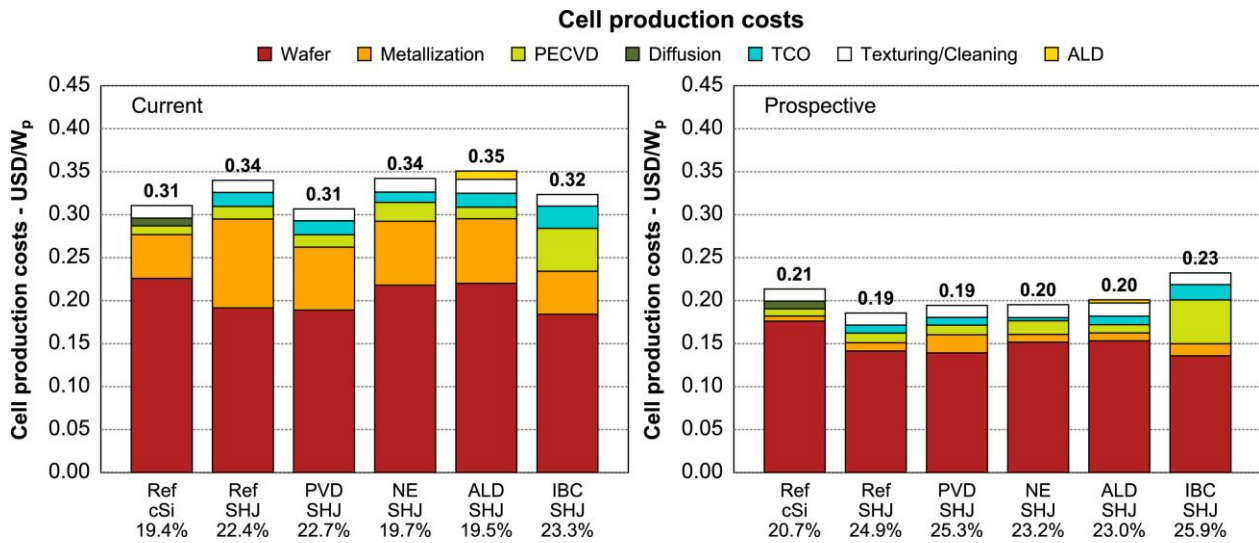
Figure 9. Current and future cell production costs for different designs of silicon solar cells. Left: current production costs; Right: prospective production costs. The percentages below the labels indicate cell efficiencies.[16]

1.4 Current Semiconducting Light Absorbers for Solar Cells

Today, different types of semiconducting material have been used as the light absorbers to make solar cells. The first type is the well-known crystalline silicon solar cell which has been commercialized for over 60 years. Crystalline silicon solar cells occupy about 90% of today's photovoltaic market, and the crystalline silicon-based solar panels can be easily found off the highways or on the roof of people's houses. The most efficient crystalline silicon solar cell achieved 25.8 % solar conversion efficiency, out of a theoretical maximum of 33%.[17] However,

defect tolerance in crystalline silicon solar cells is very low, and even very small concentration of defects can destroy the efficiency. This results in a high manufacturing cost for purification and production of crystalline silicon solar cells. Figure 10a shows an image of a crystalline silicon solar cell. On the other hand, amorphous silicon solar cells have much lower manufacturing cost compared to crystalline silicon solar cells. That is because amorphous silicon can be produced at much lower temperature. (as low as 75 °C[18]) Also, the absorption coefficient of amorphous silicon is about one order higher than crystalline silicon in visible light range which makes amorphous silicon even more cost competitive, and allows amorphous silicon to be used in thin film flexible solar cells. However, the amorphous silicon solar cells suffer from low solar conversion efficiency and low stability due to the Staebler-Wronski effect.[19] The most efficient amorphous silicon cell achieved a solar conversion efficiency of 11.3 %[20], which is much lower than the crystalline silicon solar cell with 25.8 % efficiency. Organic solar cells and dye-sensitized solar cells have similar disadvantages as amorphous silicon solar cells that they have low solar conversion efficiency and poor stability.[21, 22] Another type of solar cell is thin film chalcogenide cells, which includes copper indium gallium selenide (CIGS) and Cadmium telluride (CdTe). Most of them are bendable, and have high solar conversion efficiency.(The highest efficiency is 22.1% so far.[23]) However, these kinds of thin film solar cells are usually made by toxic material and non-earth abundant elements. It is difficult to have a large-scale production. Figure 10b shows an image of a cadmium telluride thin film solar cell. Another type of solar cell is organic-inorganic lead halide perovskite solar cell. A lot of efforts have been made to improve the efficiency and stability of these perovskite solar cells. The highest efficiency jumped from less than 5% to 23.7% in last 9 years.[24] However, the perovskite solar cells still suffer from the very poor stability which prevent the perovskite solar cells from having good long-term energy efficiency. Figure 10c shows an image of an organic-inorganic lead halide perovskites solar cell. The last type of solar cell is metal oxide solar cell. Metal oxide is a very promising candidate as light absorber in solar cell device. Most of metal oxides have advantages of high stability, low toxicity, low cost and abundance. Nevertheless, the commercialization of metal oxides solar cells is limited by its low solar conversion efficiency, and the highest efficiency so far is 8.1% achieved by Cu_2O cell.[25] Figure 10d shows an image of copper oxide solar panels.
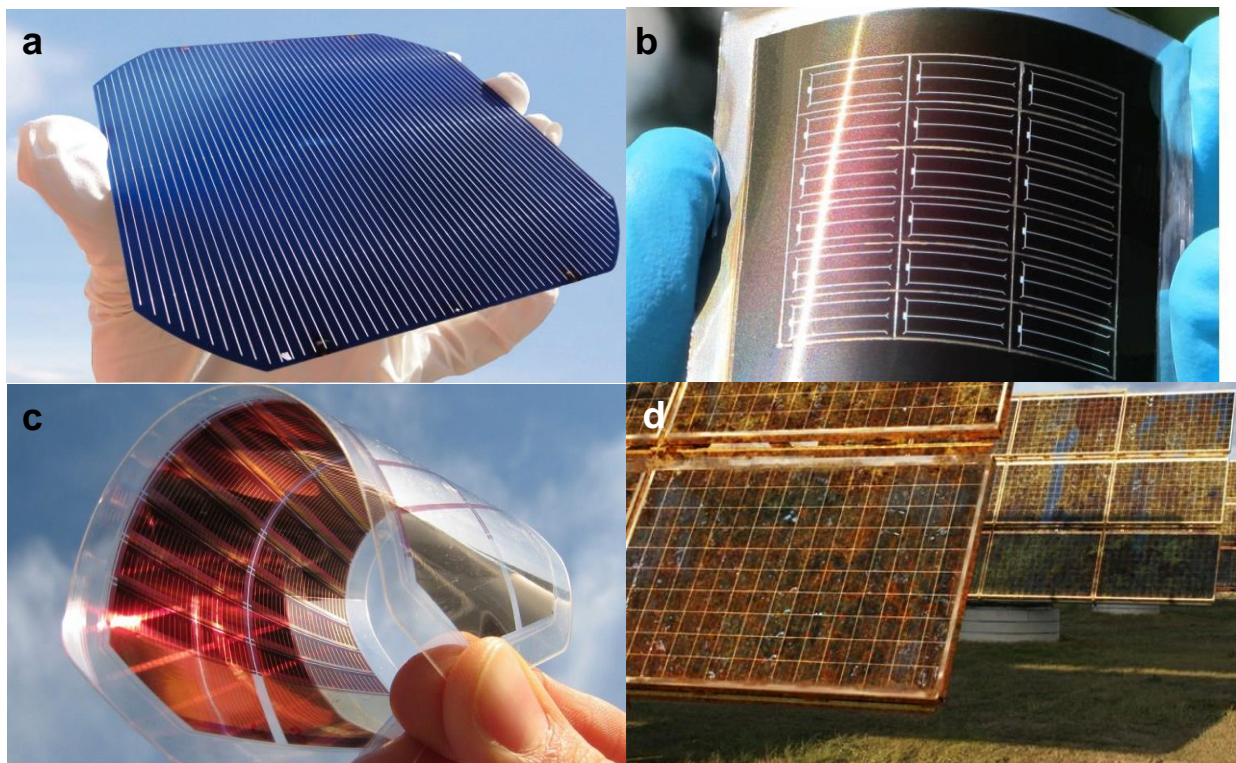
Figure 10. Image of a) crystalline silicon solar cell, b) cadmium telluride thin film solar cell,[26] c) organic-inorganic lead halide perovskites solar cell,[27] d) copper oxide solar panels.[28]

1.5 Metal Oxides as Light Absorbers

Compared to other light absorber materials, most of metal oxides have much better defect tolerance than crystalline silicon which allows much lower requirement of synthesis condition. Metal oxide thin-films could offer earth-abundant, non-toxic alternatives to current thin-film materials such as CdTe and CIGS, allowing us to tap our plentiful solar energy resource more cost-effectively and at a larger scale than is possible with today's materials.[29-35] Moreover, many metal oxides have good stability in harsh oxidizing and aqueous environments, which makes them more attractive compared to other emerging absorbers. This also means that they can be used in aqueous photoelectrochemical (PEC) solar cells, which directly produce chemicals or fuels from reactants and sunlight. However, metal oxides typically suffer from large band gaps or poor charge transport properties, or both. The poor charge transport properties in metal oxides are caused by their low charge mobilities. The magnitude of the charge mobility depends greatly

17

on the mechanism of charge transport, which in turn heavily depends on the nature of the bonding in the semiconductor and on the nature of the conduction and valence band orbitals. Covalent semiconductors with delocalized conduction and valence band states are characterized by high charge mobilities in the 50-1000 cm^2/Vs range[36], due to the excited charges can move in a quasi-free manner called band-like conduction. On the other hand, charge transport through ionic semiconductors (most of metal oxides) is generally more complicated and difficult. Ionic semiconductors are electrically polarizable due to deformation of the ions from their equilibrium positions. The coupling of the excited charges to this polarization is called a "polaron". This induced deformation and polarization will follow the charge as it moves through the medium, resulting in a higher effective mass for the charge.[37] A high degree of charge-lattice coupling results in the formation of "small" polarons that move by thermally-activated hopping with mobilities of order $10^{-4} - 10^{-1}$ cm^2/Vs (e.g. in $BiVO_4$ and Fe_2O_3),[37, 38] while lower coupling results in the formation of "large polarons" with mobilities in the range of 1-10 cm^2/Vs (e.g. in SnO_2 and WO_3).[37, 39]

1.5.1 Metal Oxides as Light Absorbers for Photoelectrochemical (PEC) Water Splitting

1.5.1.1 Introduction of PEC Water Splitting

PEC water splitting is one of the most promising ways to use solar energy. It converts solar energy to chemical potential and produce hydrogen. The water splitting reaction requires a minimum Gibbs free energy of 237 kJ/mol which corresponds to a potential of 1.23 V. As shown in Figure 1, in a regular PEC water splitting system, a photoanode and photocathode are serial connected to each other to generate enough potential to complete the water splitting reaction. The photoanode, which usually has a relatively large band gap, is used to absorb short wavelength light of the solar spectrum to conduct oxygen evolution reaction (OER). The photocathode, which usually has a relatively small band gap, is used to absorb long wavelength light of the solar spectrum to conduct hydrogen evolution reaction (HER). The serial connected tandem PEC water splitting system would operate at the current generated by the photocathode is equal to that generated by photoanode. An ideal PEC cell with two semiconductors with 1.40 eV and 0.52 eV can achieve 40% of solar to hydrogen (STH) efficiency.[40] Recently, a PEC water splitting device has been reported to operate with an STH efficiency of 30% through coupling a

photovoltaic cell and an electrolyser.[41] However, the cost of the PV–electrolyser system is too high to be commercialized and PEC water splitting requires a much simpler construction with fewer components (wires, electrodes, reactor, etc.). Thus, research is now concentrated on the development of direct low-cost, highly stable PEC water splitting cell using metal oxide as light absorber.
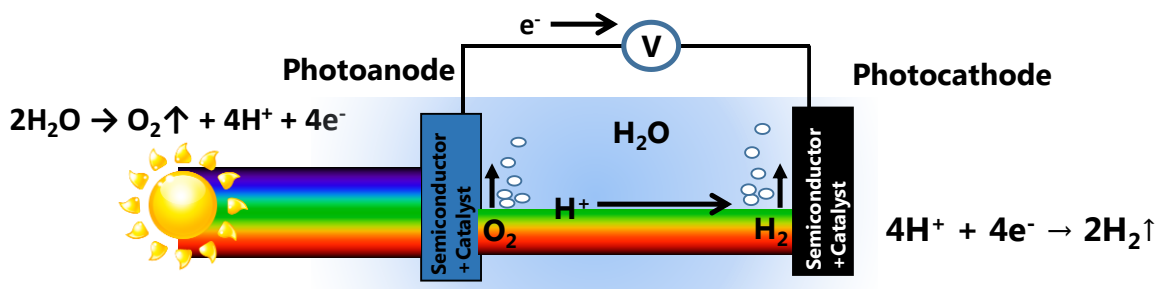
Figure 1. Schematic diagram of a simple PEC cell based on an n-type semiconducting photoanode serial connected to a p-type semiconductor photocathode.

1.5.1.2 Literature Review of Metal Oxides as Light Absorbers for PEC Water Splitting

In a PEC water splitting cell, an ideal photoanode and/or photocathode requires semiconductor materials that meet the following characteristics: (i) Suitable band gap energy and band position. The valence band potential of photoanode need must be more positive than the O_2/H_2O redox potential of 1.23 V vs. V_{NHE} (pH = 0) to carry out water oxidation, the conduction band potential must be more negative than the H^+/H_2 redox potential of 0 V vs. V_{NHE} to permit water reduction, and the added-up potential of the serial connected photoanode and photocathode must be larger than the water splitting potential of 1.23 V. (ii) Efficient charge separation and good charge transport properties. A light absorber with efficient charge separation and good charge transport properties allows charge carriers travel longer distance without recombination, which make them easier to be collected. (iii) Long term stability in aqueous solution. Electrode corrosion can easily occur in aqueous condition, especially in strong acidic or basic aqueous solution, which can decompose the photoelectrode and destroy the cell efficiency. (iv) The light absorber material should be low-cost and composed of earth abundant elements, which make it

possible to be commercialized and have a large-scale production. In last decades, numerous metal oxide light absorbers for PEC water splitting have been reported.

1.5.1.2.1 TiO$_2$ Photoanodes

TiO$_2$ is the first semiconductor material that being used as light absorber in PEC water splitting cell back to 1972.[42] TiO$_2$ has many favorable properties, such as suitable band position, high stability in harsh aqueous solution, and being composed of earth-abundant and nontoxic elements. However, due to its wide band-gap (3.2 eV), only a small portion of the solar spectrum can be absorbed by TiO$_2$, which highly limits its solar conversion efficiency. The maximum theoretical solar conversion efficiency of TiO$_2$ photoanode is 1.3%. Since 1972, many efforts have been made to improve the solar conversion efficiency of TiO$_2$-based photoanodes.[43-46] The most popular method is doping TiO$_2$ photoanode with anions or cations to extend its absorption range so that increase the overall absorption efficiency of the photoanode. The valence band of TiO$_2$ can be modified by introducing carbon[47] or nitrogen[48], while the conduction band can be modified by doping with 3d transition metal ions.[49] However, in most of these cases, the improvements in band gap are modest, and the visible light absorption of TiO$_2$ photoanodes are still very weak which prevents TiO$_2$ photoanodes from efficient water splitting.

1.5.1.2.2 α-Fe$_2$O$_3$ Photoanodes.

α-Fe$_2$O$_3$ (hematite) is a promising n-type light absorber for PEC water splitting. It has good chemical stability, low toxicity and low cost, and a decent bandgap value of about 2.1 eV, which allows it to absorb up to 590 nm wavelength light in the solar spectrum.[50] However, hematite has two serious drawbacks which highly limits its solar conversion efficiency. These drawbacks are: (i) a very short hole diffusion length of 2–4 nm, due to the short carrier lifetime (order of picoseconds)[51] and slow minority charge carrier mobility (0.2 cm^{2}V^{-1}s^{-1})[52]. (ii) a relatively low absorption coefficient, requiring at least a thickness of 400–500 nm for optimal light absorption. Several strategies have been tried to overcome these drawbacks. Firstly, heavily doping hematite with different elements, such as Si, Ti and P, which can improve the conductivity of electrons in hematite.[53] Secondly, Constructing a core-shell nanostructure hematite photoanode by coupling hematite with a highly conductive electron collector, which

can facilitate efficient hole transportation without compromising the light absorption.[54] Recently, a vertically-grown hematite nanosheet film modified with Ag nanoparticles and Co–Pi co-catalyst achieved the highest photocurrent of 4.68 mA/cm^2 at 1.23 V vs. V_{RHE}.[55] However, this 4.68 mA/cm^2 photocurrent is still much lower than its theoretical value of 12.6 mA/cm^2 which indicates that much more work is required to improve the solar conversion efficiency of hematite photoanode.

1.5.1.2.3 Cu$_2$O Photocathodes

P-type semiconductor cuprous oxide (Cu$_2$O) is the current top performing metal oxide light absorber for PEC water splitting due to its relatively small band gap of 2.0 eV and suitable conduction band position for hydrogen evolution reaction. Cu$_2$O also has advantages of low toxicity, low cost and abundance. However, the major drawbacks of Cu$_2$O photoanode are the fast electron-hole recombination and its poor stability in aqueous solution, because the redox potentials for the corrosion reaction of Cu$_2$O in water lie within the band gap.[56] Several strategies have been applied to overcome these drawbacks. Firstly, coupling Cu$_2$O with an n-type semiconductor with a more positive conduction band to form a p-n junction, which can help extract the carriers before they recombine. Secondly, conformally coating a thin protective layer to separate the Cu$_2$O photocathode and the electrolyte solution so that prevents the Cu$_2$O from corrosion.[56] Recently, by adapting strategies showing above, a Cu$_2$O nanowire/AZO/TiO$_2$/RuOx photoanode achieve more than 8 mA/cm^2 at 0 V vs. V_{RHE}, and stable operation beyond 50 h.[57]

1.5.1.2.4 Other Metal Oxide Photoelectrodes

In typical binary metal oxides, efficient carrier photoexcitation and transport are mutually exclusive: those with good charge transport properties such as ZnO,[58] SnO$_2$,[59] and WO$_3$[60] have large band gaps ($\geq$ 2.7 eV) which prevent efficient light absorption, while others such as CuO[61] and Co$_3$O$_4$[62] have moderate band gaps (0.9 - 2.2 eV) but are extremely poor conductors. Doping binary metal oxides with other metals (at relatively low concentrations, without changing the parent crystal structure) to improve optical and electronic properties has been extensively investigated, but charge transport properties have not been successfully improved and

improvements in band gap are modest. Considering that photocathodes usually have smaller band gaps than photoanodes and capable of larger photocurrents, and the serial connected tandem system would operate at the current generated by the photocathode is equal to that generated by photoanode, it is very important to find a n-type metal oxide material with moderate band gap and good charge transport property. A natural direction is alloying to obtain multi-metal oxides. This is distinct from doping in that the multi-metal oxides form entirely new crystal phases with distinct properties from the constituent oxides. Ternary metal oxides ($A_xB_yO_z$) in which A is a ns^2 metal cation (Bi^{3+}, Sn^{2+}, Sb^{3+}) and B is a md^0 metal cation (V^{5+}, Nb^{5+}, Ta^{5+}, Mo^{6+}, W^{6+}) are promising for solar energy conversion. They often have moderate band gaps due to hybridization of the ns^2 cation states with O 2p states, and relatively good charge transport properties due to the formation of large-polaron carriers by the hybridization of the md^0 cation states with O 2p states.

1.5.2 Metal Oxides as Light Absorbers for Photovoltaics (PV)

The market for photovoltaic (PV) modules has shown nearly exponential growth over the last few years, leading to a cumulative installed capacity of ~403 GW in 2017. Today, most of the PV modules are using silicon or thin films such as CdTe as light absorbers. Metal oxides also play important roles in PV cells. For examples, fluorine-doped tin oxide (FTO), indium tin oxide (ITO), and aluminum-doped zinc oxide (AZO) are widely used as transparent conducting layers in PV cells.[63, 64] Metal oxides have been also used as electron or hole transport layer in PV cells, due to their suitable band position.[65, 66] However, very few metal oxides have been used as light absorbers in PV cells, because most of metal oxides have relatively large band gaps, and can not absorb the light efficiently. One exception is Cu_2O, which has a relatively small band gap of 2.0 eV, and recently has been intensively investigated as light absorber in PV cell.[31, 67-69] Recently, a Cu_2O-based heterojunction solar cell using a $Zn_{1-x}Ge_xO$ thin film as an n-type window layer achieved 8.1 % of solar conversion efficiency.[25] This is the highest solar conversion efficiency achieved by any reported metal oxide based PV cell.

Reference

[1]   *Global Energy Statistical Yearbook 2018*; 2018.

[2]   Li, M. *World Energy 2018-2050: World Energy Annual Report*; 2018.

[3]   *The World Population Prospects: The 2017 Revision*; 2017.

[4]   *Renewables 2018 Global Status Report*; 2018.

[5]   *Trends in Atmospheric Carbon Dioxide*; 2019.

[6]   *Global Climate Report for Annual 2018*; 2019.

[7]   *Wind Power Capacity Worldwide Reaches 600 GW, 53,9 GW Added in 2018*; 2019.

[8]   *Another step toward wind-energy exportation in Canada*; 2017.

[9]   *Three Gorges Dam*; 2019.

[10]   *Conventional Hydroelectric Dams*.

[11]   *Buyer sought for stricken Tidal Energy amid 'economic and political uncertainty'*; 2016.

[12]   Geothermal energy.

[13]   *Biomass Gasification as a Unique use of Garbage*; 2019.

[14]   Cen, J.; Wu, Q.; Liu, M.; Orlov, A. *Green Energy & Environment* **2017,** 2, (2), 100-111.

[15]   *Renewables 2018* 2018.

[16]   Louwen, A.; van Sark, W.; Schropp, R.; Faaij, A. *Solar Energy Materials and Solar Cells* **2016,** 147, 295-314.

［17］　Battaglia, C.; Cuevas, A.; De Wolf, S. *Energy & Environmental Science* **2016,** 9, (5), 1552-1576.

［18］　Koch, C.; Ito, M.; Schubert, M. *Solar Energy Materials and Solar Cells* **2001,** 68, (2), 227-236.

［19］　Shimizu, T. *Japanese Journal of Applied Physics* **2004,** 43, (6A), 3257-3268.

［20］　Qarony, W.; Hossain, M. I.; Hossain, M. K.; Uddin, M. J.; Haque, A.; Saad, A. R.; Tsang, Y. H. *Results in Physics* **2017,** 7, 4287-4293.

［21］　Cheng, P.; Zhan, X. *Chemical Society Reviews* **2016,** 45, (9), 2544-2582.

［22］　Iwata, S.; Shibakawa, S.-i.; Imawaka, N.; Yoshino, K. *Energy Reports* **2018,** 4, 8-12.

［23］　Dharmadasa, I. M.; Ojo, A. A. *Journal of Materials Science: Materials in Electronics* **2017,** 28, (22), 16598-16617.

［24］　Kim, H.-S.; Hagfeldt, A.; Park, N.-G. *Chemical Communications* **2019,** 55, (9), 1192-1200.

［25］　Tadatsugu, M.; Yuki, N.; Toshihiro, M. *Applied Physics Express* **2016,** 9, (5), 052301.

［26］　Kranz, L.; Gretener, C.; Perrenoud, J.; Schmitt, R.; Pianezzi, F.; La Mattina, F.; Blösch, P.; Cheah, E.; Chirilă, A.; Fella, C. M.; Hagendorfer, H.; Jäger, T.; Nishiwaki, S.; Uhl, A. R.; Buecheler, S.; Tiwari, A. N. *Nature Communications* **2013,** 4, 2306.

［27］　*Perovskite – A Better Alternative*; 2018.

［28］　Regan, W.; Byrnes, S.; Gannett, W.; Ergen, O.; Vazquez-Mena, O.; Wang, F.; Zettl, A. *Nano Letters* **2012,** 12, (8), 4300-4304.

［29］　Shimura, F., Single-Crystal Silicon: Growth and Properties. In *Springer Handbook of Electronic and Photonic Materials*, Kasap, S.; Capper, P., Eds. Springer International Publishing: Cham, 2017; pp 1-1.

［30］   Liu, Y.; Turley, H. K.; Tumbleston, J. R.; Samulski, E. T.; Lopez, R. **2011,** 98, (16), 162105.

［31］   Minami, T.; Yamazaki, J.; Miyata, T. *MRS Communications* **2016,** 6, (4), 416-420.

［32］   Tadatsugu, M.; Yuki, N.; Toshihiro, M. *Applied Physics Express* **2013,** 6, (4), 044101.

［33］   Zhou, L.; Yang, Y.; Zhang, J.; Rao, P. M. *ACS Applied Materials & Interfaces* **2017,** 9, (13), 11356-11362.

［34］   Zhou, L.; Zhao, C.; Giri, B.; Allen, P.; Xu, X.; Joshi, H.; Fan, Y.; Titova, L. V.; Rao, P. M. *Nano Letters* **2016,** 16, (6), 3463-3474.

［35］   Kim, T. W.; Choi, K.-S. **2014,** 343, (6174), 990-994.

［36］   Arora, N. D.; Hauser, J. R.; Roulston, D. J. *Ieee Transactions on Electron Devices* **1982,** 29, (2), 292-295.

［37］   Rettie, A. J. E.; Chemelewski, W. D.; Emin, D.; Mullins, C. B. *Journal of Physical Chemistry Letters* **2016,** 7, (3), 471-479.

［38］   Abdi, F. F.; Savenije, T. J.; May, M. M.; Dam, B.; van de Krol, R. *Journal of Physical Chemistry Letters* **2013,** 4, (16), 2752-2757.

［39］   Tsuda, N., *Electronic conduction in oxides*. Springer-Verlag: 1991.

［40］   Fountaine, K. T.; Lewerenz, H. J.; Atwater, H. A. *Nature Communications* **2016,** 7, 13706.

［41］   Jia, J.; Seitz, L. C.; Benck, J. D.; Huo, Y.; Chen, Y.; Ng, J. W. D.; Bilir, T.; Harris, J. S.; Jaramillo, T. F. *Nature Communications* **2016,** 7, 13237.

［42］   Fujishima, A.; Honda, K. *Nature* **1972,** 238, (5358), 37-38.

［43］   Atabaev, T. S.; Hossain, M. A.; Lee, D.; Kim, H.-K.; Hwang, Y.-H. *Results in Physics* **2016,** 6, 373-376.

［44］　Li, H.; Jiang, L.; Xi, J.; Mu, J.; Wu, X. *Materials Research Express* **2017,** 4, (12), 126202.

［45］　Choi, M.; Lee, J. H.; Jang, Y. J.; Kim, D.; Lee, J. S.; Jang, H. M.; Yong, K. *Scientific Reports* **2016,** 6, 36099.

［46］　Li, Y.; Yu, H.; Song, W.; Li, G.; Yi, B.; Shao, Z. *International Journal of Hydrogen Energy* **2011,** 36, (22), 14374-14380.

［47］　Park, Y.; Kim, W.; Park, H.; Tachikawa, T.; Majima, T.; Choi, W. *Applied Catalysis B: Environmental* **2009,** 91, (1), 355-361.

［48］　Ansari, S. A.; Khan, M. M.; Ansari, M. O.; Cho, M. H. *New Journal of Chemistry* **2016,** 40, (4), 3000-3009.

［49］　Umebayashi, T.; Yamaki, T.; Itoh, H.; Asai, K. *Journal of Physics and Chemistry of Solids* **2002,** 63, (10), 1909-1920.

［50］　Tamirat, A. G.; Rick, J.; Dubale, A. A.; Su, W.-N.; Hwang, B.-J. *Nanoscale Horizons* **2016,** 1, (4), 243-267.

［51］　Barroso, M.; Pendlebury, S. R.; Cowan, A. J.; Durrant, J. R. *Chemical Science* **2013,** 4, (7), 2724-2734.

［52］　Dare-Edwards, M. P.; Goodenough, J. B.; Hamnett, A.; Trevellick, P. R. *Journal of the Chemical Society, Faraday Transactions 1: Physical Chemistry in Condensed Phases* **1983,** 79, (9), 2027-2041.

［53］　Sivula, K.; Le Formal, F.; Grätzel, M. *ChemSusChem* **2011,** 4, (4), 432-449.

［54］　Wheeler, D. A.; Wang, G.; Ling, Y.; Li, Y.; Zhang, J. Z. *Energy & Environmental Science* **2012,** 5, (5), 6682-6702.

［55］　Peerakiatkhajohn, P.; Yun, J.-H.; Chen, H.; Lyu, M.; Butburee, T.; Wang, L. *Advanced Materials* **2016,** 28, (30), 6405-6410.

［56］　Paracchino, A.; Mathews, N.; Hisatomi, T.; Stefik, M.; Tilley, S. D.; Grätzel, M. *Energy & Environmental Science* **2012,** 5, (9), 8673-8681.

[57]   Luo, J.; Steier, L.; Son, M.-K.; Schreier, M.; Mayer, M. T.; Grätzel, M. *Nano Letters* **2016,** 16, (3), 1848-1857.

[58]   Srikant, V.; Clarke, D. R. *Journal of Applied Physics* **1998,** 83, (10), 5447-5451.

[59]   Arlinghaus, F. J. *Journal of Physics and Chemistry of Solids* **1974,** 35, (8), 931-935.

[60]   González-Borrero, P. P.; Sato, F.; Medina, A. N.; Baesso, M. L.; Bento, A. C.; Baldissera, G.; Persson, C.; Niklasson, G. A.; Granqvist, C. G.; Silva, A. F. d. *Applied Physics Letters* **2010,** 96, (6), 061909.

[61]   Kumar, V.; Masudy-Panah, S.; Tan, C. C.; Wong, T. K. S.; Chi, D. Z.; Dalapati, G. K. In *Copper oxide based low cost thin film solar cells*, 2013 IEEE 5th International Nanoelectronics Conference (INEC), 2-4 Jan. 2013, 2013; pp 443-445.

[62]   Murad, W. A.; Al-Shamari, S. M.; Al-Khateeb, F. H.; Misho, R. H. *physica status solidi (a)* **1988,** 106, (2), K143-K146.

[63]   Rühle, S.; Anderson, A. Y.; Barad, H.-N.; Kupfer, B.; Bouhadana, Y.; Rosh-Hodesh, E.; Zaban, A. *The Journal of Physical Chemistry Letters* **2012,** 3, (24), 3755-3764.

[64]   Hamelmann, F. U. *Journal of Physics: Conference Series* **2014,** 559, 012016.

[65]   Haque, M. A.; Sheikh, A. D.; Guan, X.; Wu, T. *Advanced Energy Materials* **2017,** 7, (20), 1602803.

[66]   Lattante, S. *Electronics* **2014,** 3, (1), 132.

[67]   Minami, T.; Nishi, Y.; Miyata, T. *Journal of Semiconductors* **2016,** 37, (1), 014002.

[68]   Wei, H. M.; Gong, H. B.; Chen, L.; Zi, M.; Cao, B. Q. *The Journal of Physical Chemistry C* **2012,** 116, (19), 10510-10515.

[69]   Rai, B. P. *Solar Cells* **1988,** 25, (3), 265-272.

Chapter 2 BiVO$_4$ Photoanodes for Photoelectrochemical (PEC) Water Splitting

2.1 Literature Review of BiVO$_4$ Photoanodes

Recently, a ternary oxide BiVO$_4$ is found to be one of the top performing n-type metal oxide light absorbers because of its moderate stability and relatively small band gap (2.4 eV). As a light absorber, BiVO$_4$ is usually used as photoanode in photoelectrochemical (PEC) water splitting application because the conduction band and valence band energy of BiVO$_4$ have good match with the potentials of hydrogen evolution reaction and oxygen evolution reaction. However, the solar conversion efficiency of BiVO$_4$ cell is still limited by its moderate charge transport property. In BiVO$_4$ cell, the photo-exited electrons can only diffuse about 20 nm before they recombine and waste as heat. However, according to absorption measurements, 300 nm thick BiVO$_4$ is needed to absorb most of light. There is an efficiency trade-off in BiVO$_4$ solar cell. Increasing the thickness of BiVO$_4$ increases light absorption efficiency (η_{abs}) and decreases charge separation efficiency (η_{sep}), and vice versa.

In most of research, BiVO$_4$ was synthesized by solution-process (drop-casting, spin-coating and electrodeposition) followed by annealing in air. Figure 2 shows the numbers of publication of BiVO$_4$ and PEC cells in recent five years. As we can see, the numbers of publication of both these two topics are increasing by year which indicates that both of these two topics are more and more active attractive in the solar cell area. Based on BiVO$_4$ band gap energy, the maximum water oxidation photocurrent (J_{max}) for BiVO$_4$ photoanodes under Air-Mass 1.5 Global (AM 1.5G) solar illumination is 7.5 mA/cm^2.[1] However, the practical water oxidation photocurrent (J_{H2O}) of BiVO$_4$ is limited by less-than-unity light absorption efficiency (η_{abs}), charge separation efficiency (η_{sep}) and charge transfer efficiency (η_{trans}). η_{abs} accounts for the efficiency of generation of photoexcited charges and is decreased by the reflection and transmission of light; η_{sep} accounts for the efficiency of separation of the resulting photoexcited electrons and holes and their transport to the current collector and electrolyte, respectively, and is decreased by bulk recombination in the semiconductor and at internal interfaces; and η_{trans} accounts for the efficiency of charge transfer at the semiconductor/electrolyte interface, and is

decreased by surface recombination of holes. Among these efficiencies, high values of η_{trans} have already been achieved by coating $BiVO_4$ with oxygen evolution reaction (OER) catalysts like CoPi,[2] FeOOH[3] and NiOOH[4]. Moreover, η_{trans} values of 86% and 92% have been achieved at applied voltages of 0.6 and 1.0 V_{RHE}, respectively, by coating bilayer FeOOH/NiOOH.[5, 6] However, the value of the product of η_{abs} and η_{sep} ($\eta_{abs} \times \eta_{sep}$) remains low. Several strategies have been investigated to achieve a high $\eta_{abs} \times \eta_{sep}$ product in $BiVO_4$. Doping $BiVO_4$ by the substitution of V^{5+} with electron donors such as W^{6+} and Mo^{6+} is a popular strategy for improving η_{sep} since slow electron transport is known to be a bottleneck[8] in $BiVO_4$.[6, 7, 9-16] However, these same donors also behave as charge recombination centers and scattering sites, decreasing photoexcited carrier lifetimes and mobilities, so there is a limit to their effectiveness.[17] Apart from uniform doping of $BiVO_4$, the gradient doping of $BiVO_4$ with W has also been demonstrated, which creates an internal electric field that further enhances η_{sep}.[13] Another strategy involves the introduction of nanoscale porosity into $BiVO_4$, which improves η_{sep} because the penetration of the electrolyte into the pores decreases the transport distance for holes.[18] However, the electrons must still travel a relatively large distance across the entire thickness of the $BiVO_4$ film, which can limit the efficiency. Hydrogenation of $BiVO_4$ and doping with phosphorus or nitrogen have also successfully improved the performance.[19-21] Hydrogen doping improves $BiVO_4$ photoanode performance by passivation of the oxygen vacancy trap state in $BiVO_4$, which increases the photo-exited electron lifetime and electron diffusion length. Most recently, nitrogen doping of $BiVO_4$ decreased the band gap by about 0.2 eV, which enhanced η_{abs} by increasing the maximum wavelength at which $BiVO_4$ is able to produce photocurrent to 550 nm (compared to 510 nm for undoped $BiVO_4$), and improved η_{sep} by increasing electron mobility. Together, this resulted in a peak $\eta_{abs} \times \eta_{sep}$ of ~62% at 0.6 V_{RHE} for monochromatic light with wavelength of 400 nm, and $\eta_{abs} \times \eta_{sep}$ that is likely close to ~46% at 0.6 V_{RHE} for AM 1.5G sunlight, as determined by integration of the reported quantum efficiency over the standard AM 1.5G spectrum.[21]

Another strategy is to form heterostructures between $BiVO_4$ and other materials, most often WO_3,[12, 22-24] although others have also been explored.[25, 26] In WO_3/$BiVO_4$ heterojunctions, η_{sep} is improved because of the lower-lying conduction and valence bands of WO_3, which permit the extraction of electrons from $BiVO_4$ into WO_3, but block the passage of holes. A particularly effective form of this heterojunction is WO_3/$BiVO_4$ core/shell nanowire-arrays in which high-

surface-area WO_3 nanowire-arrays are coated with a thin layer of BiVO4. [6, 27-30] Here, η_{abs} is enhanced due to long light absorption paths in $BiVO_4$ along the nanowire axial direction and η_{sep} is enhanced both by the small thickness of $BiVO_4$, which allows a short transport distance for holes to the electrolyte, and by facile axial transport of electrons to the current collector through the WO_3 wires. Nonetheless, while $\eta_{abs} \times \eta_{sep}$ for core/shell $WO_3/BiVO_4$ nanowires is much higher than that for $BiVO_4$ alone and reaches high values at large applied voltages, we estimate from the report demonstrating the highest efficiency so far that $\eta_{abs} \times \eta_{sep}$ at 0.6 V_{RHE} is still limited to below 40%.[6] We hypothesize that the limited $\eta_{abs} \times \eta_{sep}$ at 0.6 V_{RHE} can be explained by two effects. The first is excess doping of W from the WO_3 nanowires into $BiVO_4$ during the formation of the core/shell structure (as much as 7% according to a previous study[27]), such that the detrimental recombination of photoexcited charges at W atoms exceeds the beneficial enhancement in electron conductivity. The second is the relatively low-lying conduction band of WO_3 compared to that of $BiVO_4$, which results in a higher turn-on voltage for the photocurrent compared to that of $BiVO_4$ alone.
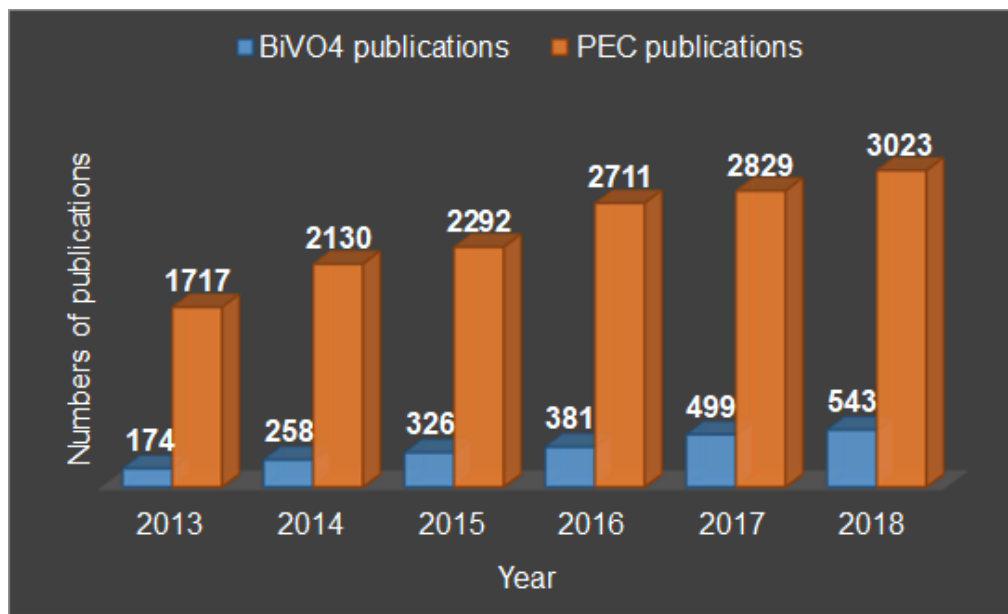
Figure 2. Numbers of publication of BiVO$_4$ and PEC cell

2.2 Objective of Present BiVO₄ Photoanodes for Photoelectrochemical (PEC) Water Splitting Research

The objective of present BiVO₄ photoanodes for PEC water splitting research is simultaneously improve light absorption efficiency and charge separation efficiency of BiVO₄ photoanode. This objective can be realized by the following approach: (1), find a core material for BiVO₄ photoanodes that not only conducts electrons well, but also has less interdiffusion with BiVO₄ compared to WO₃ during the annealing process. (2), measure and calculate the maximum thickness of BiVO₄ coating that has efficient charge separation. (3), synthesize a core/shell nanostructured BiVO₄ photoanode that has nanostructured core material figured out from (1), and uniform BiVO₄ shell coating with coating thickness figured out from (2).

2.3 Experimental Methods of BiVO₄ Photoanodes

2.3.1 Synthesis of planar WO₃/BiVO₄ heterojunction and planar Sb:SnO₂/BiVO₄ heterojunction

To facilitate a direct comparison, BiVO₄ layers of equal thicknesses (~80 nm) were spin-coated directly onto FTO substrates, onto planar Sb:SnO₂ films on FTO substrates, and onto planar WO₃ films on FTO substrates by annealing at 550 °C in air. The solution for spin-coating BiVO₄ was composed of 0.1225g Bi(NO₃)₃.5H₂O (98%, Sigma Aldrich) and 0.0663g OV(C₅H₇O₂)₂ (98%, Sigma Aldrich), dissolved in 5mL acetic acid (≥99.7%, Sigma Aldrich) and 0.25mL acetylacetone (≥99%, Sigma Aldrich) by 30 minutes sonication, resulting in a black-green solution. This solution was used for coating BiVO₄ in all experiments in this report. The planar WO₃ and Sb:SnO₂ films were prepared on FTO by spin coating a solution of 0.2M ammonium metatungstate ((NH₄)₆H₂W₁₂O₄₀.29H₂O), or 0.5M SnCl₄ and 0.025M SbCl₃, respectively, followed by annealing at 550 °C in air.

2.3.2 Synthesis of Sb:SnO₂/BiVO₄ NRA photoanodes

The Sb:SnO₂/BiVO₄ NRA photoanodes were synthesized by a combination of hydrothermal synthesis of Sb:SnO₂ NRAs and drop-casting of BiVO₄ onto the NRAs. Firstly,

fluorine-doped tin oxide (FTO) glass (Hartford Glass, IN) or quartz (Quartz Scientific) substrates were sonicated and cleaned 3 times in 1:1:1 isopropanol alcohol, acetone and DI water mixture. 0.474 g of $SnCl_2$ (98%, Sigma Aldrich) and 0.25 g of PEG 6000 (EMD) were dissolved into 10 mL of 2-Methoxyethanol (99%, Alfa Aesar) to prepare the SnO_2 seed layer solution. Then, the substrates were seeded by spin coating the SnO_2 seed layer solution and annealed at 550 °C for 2 hours. The recipe for the hydrothermal growth of Sb:SnO_2 NRAs was adapted from a previous report.[31] Two pieces of seeded substrates of dimensions 2 cm x 2.5 cm were placed face-down against the wall of a Teflon-lined autoclave (50 mL) containing a mixture of 15 mL of DI water, 15 mL of ethanol, 1.2 mL of HCl (38%), 135 mg of $SnCl_4.5H_2O$ and 0.043 mL Sb-dopant solution for hydrothermal synthesis of Sb:SnO_2 NRAs. The dopant solution was prepared by adding 0.0228 g of $SbCl_3$ in 10 mL ethanol. The hydrothermal reaction was performed 10 times at 200 °C for 12 h each to obtain Sb:SnO_2 NRAs of the desired length. Finally, the nanorod films were annealed at 550 °C for 30 minutes in air. Each 2 cm x 2.5 cm piece was then cut into two pieces to yield four pieces measuring 2 cm x 1.25 cm each. The solution for drop-casting $BiVO_4$ was composed of 0.1225g $Bi(NO_3)_3.5H_2O$ (98%, Sigma Aldrich) and 0.0663g $OV(C_5H_7O_2)_2$ (98%, Sigma Aldrich), dissolved in 5mL acetic acid (≥99.7%, Sigma Aldrich) and 0.25mL acetylacetone (≥99%, Sigma Aldrich) by 30 minutes sonication, resulting in a black-green solution. The Sb:SnO_2 NRAs on the substrate were soaked in acetic acid for 10mins and then dried by air-gun, which was found to improve the subsequent wetting and coating of the nanorods by the drop-casting solution. One edge of the FTO/Sb:SnO_2 NRAs was then covered with Scotch tape measuring 1.25 x 0.85 cm (to preserve an uncoated area that was later used to make electrical contact to the FTO/Sb:SnO_2 NRAs current-collector), leaving an area of 1.25 cm × 1.15 cm to be coated with $BiVO_4$. 2 drops of 5 μL solution were then dropped onto the Sb:SnO_2 NRAs, which was then dried on a hotplate set at 500°C in air for 10 minutes to make one $BiVO_4$ drop-casted layer. After 3 layers of drop-casting, the sample was annealed in a furnace in air at 550°C for 2 hours to crystallize the $BiVO_4$ and form the core/shell Sb:SnO_2/$BiVO_4$ NRA photoanode. To prepare the photoanode for PEC measurements, an electrical connection was then made to the exposed FTO/Sb:SnO_2 NRAs part of the photoanode by bonding a stainless steel wire using silver epoxy (Circuit Works No. 16043). The silver epoxy, any exposed FTO/Sb:SnO_2 NRA substrate area, and the portion of the stainless steel wire that would be submerged in the electrolyte were then all covered thoroughly with non-

conductive epoxy (Loctite 1C Hysol). The optical image of FTO, FTO/Sb:SnO$_2$ NRAs and FTO/Sb:SnO$_2$ NRAs/BiVO$_4$ are shown in Image 1.
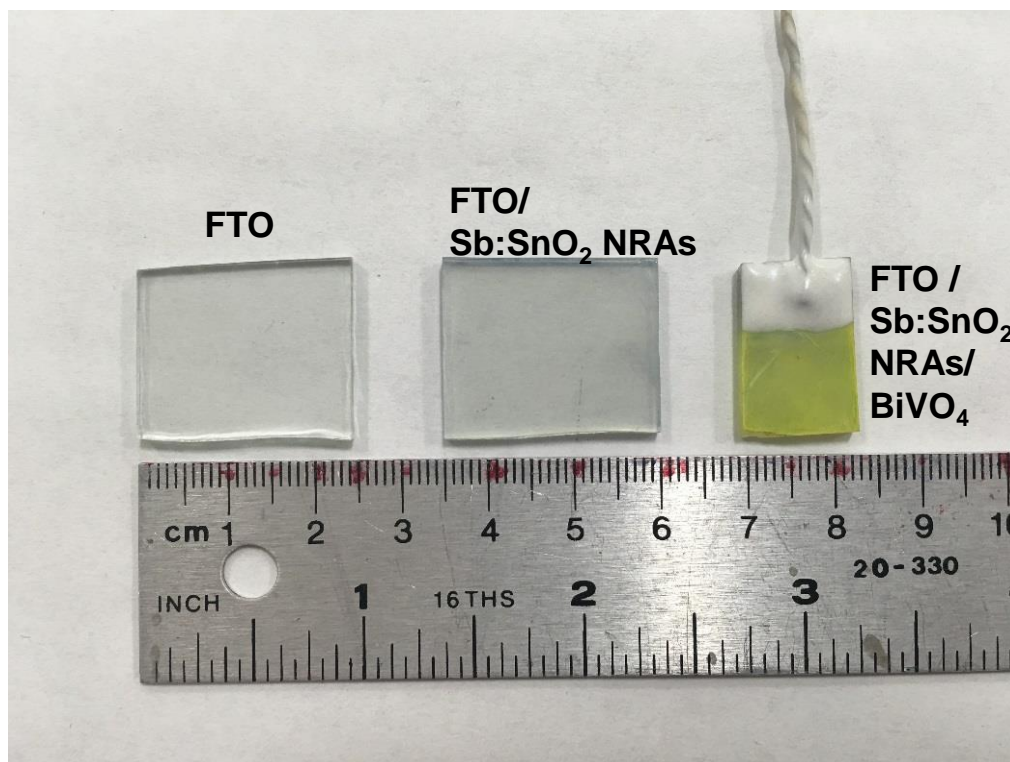
Image 1. Optical image of FTO (left), FTO/Sb:SnO$_2$ NRAs (middle), FTO/Sb:SnO$_2$ NRAs/BiVO$_4$ (right).

2.3.3 Synthesis of Sb:SnO$_2$ Nanotubes

Arrays of ZnO nanowires were synthesized on 2 cm * 2.5 cm FTO substrates (Hartford Glass, IN), that were first cleaned thoroughly by acetone + isopropyl alcohol + deionized water with sonication, and then coated with seed layer (5 mM zinc acetate dihydrate in ethanol) by spin coating at 2000 rpm for 30 s. Samples with seed layer were annealed at 350°C for 0.5 hour. ZnO nanowires were grown by immersing seeded substrates in aqueous solution containing 25 mM zinc nitrate hexahydrate (98%, Sigma Aldrich), 25mM hexamethylenetetramine (99%, Sigma Aldrich) and 5-7 mM polyethylenimine (branched, Aldrich) at 90-95°C for 2 hours. After first time growth of 2 hours, substrates were repeatedly introduced to fresh solution (20 mM zinc nitrate hydrate, 20mM hexamethylenetetramine and 5-6 mM polyethylenimine) for 2 hours at a time in order to obtain long nanowire arrays. The total reaction time was 6 hours, 8 hours, 10

hours or 12 hours. The arrays were then rinsed with deionized water and annealed in air at 400°C for 0.5 hours to remove any residual organics. The Sb:SnO$_2$ nanotube arrays were synthesized by coating Sb:SnO$_2$ layers onto the ZnO nanowire templates. Sb:SnO$_2$ solution containing 0.1225g SnCl$_2$ (98%, Sigma Aldrich) and 0.075g SbCl$_3$ (99%, Sigma Aldrich) in 10 mL 2-methoxyethanol (99%, Alfa Aesar) was firstly spin coated on the ZnO nanowire templates. After 5 layers of Sb:SnO$_2$ coating, the substrates were annealed in air at 550°C for 2 hours to crystallize the Sb:SnO$_2$ nanotube shell. Then, the ZnO nanowire templates with the Sb:SnO$_2$ shell was etched in acetic acid (99.7%, Sigma Aldrich) for 4 hours and thoroughly washed in DI water to remove all the ZnO. The samples were then again spin coated with 5 more layers of Sb:SnO$_2$ solution, annealed and etched in acetic acid one more time to make the Sb:SnO$_2$ nanotube walls thicker and further decrease the possibility of Zn doping in the outer layers of the Sb:SnO$_2$ nanotubes, which might otherwise dope into the BiVO$_4$ shell.

2.3.4 Synthesis of Sb:SnO$_2$/BiVO$_4$ Nanotube Photoanodes

The BiVO$_4$ drop casting method for Sb:SnO$_2$/BiVO$_4$ nanotubes Photoanodes was same as the BiVO$_4$ drop casting method for Sb:SnO$_2$ NRAs. The Sb:SnO$_2$ nanotube arrays on the substrate were soaked in acetic acid for 10mins and then dried by air-gun to improve the subsequent wetting and coating of the nanotube arrays by the drop-casting solution. One edge of the substrate was then covered with Scotch tape measuring 1 x 0.85 cm (to preserve an uncoated area that was later used to make electrical contact to the FTO/Sb:SnO$_2$ nanotube arrays current-collector), leaving an area of 1 cm × 1.15 cm to be coated with BiVO$_4$. 2 drops of 5 μL solution were then dropped onto the Sb:SnO$_2$ nanotube arrays, which was then dried on a hotplate set at 500°C in air for 10 minutes to make one BiVO$_4$ drop-casted layer. After 4 layers of drop-casting, the sample was annealed in a furnace in air at 550°C for 2 hours to crystallize the BiVO$_4$ and form the core/shell Sb:SnO$_2$/BiVO$_4$ nanotubes photoanode. To prepare the photoanode for PEC measurements, an electrical connection was then made to the exposed FTO/Sb:SnO$_2$ nanotube arrays part of the photoanode by bonding a nickel wire using silver epoxy (Circuit Works No. 16043). The silver epoxy, any exposed FTO/Sb:SnO$_2$ NRA substrate area, and the portion of the nickel wire that would be submerged in the electrolyte were then all covered thoroughly with

non-conductive epoxy (Loctite 1C Hysol). The optical images of ZnO nanowires, Sb:SnO$_2$ nanotubes and Sb:SnO$_2$/BiVO$_4$ nanotubes are shown in Image 2.
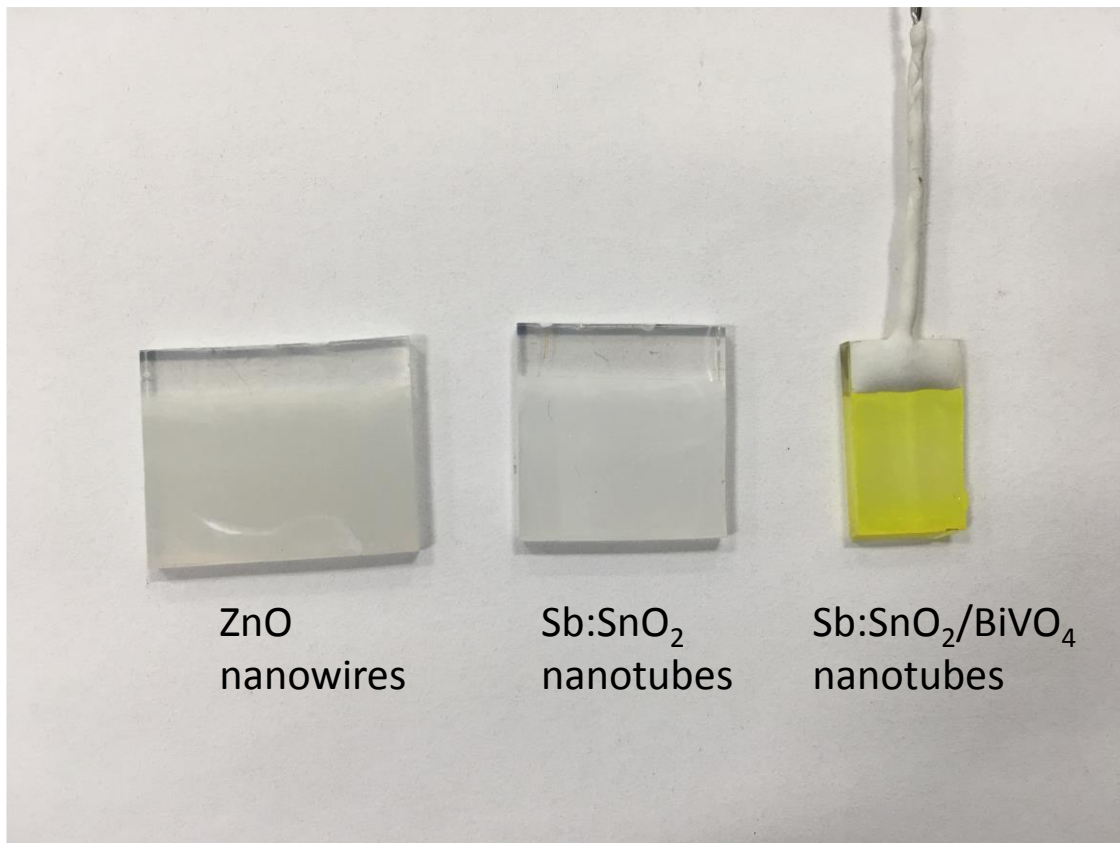
Image 2. Optical image of ZnO nanowires (left), Sb:SnO$_2$ nanotubes (middle), Sb:SnO$_2$/BiVO$_4$ nanotubes (right).

2.3.5 Light Absorption Test of Photoanodes

The water photooxidation current of photoanodes can be expressed as $J_{H2O} = J_{max} \times \eta_{abs} \times \eta_{sep} \times \eta_{trans}$.[27] We determine J_{max} by integrating the incident spectral irradiance over all wavelengths below 515 nm, which is the band edge of BiVO$_4$, and determine η_{abs} by integrating the product of the incident spectral irradiance and the light harvesting efficiency (LHE, the fraction of absorbed light) at each wavelength, and dividing by J_{max}. The simulated solar illumination in this study was provided by a Xe lamp (Model 6258, Oriel) equipped with an AM1.5G filter (Model 81094, Oriel), and the spectral irradiance was measured by a spectrometer (Model USB2000+Rad, Ocean Optics). The wavelength-dependent LHE of

the photoanode was measured using an integrating sphere with white-light illumination from the Xe lamp, and calculated from the measured reflection (R) and transmission (T) as LHE (λ) (%) = 100% - R (λ) (%) - T (λ) (%). The measurements were made with light incident on the glass-side of the photoanode (referred to as "back"), or incident on the side of the photoanodes (referred to as "front"). For the transmission measurements, the photoanode was placed at the front port of the sphere, and the transmittance spectrum was referenced to that of the empty port. For the reflection measurements, the photoanode was placed at the back port of the integrating sphere and the reflectance spectrum was referenced to that of a white standard. To ensure that the sphere throughput was identical to that for the photoanode measurement and thereby eliminate comparison error, the photoanode was placed at the side port of the sphere for both the transmission and reflection reference measurements, and the side port was closed with the white standard during the transmission measurement of the photoanode but left open for the reflection measurement of the photoanode. The spectrometer was placed at the top port to measure the spectral irradiance of the transmitted and reflected light, respectively.

2.3.6 PEC Measurements of Photoanodes

The PEC performance of all photoanodes were evaluated by measuring the current density-voltage (J-V) curve (i.e. linear sweep voltammogram) under both front-side (electrolyte-side) and back-side (glass-side) illumination in a three-electrode configuration using a potentiostat (Model SP-200, BioLogic), with the photoanode as working electrode, a saturated calomel electrode (SCE) as the reference electrode and a Pt wire as the counter electrode. The entire exposed area of the photoanodes ($1.44 cm^2$) were used in all calculations of photocurrent density. The J-V curve was measured at a scan rate of 10mV/s. Since our goal is to measure the $\eta_{abs} \times \eta_{sep}$ product rather than the photocurrent for water oxidation (J_{H2O}), both the J-V curve were measured in 0.5M potassium phosphate aqueous solution buffered to pH 7, with 1M sodium sulfite (Na_2SO_3) added as a hole scavenger. Because of the fast oxidation kinetics of sulfite, the surface charge transfer efficiency of the photoanode (η_{trans}) is nearly equal to 100%, allowing the $\eta_{abs} \times \eta_{sep}$ product to be calculated from $\eta_{abs} \times \eta_{sep} \approx J_{sulfite}/J_{max}$, where $J_{sulfite}$ is the photocurrent density for sulfite oxidation. Although sulfite photo-oxidation has been used in several studies to extract $\eta_{abs} \times \eta_{sep}$.[5, 6, 24, 32]

2.4 Results and Discussions of Sb:SnO₂ nanorods/BiVO₄ Photoanodes

In order to select a better choice of core material for $BiVO_4$ photoanode, we examine the PEC behaviors of a planar $WO_3/BiVO_4$ heterojunction and a planar $Sb:SnO_2/BiVO_4$ heterojunction, in which the $BiVO_4$ layers are of the same thickness and are not intentionally doped. The SEM images of planar $WO_3/BiVO_4$ heterojunction and planar $Sb:SnO_2/BiVO_4$ heterojunction are shown in Figure 3. The LHE of each film was measured (Figure 4a) and used to calculate η_{abs} from the spectral irradiance of the Xe lamp solar simulator, yielding 35.6 %, 38.1% for the $Sb:SnO_2/BiVO_4$ heterojunction and $WO_3/BiVO_4$ heterojunction, respectively. J-V curves of all films were then measured for sulfite oxidation, and η_{sep} was calculated from $\eta_{sep} \approx J_{sulfite}/(J_{max} \times \eta_{abs})$ and plotted (Figure 4b). We found that as a core material, $Sb:SnO_2$ can provide better charge separation efficiency to $BiVO_4$ photoanodes compared to the commonly used WO_3 core material. That is because unlike W, Sn and Sb are almost insoluble in $BiVO_4$. A previous study showed that $BiVO_4$ is (unintentionally) heavily doped by W^{6+} ions (up to 7%) from WO_3 during formation of the $WO_3/BiVO_4$ heterojunction by annealing.[27] This high doping concentration greatly decreases the depletion width in $BiVO_4$, is well above the ~1% concentration of W^{6+} that has been shown to improve η_{sep} by increasing the electron concentration and conductivity,[2] and could be large enough that the detrimental recombination of photoexcited charges at W^{6+} ions would exceed the beneficial effect of increased electron concentration. In addition, doping W into $BiVO_4$ is expected to shift the flat band potential to more positive values (farther from vacuum level),[33] which would undesirably increase the voltage of photocurrent onset. Secondly, $Sb:SnO_2$ has higher electrical conductivity compared to WO_3 which can decrease the series resistance in the photoanode.[34] Therefore, comparing the $Sb:SnO_2/BiVO_4$ and $WO_3/BiVO_4$ heterojunctions, we expect the $Sb:SnO_2/BiVO_4$ heterojunction to have higher η_{sep} and lower photocurrent onset voltage.
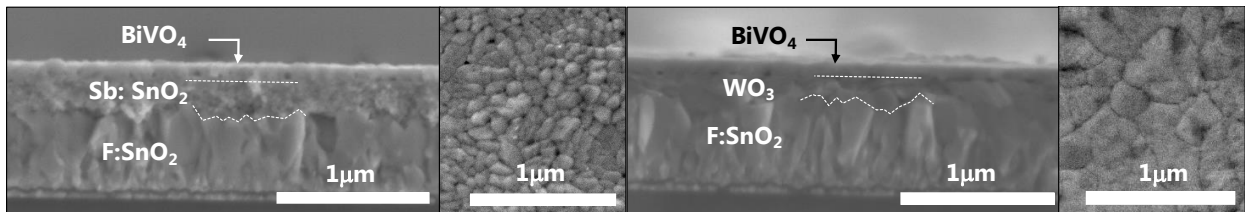
Figure 3. SEM images of planar $WO_3/BiVO_4$ heterojunction (right) and planar $Sb:SnO_2/BiVO_4$ heterojunction (left)
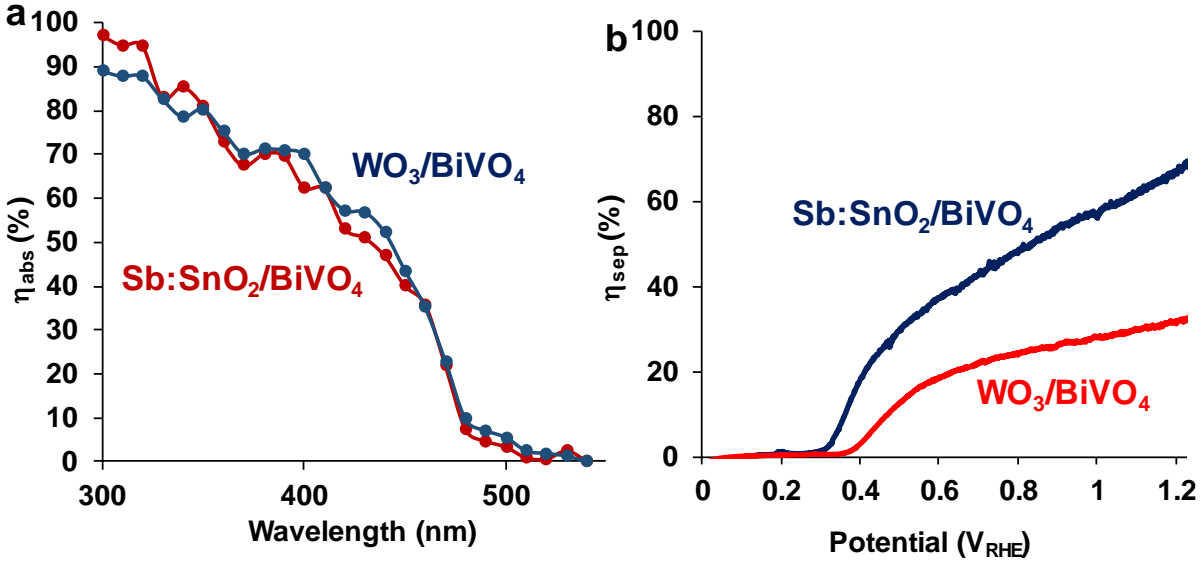
Figure 4. a) Light harvesting efficiency of $WO_3/BiVO_4$ heterojunction (blue) and $Sb:SnO_2/BiVO_4$ heterojunction (red), b) charge separation efficiency of $WO_3/BiVO_4$ heterojunction (blue) and $Sb:SnO_2/BiVO_4$ heterojunction (red)

After selecting the core material, we need to decide how thin the shell $BiVO_4$ layer should be to achieve high η_{sep} at low bias. The thickness of $BiVO_4$ layer with high separation efficiency is equal to the electron diffusion length plus the depletion width. The hole and electron diffusion lengths in $BiVO_4$ are reported to be ~100 nm and ~20 nm, respectively, and electron transport is known to be the performance-limiting bottleneck in $BiVO_4$.[9, 14, 17, 35] To determine the depletion layer width in the $BiVO_4$ as a function of potential, we have performed AC capacitance (Mott-Schottky) measurements of a separately synthesized planar non-porous, spin-coated film of $BiVO_4$. A $BiVO_4$ layer of approximately 80 nm thickness was spin-coated onto an FTO substrate using the same $BiVO_4$ solution that was used for drop-casting $BiVO_4$, followed by annealing at 550 °C in air. Although the $BiVO_4$ is not doped, it contains oxygen vacancies that behave as electron donors.[35] The Mott-Schottky plot is a plot of $1/C^2$ vs V, where C is the capacitance, and V is the voltage. The equivalent circuit for the Mott-Schottky measurement is a resistor in series with a capacitor. The capacitor is taken to represent the capacitance across the semiconductor depletion layer. The capacitance of the electrical double layer at the semiconductor/electrolyte interface is assumed to be much larger, and can therefore be neglected. No additional circuit elements are needed to account for mass transport, etc. since these

measurements are made at high frequency. The capacitance C at frequency f is calculated from the imaginary part of the measured impedance Z as:

$$\text{Im}(Z) = \frac{-1}{2\pi f C}$$

In the linear region at low potentials, the depletion width is smaller than the thickness of the semiconductor. When the depletion width equals or exceeds the thickness of the semiconductor at higher potentials, the capacitance plateaus,[36] which can be seen in the Mott-Schottky plot in Figure 5a.
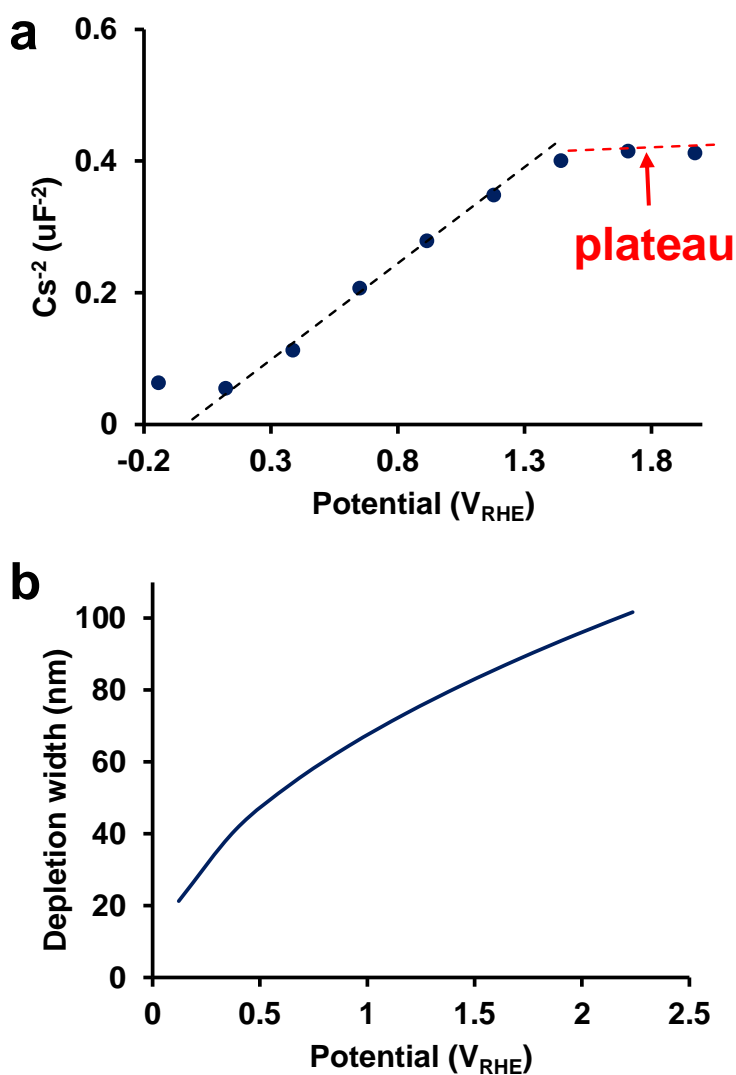
Figure 5. a) Mott-Schottky plot of planar, non-porous $BiVO_4$ over extended potential range, and b) depletion width of $BiVO_4$ versus potential.

The capacitance of the semiconductor/liquid junction is given by the following Mott-Schottky equation

$$\frac{1}{C^2} = \frac{2}{\varepsilon \varepsilon_0 A^2 e N_D} (V - V_{FB} - \frac{k_B T}{e})$$

where C is the capacitance, A is the surface area of the planar semiconductor (2 cm^2 for our planar BiVO$_4$), ε_0 = 8.8*10^{-12} F/m is the permittivity of free space, ε is the relative permittivity of the semiconductor, (68 for BiVO$_4$[9]), e=1.6*10^{-19} C is the electron charge, k=1.38*10^{-23} (m^2 kg s^{-2} K^{-1}) is the Boltzmann constant, T is temperature =300 K, and V$_{FB}$ is the flat band potential of the semiconductor. The concentration of electron donors (N$_D$) is calculated from the slope of the measured Mott-Schottky plot using the above equation. The value obtained is 1.7×10^{18}/cm^3. Then the depletion width as a function of applied voltage, is calculated using the following equation, and is plotted in Figure 5b.

$$W = \sqrt{\frac{2\varepsilon \varepsilon_0}{e N_D} \left(V - V_{FB} - \frac{k_B T}{e} \right)}$$

This calculation shows that the depletion width becomes equal to the film thickness of ~80 nm for a potential of around 1.5 V, which matches the potential at which the MS plot plateaus. Because most photocathodes can usually supply 0.6 V bias to the photoanode, we aimed at having a high performance of the photoanode at 0.6 V$_{RHE}$. And we found that the depletion width of our BiVO$_4$ at 0.6 V$_{RHE}$ is about 40 nm. Again, the thickness of BiVO$_4$ layer with high separation efficiency is equal to the electron diffusion length plus the depletion width. For our BiVO$_4$, it should be 20 nm + 40 nm which is 60 nm. This is therefore the maximum allowable thickness for the BiVO$_4$.

After synthesis of core/shell Sb:SnO$_2$/BiVO$_4$ NRAs, the morphologies and crystal structures of the core/shell Sb:SnO$_2$/BiVO$_4$ NRAs on FTO substrates were characterized by scanning electron microscopy (SEM, JEOL 7000F, 5 kV) and parallel beam X-ray diffraction (XRD, PANalytical Empyrean, Cu-kα, 45 kV, 40 mA). Monoclinic BiVO$_4$ and tetragonal SnO$_2$ are the only phases detected by XRD for the Sb:SnO$_2$/BiVO$_4$ NRAs grown on FTO substrates (Figure 6). The average crystallite size in the BiVO$_4$ shell of the Sb:SnO$_2$/BiVO$_4$ NRAs was

estimated to be ~20 nm using the Scherrer equation applied to the (112) reflection of $BiVO_4$. The XRD patterns of the $Sb:SnO_2$ NRAs and the $BiVO_4$ in the core/shell $Sb:SnO_2/BiVO_4$ NRAs are unchanged compared to those of the separate $Sb:SnO_2$ NRAs and drop-casted $BiVO_4$, which indicates that there was no measurable inter-reaction or inter-doping between the two phases (unlike the XRD patterns in the case of $WO_3/BiVO_4$[27]).
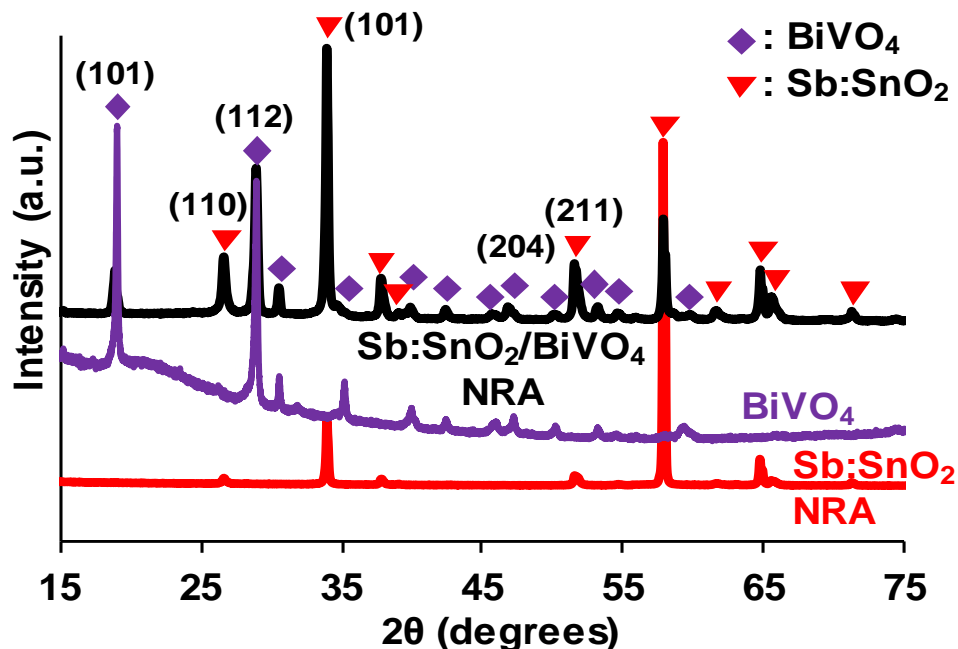
Figure 6. X-ray diffraction patterns of $Sb:SnO_2$ NRAs (red), $BiVO_4$ film (purple), and $Sb:SnO_2/BiVO_4$ core/shell NRAs (black).

According to SEM images (Figure 7a), the SnO_2 nanorods are quasi-aligned perpendicularly to the FTO substrate and have diameters ranging from 40 nm to 250 nm with an average of about 100 nm, lengths up to 1.3 µm with an average of about 1.0 µm, and an average inter-rod (axis-to-axis) spacing of about 170 nm. The shorter nanorods tend to have smaller diameters and smaller inter-rod spacing, while the larger nanorods tend to have larger diameters and larger inter-rod spacing. After 3 layers of $BiVO_4$ are drop-casted and annealed (Figure 7b), the $Sb:SnO_2/BiVO_4$ NRAs have a similar length as the uncoated $Sb:SnO_2$ NRAs, which indicates that most of the $BiVO_4$ was coated on the sidewalls of the $Sb:SnO_2$ NRs rather than on top. However, there is a wide variation in the thickness of the $BiVO_4$ shell. The $BiVO_4$ coating the

upper regions of the taller, larger-diameter nanorods tends to be relatively thick (up to ~100 nm), and encapsulates only a single $Sb:SnO_2$ nanorod, while the $BiVO_4$ coating the shorter, smaller-diameter, more closely-spaced nanorods tends to be thinner and often encapsulates more than one $Sb:SnO_2$ NR. We have also provided SEM images of the $Sb:SnO_2$ NRs coated with 2 and 4 layers of $BiVO_4$ in Figure 12a and 12b. These also show the thicker coating of $BiVO_4$ at the upper regions of the nanorods compared to the bottom regions.
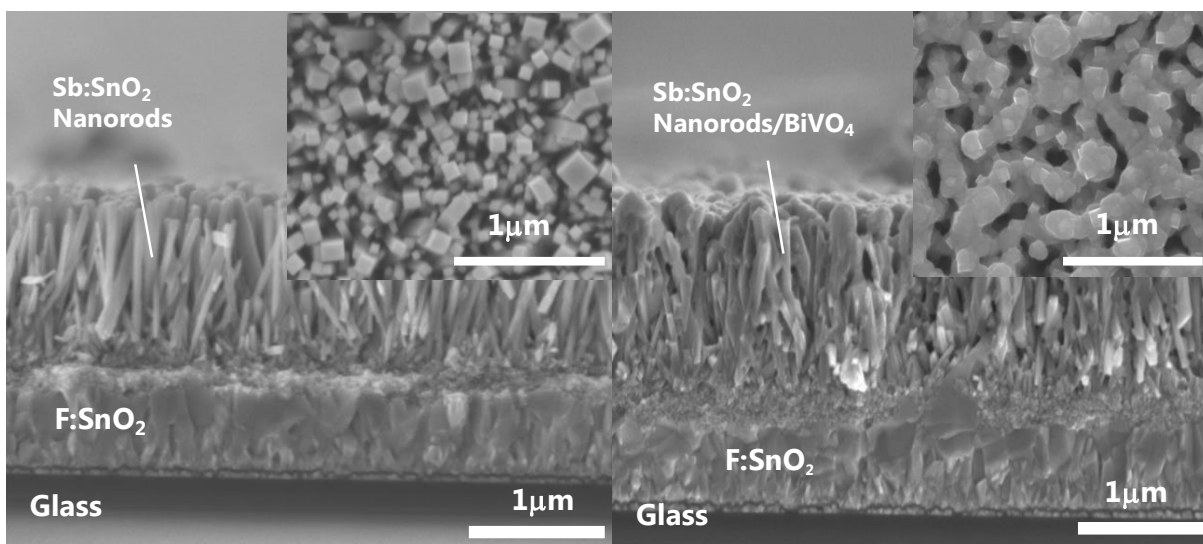
Figure 7. Scanning electron microscopy cross-section images (and inset top-view images) of a) $Sb:SnO_2$ NRAs, and b) 3 layers of $BiVO_4$ drop-casted onto the $Sb:SnO_2$ NRAs to form $Sb:SnO_2/BiVO_4$ core/shell NRAs

High-resolution transmission electron microscopy (TEM, JEOL 2010F, 200kV) was conducted on the core/shell $Sb:SnO_2/BiVO_4$ NRAs to further elucidate the morphology of the $BiVO_4$ shell (Figure 8). An $Sb:SnO_2$ NR of approximately 40 nm diameter with a $BiVO_4$ shell of approximately 30 nm was examined, and it was found that the shell consists of randomly-oriented $BiVO_4$ crystallites with size ranging from 2 to 10 nm. Both the diameter of the NR and the thickness of the $BiVO_4$ shell that were selected for examination were on the thin side of the distribution, since thicker wires and thicker shells were not sufficiently transparent for high-resolution TEM imaging. Given that the average $BiVO_4$ crystallite size from XRD measurements was ~20 nm, we expect that thicker NRs with thicker $BiVO_4$ shells would have larger $BiVO_4$

crystallites. The relatively small crystallite size in the $BiVO_4$ shell could lead to increased carrier recombination and slower charge transport due to the presence of higher concentration of grain boundaries compared to films with larger crystallite sizes. A recent study demonstrated that, for $BiVO_4$ films synthesized by successive layers of solution deposition (as has been done here), intermediate annealing steps of at least 350 °C are required to obtain full crystallinity of the $BiVO_4$ layers, even if final annealing is done at higher temperatures.[37] In the present study, the drop-casted $BiVO_4$ layers were subjected to intermediate annealing steps on a hotplate set to 500 °C, before being annealed in a furnace at 550 °C. However, we estimate that the actual temperature achieved during hotplate annealing was much lower, around 200-300 °C. Therefore, the influence of higher-temperature intermediate annealing on the crystallinity of the $BiVO_4$ shell and the resulting PEC performance remains a subject for future investigation.
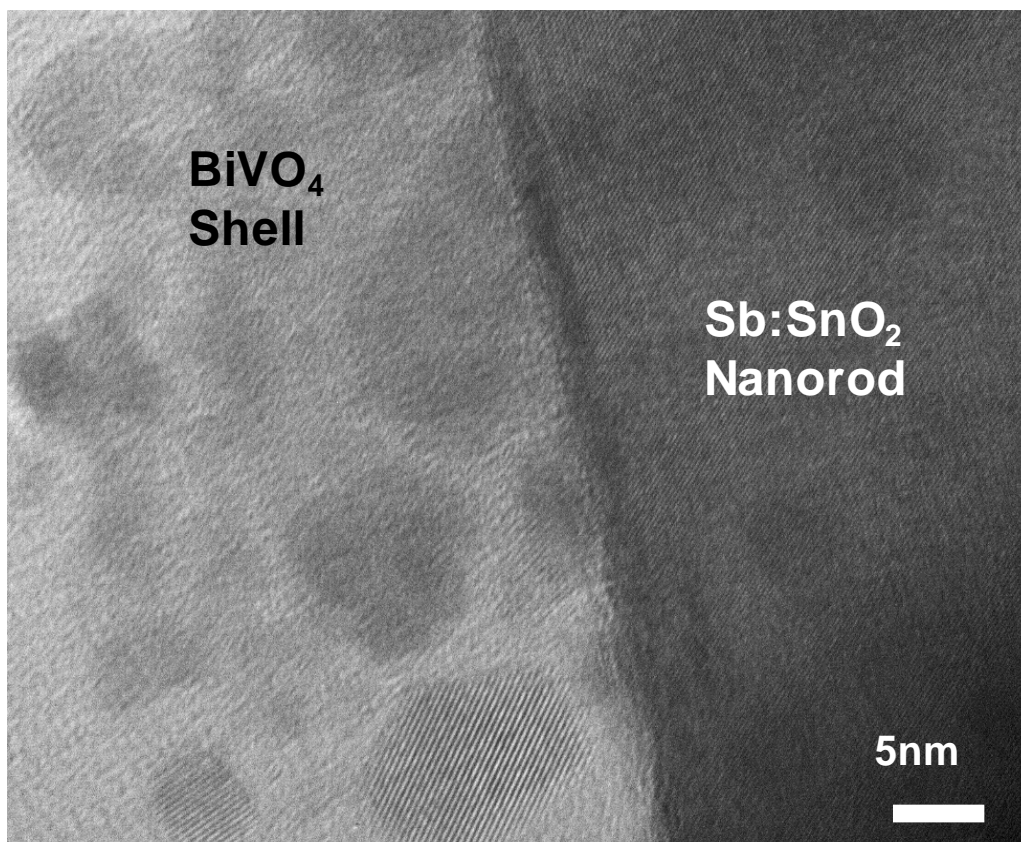
Figure 8. Transmission electron microscope image of $Sb:SnO_2$ nanorod coated with $BiVO_4$ shell.

The water photooxidation current of the Sb:SnO$_2$/BiVO$_4$ NRAs can be expressed as $J_{H2O} = J_{max} \times \eta_{abs} \times \eta_{sep} \times \eta_{trans}$.[27] We determine J_{max} by integrating the incident spectral irradiance over all wavelengths below 515 nm, which is the band edge of BiVO$_4$, and determine η_{abs} by integrating the product of the incident spectral irradiance and the light harvesting efficiency (LHE, the fraction of absorbed light) at each wavelength, and dividing by J_{max}. The simulated solar illumination in this study was provided by a Xe lamp (Model 6258, Oriel) equipped with an AM1.5G filter (Model 81094, Oriel), and the spectral irradiance was measured by a spectrometer (Model USB2000+Rad, Ocean Optics). The spectral irradiance of the Xe lamp solar simulator measured at the photoanode location, as well as the spectral irradiance of AM 1.5G standard illumination are all plotted in Figure 9. The wavelength-dependent LHE of the photoanode was measured using an integrating sphere with white-light illumination from the Xe lamp, and calculated from the measured reflection (R) and transmission (T) as LHE (λ) (%) = 100% - R (λ) (%) - T (λ) (%). The measurements were made with light incident on the glass-side of the photoanode (referred to as "back"), or incident on the side of the Sb:SnO$_2$/BiVO$_4$ NRAs (referred to as "front"). For the transmission measurements, the photoanode was placed at the front port of the sphere, and the transmittance spectrum was referenced to that of the empty port.
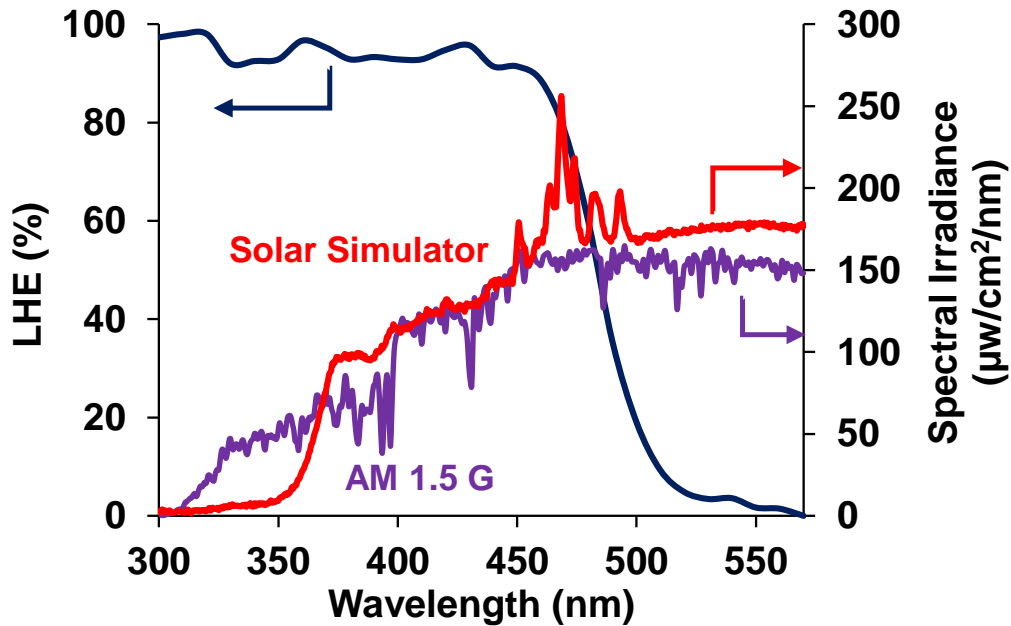
Figure 9. Light harvesting efficiency (LHE) of Sb:SnO$_2$/BiVO$_4$ (3 layers) core/shell NRAs (blue), and spectral irradiance of Xe lamp solar simulator (red) and standard AM 1.5G solar spectrum (purple).

The front- and back-side LHE of the Sb:SnO$_2$/BiVO$_4$ NRAs synthesized using 3 layers of BiVO$_4$ are plotted in Figure 10a. Integration of the spectral irradiance of the solar simulator over the range 300 - 515 nm gives J$_{max}$ of 7.97 mA/cm^2. Integration of the product of back-side LHE of the Sb:SnO$_2$/BiVO$_4$ NRAs and the spectral irradiance of the Xe lamp over the range 300 - 515 nm gives 5.74 mA/cm^2, which yields η$_{abs}$ of 72.0 %. Integration of the product of front-side LHE of the Sb:SnO$_2$/BiVO$_4$ NRAs and the spectral irradiance of the Xe lamp over the same range gives 5.81 mA/cm^2, which yields η$_{abs}$ of 72.9 %. The LHE of the FTO substrate and the Sb:SnO$_2$ NRs without BiVO$_4$ coating were also measured under back-side illumination, and are provided in Figure 11a. The FTO and Sb:SnO$_2$ NRs absorb strongly below 320 nm and weakly up to 400 nm, but have almost no absorption above 400 nm. Therefore, the high values of LHE in the 320 - 450 nm range indicate that there is strong light absorption in the BiVO$_4$ shells. This is despite the BiVO$_4$ coating thickness being significantly smaller than the light absorption depth of ~250 nm in BiVO$_4$ at 450 nm wavelength,[9] which can be explained by the long optical path in the axial direction of the NRs. The back-side LHE of Sb:SnO$_2$/BiVO$_4$ NRAs synthesized using 2 and 4 layers are provided in Figure 12e.

The PEC performance of the Sb:SnO$_2$/BiVO$_4$ NRAs was evaluated by measuring the current density-voltage (J-V) curve (i.e. linear sweep voltammogram) and wavelength-dependent incident photo-to-current conversion efficiency (IPCE) under both front-side (electrolyte-side) and back-side (glass-side) illumination in a three-electrode configuration using a potentiostat (Model SP-200, BioLogic), with the photoanode as working electrode, a saturated calomel electrode (SCE) as the reference electrode and a Pt wire as the counter electrode. The entire exposed area of the photoanode (1.44cm^2) was used in all calculations of photocurrent density. The J-V curve was measured at a scan rate of 10 mV/s and the IPCE was measured at a voltage of 0.6 V$_{RHE}$. Since our goal is to measure the η$_{abs}$ × η$_{sep}$ product rather than the photocurrent for water oxidation (J$_{H2O}$), both the J-V curve and the IPCE were measured in 0.5M potassium phosphate aqueous solution buffered to pH 7, with 1M sodium sulfite (Na$_2$SO$_3$) added as a hole scavenger. Because of the fast oxidation kinetics of sulfite, the surface charge transfer efficiency of the photoanode (η$_{trans}$) is nearly equal to 100%, allowing the η$_{abs}$ × η$_{sep}$ product to be calculated from η$_{abs}$ × η$_{sep}$ ≈ J$_{sulfite}$/J$_{max}$, where J$_{sulfite}$ is the photocurrent density for sulfite oxidation. Although sulfite photo-oxidation has been used in several studies to extract η$_{abs}$ × η$_{sep}$,[5, 6, 24, 32] we have performed Mott-Schottky measurements to verify that the presence of

45

sulfite does not alter the surface band energies of $BiVO_4$ by checking that the flat-band potential of $BiVO_4$ is the same in the presence of sulfite as it is in the pH 7 phosphate buffer alone. (Figure 13)
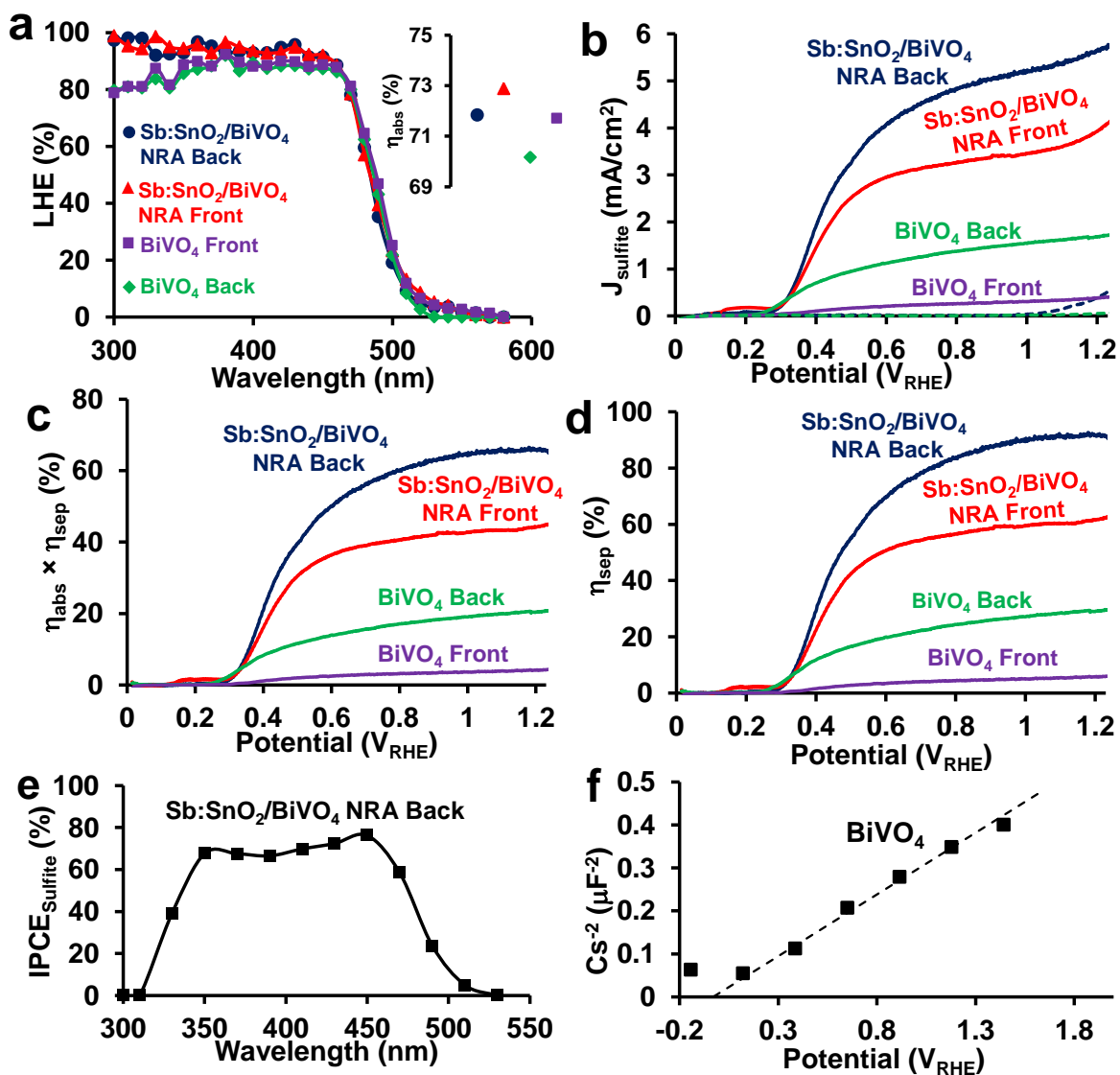
Figure 10. Optical and photoelectrochemical performance of $Sb:SnO_2$ NRAs coated with 3 layers of $BiVO_4$ ($Sb:SnO_2/BiVO_4$ NRA), and same-mass $BiVO_4$ film deposited directly onto FTO substrate without any NRAs ($BiVO_4$). For a-d, $Sb:SnO_2/BiVO_4$ NRA with back-side and front-side illumination are shown in blue and red, respectively, while $BiVO_4$ with back-side and front-side illumination are shown in green and purple, respectively. a) Light harvesting efficiency (LHE) and inset showing integrated light absorption efficiency (η_{abs}). b) Photocurrent for sulfite oxidation ($J_{sulfite}$) measured using a 3-electrode configuration in aqueous phosphate buffer (pH 7) with 1M

Na_2SO_3. Dark currents for $Sb:SnO_2/BiVO_4$ NRA and $BiVO_4$ are shown as blue and green dashed lines, respectively. c) Product of light absorption and charge separation efficiency ($\eta_{abs} \times \eta_{sep}$) versus potential, with dark currents subtracted. d) Charge separation efficiency (η_{sep}) with dark current subtracted. e) Incident photon-to-current efficiency (IPCE) of $Sb:SnO_2/BiVO_4$ core/shell NRAs measured under back-side illumination at 0.6 V_{RHE}. f) Mott-Schottky plot of planar non-porous film $BiVO_4$ measured using a 3-electrode configuration in aqueous phosphate buffer (pH 7) with 1M Na_2SO_3.
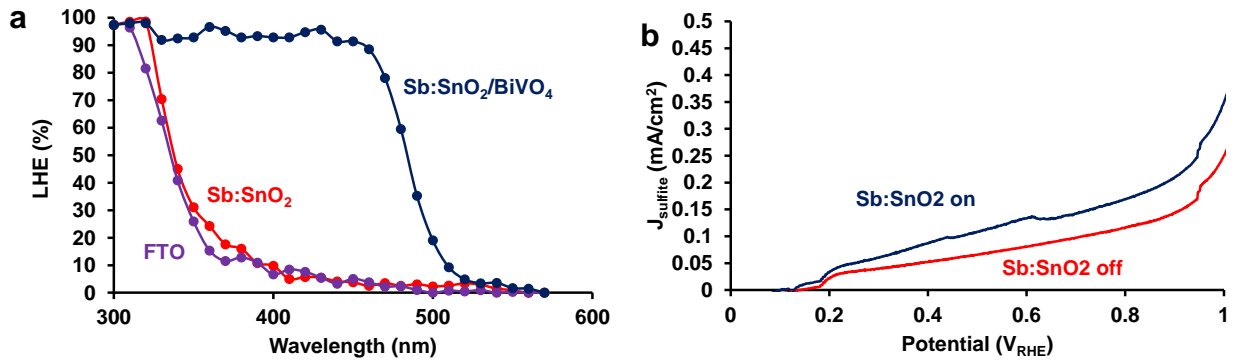
Figure 11. (a) Light harvesting efficiency (LHE) of $Sb:SnO_2/BiVO_4$ core/shell NRAs (blue), Sb:SnO2 NRAs (red) and FTO (purple); (b) Plots of current density ($J_{sulfite}$) versus potential (V) for $Sb:SnO_2$ NRAs under illumination (blue) and in the dark (red), measured using a 3-electrode configuration in aqueous phosphate buffer (pH 7) with 1M Na_2SO_3.

Out of the $Sb:SnO_2/BiVO_4$ NRA photoanodes synthesized with 2, 3 and 4 layers of $BiVO_4$, the photoanode with 3 layers of $BiVO_4$ produced the highest photocurrent for sulfite oxidation ($J_{sulfite}$) at a potential of 0.6 V_{RHE}. As shown in the J-V curve (Figure 10b), $J_{sulfite}$ under back-side illumination with dark current subtracted is 4.08 mA/cm^2 and 5.3 mA/cm^2 at 0.6 V_{RHE} and 1.23 V_{RHE}, respectively, which correspond to $\eta_{abs} \times \eta_{sep}$ products (Figure 10c) of 51.2% and 66.5% based on the J_{max} value of 7.97 mA/cm^2 obtained by the integration of the measured spectral irradiance of the Xe lamp solar simulator. We can also calculate η_{sep} (Figure 10d) by dividing the $\eta_{abs} \times \eta_{sep}$ product by the η_{abs} value of 72.0% calculated from the integration of the product of the LHE and the spectral irradiance of the Xe lamp solar simulator, yielding η_{sep} of 71.1% and 92.4% at 0.6 V_{RHE} and 1.23 V_{RHE}, respectively. Only about 1-2% of this photocurrent is generated in the $Sb:SnO_2$ NRAs, and the remainder is generated in the $BiVO_4$ shell. During back-side illumination, light first passes through the glass and the ~500nm-thick FTO layer, then

through the $Sb:SnO_2$ NRAs, and then finally into the $BiVO_4$. The FTO layer absorbs 5.4% of the incident light with wavelength less than 515 nm (band edge of $BiVO_4$), but does not produce any photocurrent, which represents a loss of 0.43 mA/cm^2 photocurrent. The $Sb:SnO_2$ NRAs absorb an additional 0.8% of the incident light with wavelength less than 515 nm, which could generate a maximum of 0.064 mA/cm^2 photocurrent. The actual photocurrent generated by the $Sb:SnO_2$ NRAs without any $BiVO_4$ shell was also measured under back-side illumination, and is 0.052 mA/cm^2 at 0.6 V_{RHE} (with dark current subtracted), as reported in Figure 11b. Therefore, η_{sep} at 0.6 V_{RHE} for charges generated only in the $Sb:SnO_2$ NRAs is 81.3%, which is higher than that for charges generated in the $BiVO_4$ layer. The rest of the ~72% of absorbed light is absorbed in the $BiVO_4$ layer.

When illuminated from the front-side, the $Sb:SnO_2/BiVO_4$ NRA photoanode (3 layers of $BiVO_4$) produces $J_{sulfite}$ with dark current subtracted of 3.0 mA/cm^2 and 3.6 mA/cm^2 at 0.6 V_{RHE} and 1.23 V_{RHE}, respectively (Figure 10b), which correspond to $\eta_{abs} \times \eta_{sep}$ products (Figure 10c) of 37.6% and 44.9% and η_{sep} (Figure 10d) of 50.8% and 61.6%, which are lower than the corresponding values for back-side illumination. Front-illumintion has the benefit that it does not suffer from unproductive light absorption by the FTO layer, as back-illumination does. Nonetheless, the photocurrent under front-illumination is lower because of significantly lower charge separation efficiency. For comparison, LHE and η_{abs}, $J_{sulfite}$, $\eta_{abs} \times \eta_{sep}$, and η_{sep} are also plotted for the same mass of $BiVO_4$ (3 layers) drop-casted directly onto a planar FTO substrate without any NRAs for both front- and back-side illumination (Figure 10a-d). This photoanode consists of a porous $BiVO_4$ film with 400 nm total thickness and 250 nm average particle size (SEM images provided in Figure 14). At 0.6 V_{RHE}, the photocurrent of this porous film without any NRAs is ~14 times lower than that of the $Sb:SnO_2/BiVO_4$ core/shell NRA film under front-side illumination, and ~3.6 times lower under back-side illumination, and the photocurrent under front-side illumination is lower than that under back-side illumination.
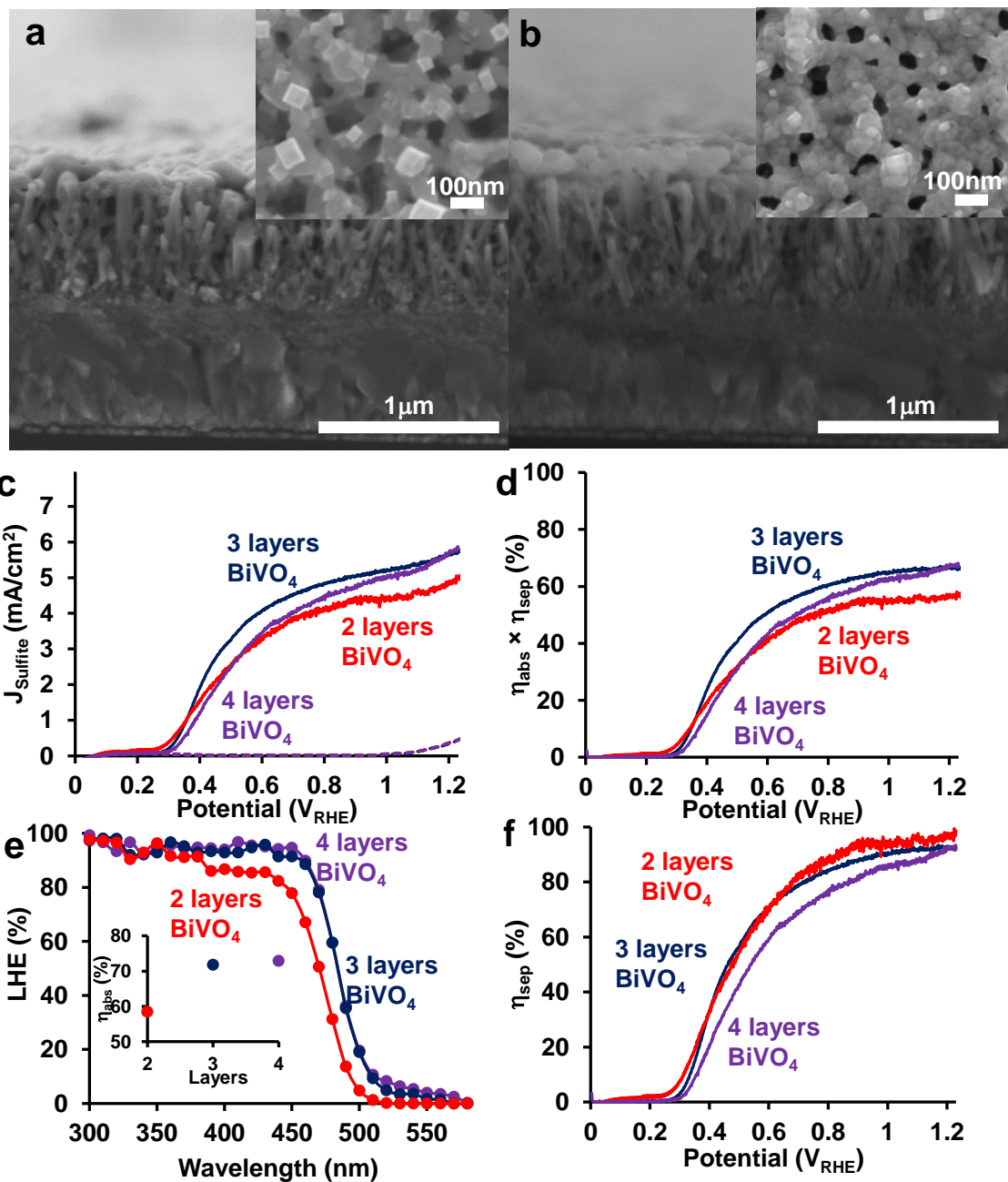
Figure 12. Scanning electron microscopy cross-section images (and inset top-view images) of (a) 2 layers and (b) 4 layers of BiVO$_4$ drop-casted onto Sb:SnO$_2$ NRAs. Performance of 2 layers (red), 3layers (blue) and 4 layers (purple) of BiVO$_4$ drop-casted onto Sb:SnO$_2$ NRAs for photoelectrochemical sulfite oxidation, measured using a 3-electrode configuration in aqueous phosphate buffer (pH 7) with 1M Na$_2$SO$_3$. (c) Plots of current density ($J_{sulfite}$) versus potential (V), dark current of Sb:SnO$_2$/BiVO$_4$ NRAs (dashed line), (d) product of light absorption and charge separation efficiency ($\eta_{abs} \times \eta_{sep}$) versus potential ($V$), (e) light harvesting efficiency (LHE) versus wavelength (and inset overall absorption efficiency - η_{abs} - versus numbers of BiVO$_4$ layers) and (f) charge separation efficiency (η_{sep}) versus potential (V).
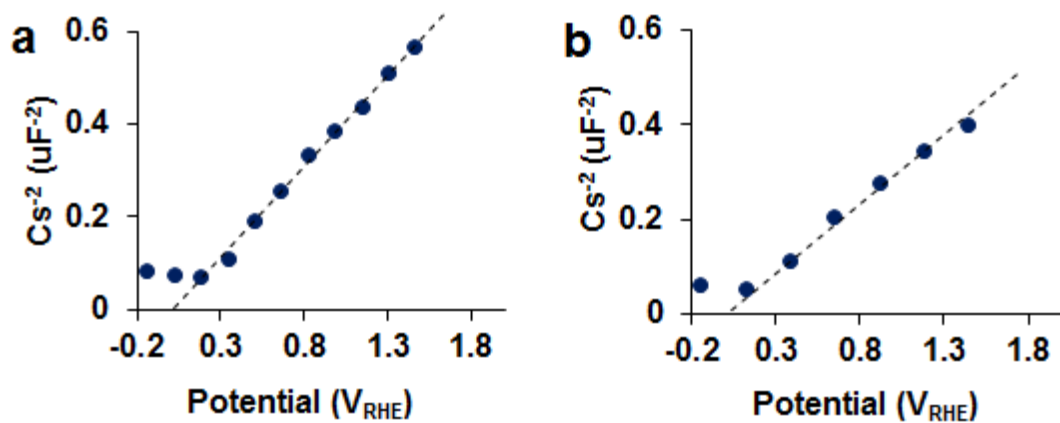
Figure 13. Mott-Schottky measurement (obtained at 10 kHz frequency, 20 mV amplitude, 5s equilibration time) of planar, non-porous film of $BiVO_4$ in (a) aqueous phosphate buffer (pH 7); (b) aqueous phosphate buffer (pH 7) with the addition of 1M Na_2SO_3. The presence of sulfite does not alter the surface band energies of $BiVO_4$.
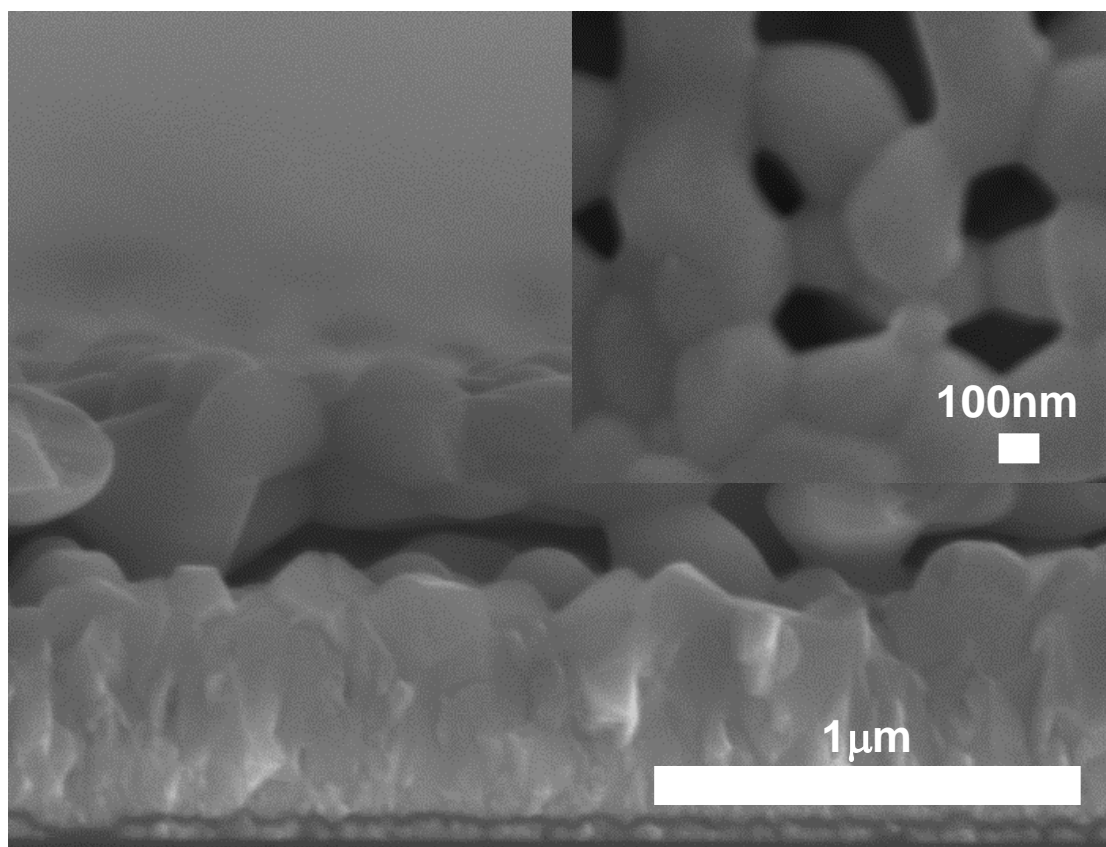
Figure 14. Scanning electron microscopy cross-section image (and inset top-view image) of 3 layers of porous $BiVO_4$ directly drop-casted onto a planar FTO substrate.

The IPCE of the Sb:SnO$_2$/BiVO$_4$ NRAs (3 layers of BiVO$_4$) for sulfite oxidation under back-side illumination at 0.6 V$_{RHE}$ (Figure 10e) was calculated from IPCE = [J$_{sulfite}$(mA/cm^2) × 1240(volt×nm)] / [P$_{mono}$ (mW/cm^2) × λ (nm)], where P$_{mono}$ is the intensity and λ the wavelength of the incident monochromatic light. The IPCE for sulfite oxidation is itself a measure of the η$_{abs}$ × η$_{sep}$ product at each wavelength (again assuming that η$_{trans}$ ≈ 100%), and peaks at 450nm, at a value of 76%. The IPCE at wavelengths below 350 nm is very low because the light is absorbed in the FTO layer of the substrate. This matches other studies of BiVO$_4$ in which light is incident through the FTO layer.[35] The photocurrent at 0.6 V$_{RHE}$ obtained by integrating the product of the measured IPCE and the spectral irradiance of the Xe lamp is ~4.1 mA/cm^2, which matches closely with the photocurrent of 4.08 mA/cm^2 obtained from the J-V curve under the simulated illumination. Moreover, the photocurrent at 0.6 V$_{RHE}$ obtained by integrating the product of the measured IPCE and the spectral irradiance of the standard AM 1.5G spectrum is ~3.9 mA/cm^2, which is also very similar.

The stability of the Sb:SnO$_2$/BiVO$_4$ NRA photoanode (3 layers of BiVO$_4$) for sulfite photo-oxidation at 0.6 V$_{RHE}$ was also measured, and is reported in Figure 15. There was almost no decrease in measured photocurrent after 2 hours of continuous operation. We have also measured the photocurrent generated by the Sb:SnO$_2$/BiVO$_4$ NRA photoanode (3 layers of BiVO$_4$) for photo-oxidation of water in aqueous 1M potassium borate (pH 9) solution without addition of sulfite, under back-side illumination (Figure 16a), which results in a modest photocurrent J$_{H2O}$ of 1.7 mA/cm^2 at 1.23V$_{RHE}$. Assuming 100% charge transfer efficiency for sulfite photo-oxidation (which resulted in 5.3 mA/cm^2 at 1.23 V$_{RHE}$) and taking the ratio of J$_{H2O}$/J$_{Sulfite}$, we therefore estimate the charge transfer efficiency (η$_{trans}$) for water photo-oxidation to be 32%. This value is to be expected since we have not added any OER catalyst to the surface of the BiVO$_4$, and is similar to those achieved by nanoporous BiVO$_4$ and WO$_3$/BiVO$_4$ core/shell nanowire photoanodes for water oxidation without the addition of OER catalysts.[6, 32] In addition, we have added a layer of NiFe-(oxy)hydroxide/borate OER catalyst to the surface of the Sb:SnO$_2$/BiVO$_4$ NRAs by photo-assisted electrodeposition, according to a published procedure.[38] With the OER catalyst, the Sb:SnO$_2$/BiVO$_4$ NRA photoanode achieves a photocurrent of ~2.9 mA/cm^2 at 0.6 V$_{RHE}$ under backside illumination in potassium borate buffer solution at pH 9, compared to ~4.1 mA/cm^2 for sulfite oxidation at the same potential (Figure S16a). We therefore estimate the charge transfer efficiency for water photo-oxidation by the

catalyst-coated photoanode to be ~71% at 0.6 V_{RHE}. The photocurrent achieved with the catalyst at 0.6 V_{RHE} is slightly lower than the state-of-the art value of ~3.2 mA/cm^2 achieved by nanoporous ("nanoworm") $BiVO_4$ at the same potential.[38] Finally, as shown in Figure 16b and c, we measured the oxygen evolved by the catalyst-coated $BiVO_4$ photoanode held at 0.6 V_{RHE} in potassium borate buffer solution at pH 9 over a duration of 30 minutes in a closed photoelectrochemical cell using a phase fluorimeter probe (NeoFox, Ocean Optics), according to a published procedure.[9] A stable photocurrent was obtained, and the faradaic efficiency for oxygen evolution was determined to be nearly 100%, which is consistent with a previous report.[38]
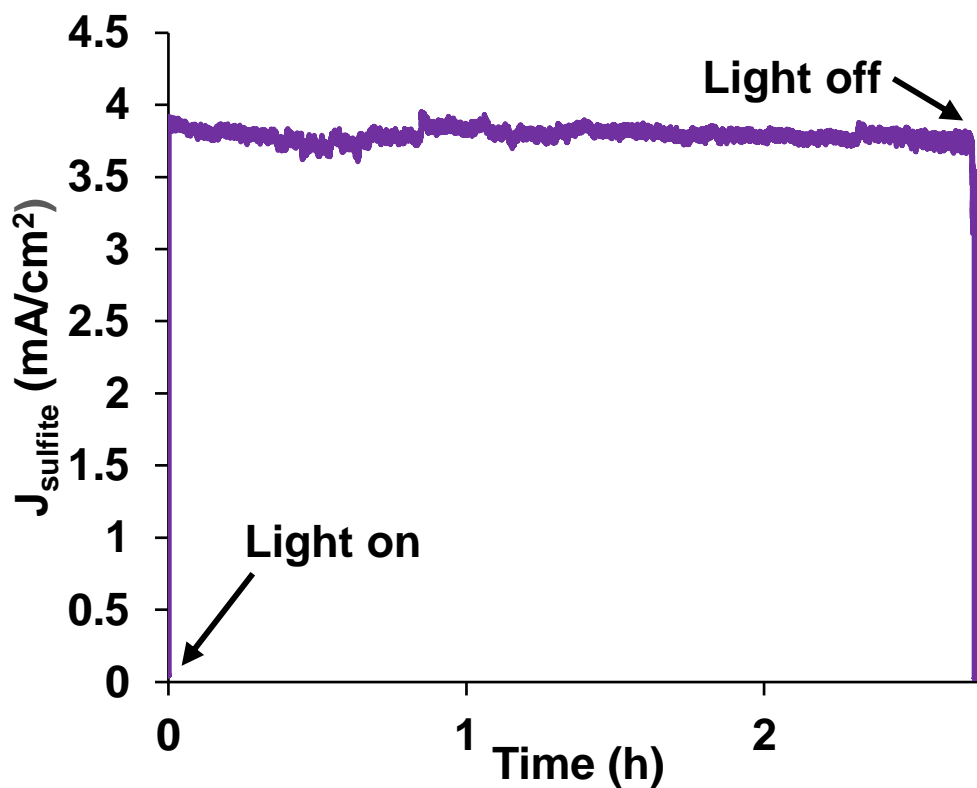
Figure 15. Stability measurement of Sb:SnO$_2$/BiVO$_4$ core/shell NRA photoanode, measured using a 3-electrode configuration in aqueous phosphate buffer (pH 7) with 1M Na$_2$SO$_3$ at 0.6V$_{RHE}$ under simulated solar illumination.
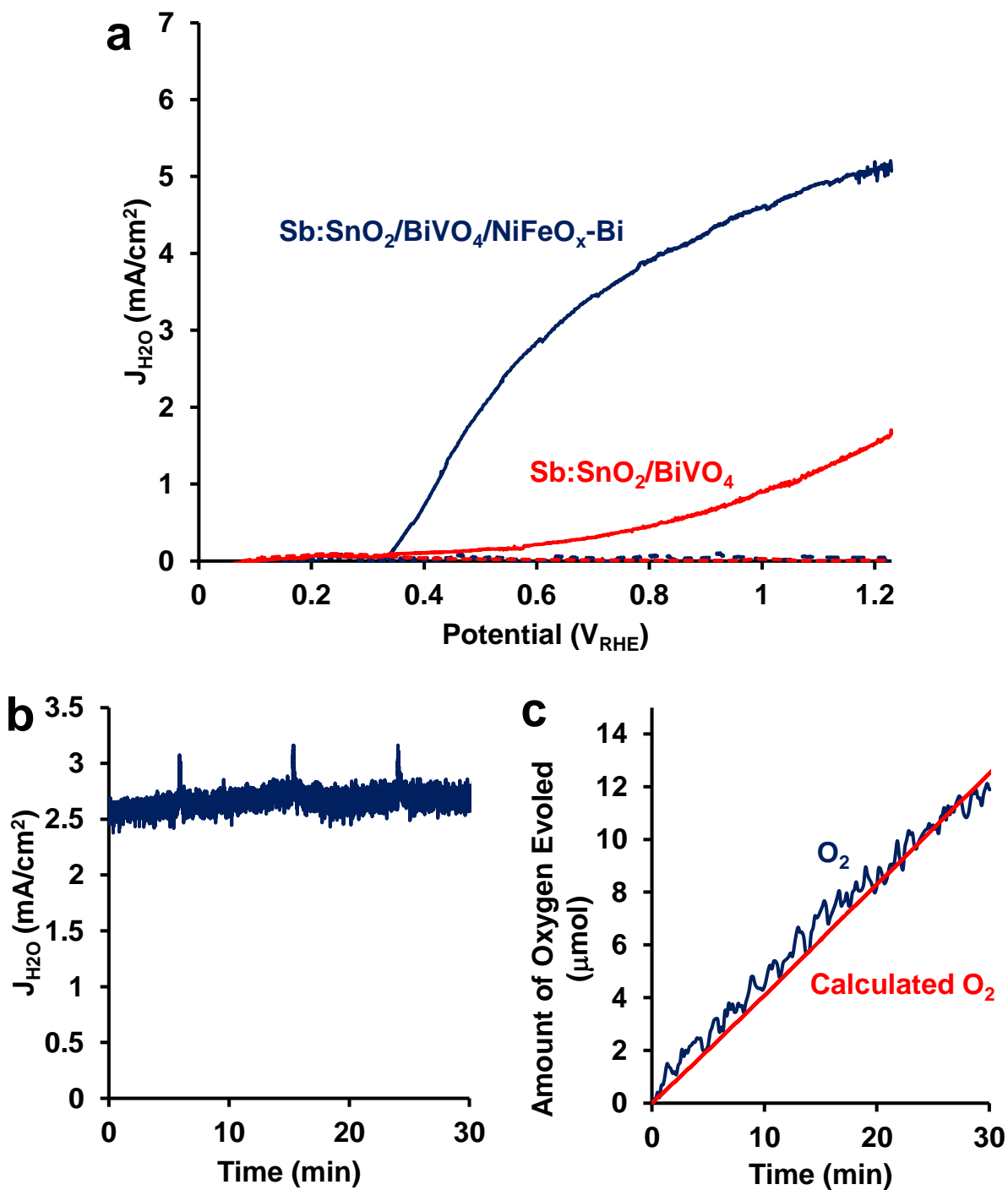
Figure 16. Performance of $Sb:SnO_2/BiVO_4$ and $NiFeOx-Bi/Sb:SnO_2/BiVO_4$ for photoelectrochemical water oxidation, measured using a 3-electrode configuration in aqueous 1M potassium borate (pH 9) solution (a) Plots of current density (J_{H2O}) versus potential (V) for $Sb:SnO_2/BiVO_4/NiFeO_x-Bi$ NRAs under illumination (blue) and in the dark (blue dashed) and $Sb:SnO_2/BiVO_4$ NRAs under illumination (red) and in the dark (red dashed). (b) Stability test of $NiFeOx-Bi/Sb:SnO_2/BiVO_4$ at $0.6V_{RHE}$ under illumination. (c) Oxygen evolution detected by a phase fluorimeter probe (blue) and oxygen calculated from photocurrent (red).

We have also reported LHE and η_{abs}, $J_{sulfite}$, $\eta_{abs} \times \eta_{sep}$, and η_{sep} vs. potential for the same Sb:SnO$_2$ NRAs coated instead with 2 and 4 layers of BiVO$_4$ in Figure 10. 2 layers of BiVO$_4$ was found to give slightly higher photocurrent than 3 layers at potentials below 0.4 V$_{RHE}$ due to improved η_{sep}, but lower photocurrent above 0.4 V$_{RHE}$ due to decreased η_{abs}, while 4 layers was found to give lower photocurrent than 3 layers below 1.2 V$_{RHE}$ due to increased BiVO$_4$ thickness and consequently poor η_{sep}, but slightly higher photocurrent above 1.2 V$_{RHE}$ due to comparable η_{sep} and slightly increased η_{abs}. We have also explored the growth of longer Sb:SnO$_2$ NRAs since drop-casting the same amount of BiVO$_4$ onto longer NRAs is expected to result in smaller BiVO$_4$ shell thickness and improved η_{sep} with no expected change in η_{abs}. However, the concurrent increase in the diameter of the NRs with length has so far resulted in NRAs that are too densely-packed, in which the drop-casted BiVO$_4$ forms a dense film with little remaining porosity. Modification of the synthesis conditions for the Sb:SnO$_2$ NRAs or an alternative method of synthesis could result in longer, higher-aspect-ratio NRAs with improved performance in the future.

Next, we aim to understand the influence of Sb-doping of the SnO$_2$ NRAs on the performance of the core/shell NRAs. For comparison, $J_{sulfite}$ and η_{sep} are plotted for the same mass of BiVO$_4$ drop-casted onto Sb-doped and undoped SnO$_2$ NRAs under back-side illumination (Figure 17a and 17b). The photocurrent of the Sb:SnO$_2$/BiVO$_4$ NRAs and undoped SnO$_2$/BiVO$_4$ NRAs is similar at very low potentials, but the Sb:SnO$_2$/BiVO$_4$ NRAs have higher performance at potentials of 0.6 and 1.23 V$_{RHE}$, which we hypothesize is due to improved electrical conductivity of the NRAs as a result of Sb doping. Conventional techniques such as four-point-probe measure only long-range conductivity of a NR array and cannot be used to characterize intrinsic conductivity of NRs. To study carrier dynamics over nanometer length scales, we have used terahertz time-domain spectroscopy (THz-TDS). A contact-free probe of complex conductivity, THz-TDS provides information about intrinsic conductivity within the individual NRs as well as about interconnectedness of the conducting NR network, as it probes microscopic conductivity within the NR array averaged across ~ 2 mm^2 area.[39-45]

THz pulses were generated by optical rectification of 800 nm, 100 fs pulses from a 1 kHz amplified Ti:sapphire laser source in a [110] ZnTe crystal, and coherently detected by free-space electro-optic sampling in a second [110] ZnTe crystal. Complex-valued THz conductivity is obtained by comparing the amplitude and the phase of the THz-pulse electric field waveform

transmitted through Sb:SnO$_2$ and undoped SnO$_2$ NRA films grown on a fused quartz substrate to a reference waveform transmitted through the bare substrate. THz-TDS probes AC-conductivity over the characteristic length $L = \sqrt{2D/f}$, where D is the diffusion coefficient, and f is the THz probing frequency.[39, 46] Calculating D using a carrier mobility of ~ 100 cm^2/Vs in undoped single crystal SnO$_2$,[47] we estimate L to be in the 15-50 nm range for a THz pulse bandwidth of 0.2 – 2.2 THz, which is smaller than a typical NR diameter. The complex THz conductivity spectra of Sb-doped and undoped SnO$_2$ NRAs are plotted in Figure 17c and 17d, respectively, with red squares and blue circles corresponding to real and imaginary components of the conductivity, respectively. Modeling complex THz conductivity with a Drude-Smith model, which takes into account confinement of carriers to distances comparable to the carrier mean free path, allows us to extract carrier density, scattering time, and to assess interconnectivity between NRs. Drude-Smith conductivity is given by

$$\sigma_{DS}(\omega) = \frac{n_{film}e^2\tau_{DS}/m*}{1-i\omega\tau}\left[1+\frac{c}{1-i\omega\tau_{DS}}\right]$$

where n_{film} is carrier density averaged across the ~ 2 mm^2 area, τ_{DS} is the Drude-Smith carrier scattering time, which takes into account both bulk and interface scattering, $m*$ is the effective mass of electrons, which is taken to be 0.3m$_e$,[48] and c is a parameter that accounts for the degree of carrier localization, varying from 0 for free carriers to -1 for fully localized carriers.[46, 49-52] Lines in Figure 17c and 17d are Drude–Smith model fits to the THz conductivity. We find that scattering time is 8.7 fs, which is about a factor of 2 lower than the bulk scattering rate of 17.6 fs calculated from a literature value of the electron mobility in undoped single-crystal SnO$_2$.[47, 48] This is expected due to the lower crystallinity in these NRs grown at lower temperature than that at which the measured single crystals were grown, as well as due to the contribution of Sb dopants and NR boundaries. We find that carriers are strongly localized within the NRs, as evidenced by the strongly suppressed real conductivity at low probing frequencies, and represented by the Drude-Smith c-parameter that is close to -1. This is expected since we are probing the conductivity in the plane of the substrate, perpendicular to the NR axes. Averaged film carrier density values obtained from Drude-Smith fits are 20.5 ± 2.3 × 10^{19} cm^{-3} for the Sb-doped SnO$_2$ NRAs, and 4.6 ± 0.9 × 10^{19} cm^{-3} for the undoped SnO$_2$ NRAs. The electron density within the NRs, n_{NRs}, can be calculated as $n_{NRs} = n_{film}(\rho_{bulk}/\rho)$ using the filling fraction ρ_{bulk}/ρ

that we estimate from the SEM micrographs to be ~0.5.[39] Finally, we calculate intrinsic conductivity within the Sb-doped and undoped SnO_2 NRs in the absence of structural confinement as $\sigma_{intrinsic} = \dfrac{n_{NRs} e^2 \tau_{DS}}{m*}$. In this calculation, we assume that bulk scattering is the dominant contribution to the Drude-Smith scattering time, while the boundary scattering is negligible as we are probing conductivity over 15-50 nm range, which is smaller than a typical NR diameter. The resulting intrinsic conductivity values are 33.2 ± 6.4 S/cm for the Sb-doped, and 7.4 ± 1.8 S/cm for the undoped SnO_2 NRs.
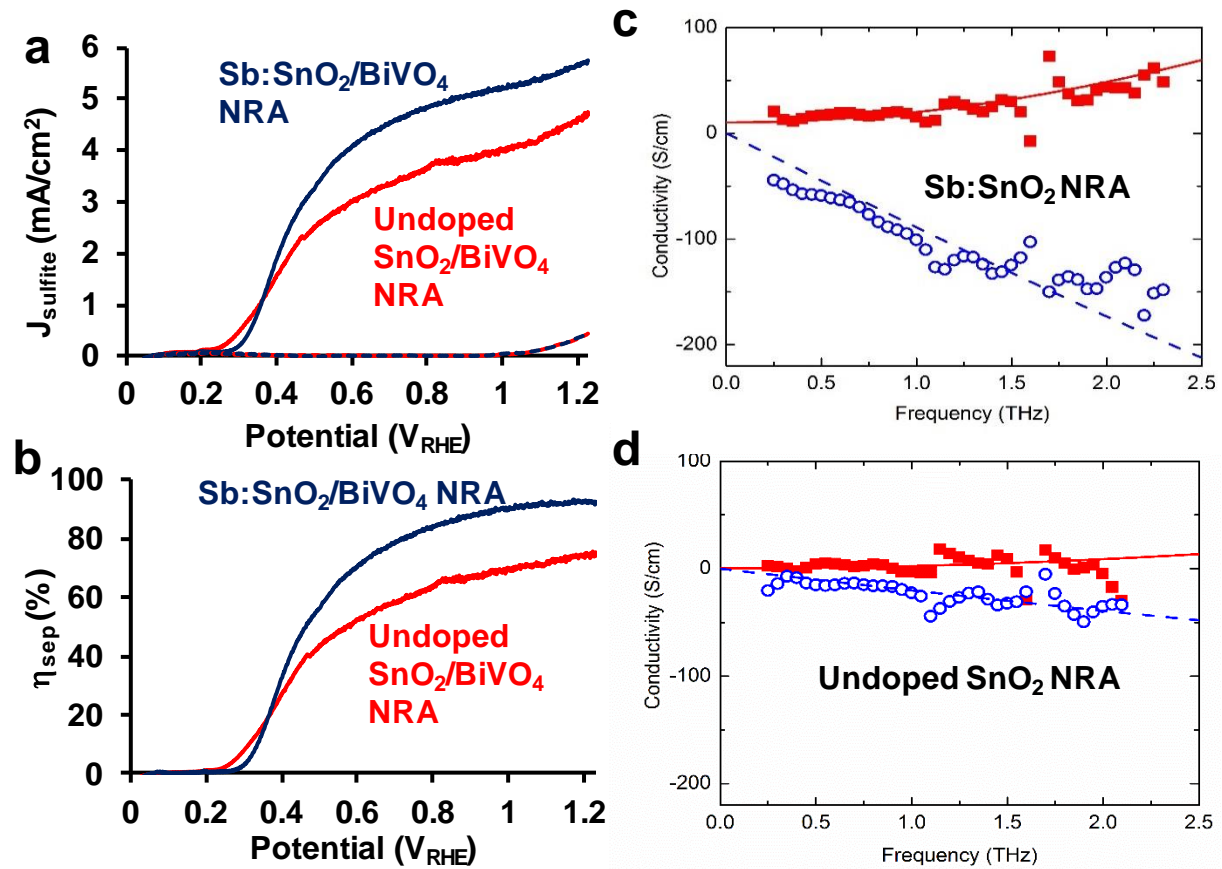
Figure 17. Performance of Sb-doped SnO_2 (Sb:SnO_2) and undoped SnO_2 NRAs coated with 3 layers of $BiVO_4$ for photoelectrochemical sulfite oxidation, measured using a 3-electrode configuration in aqueous phosphate buffer (pH 7) with 1M Na_2SO_3, under back-side illumination. a) Photocurrent ($J_{sulfite}$) and b) charge separation efficiency (η_{sep}) vs potential for the case in which the SnO_2 NRAs are Sb-doped (blue) and undoped (red). Complex THz conductivity spectra of c) Sb-doped and d) undoped SnO_2 NRAs, with red squares and blue circles corresponding to real and imaginary components of the conductivity, respectively.

56

However, we found that the high charge separation efficiency can only be achieved under back-side illumination. That is because the $BiVO_4$ coating is not uniform. In $Sb:SnO_2/BiVO_4$ NRAs, $BiVO_4$ coating has bridging between nanorods and accumulation on the top of nanorods. Both of these damaged the performance of the photoanode, especially under front illumination. That is because under front illumination, most of the photoexcited electrons are generated in the $BiVO_4$ surface layer, and need to travel across the whole layer to be collected. Recall that at 0.6 V_{RHE}, the maximum $BiVO_4$ thickness for high efficiency is about 60 nm. The thickness of $BiVO_4$ at the top of these nanorods is definitely larger than 100 nm, due to accumulation. Therefore, most of the photoexcited electrons can not be collected. However, under back-side illumination, most of the photoexcited electrons are generated at the $BiVO_4/Sb:SnO_2$ interface. Because there is no $BiVO_4$ accumulation close to the root of nanorods, most of the photoexcited electrons can be collected. The efficiency is only lost in the bridging part of the coating. The reason that we do not have the uniform coating was because the hydrothermal growth of $Sb:SnO_2$ is uncontrollable. As we increased the growth time to get longer nanorods, the spacing between the nanorods became too small. Moreover, we could not decrease the nanorod packing density by decreasing the seed layer concentration because the FTO substrate is F-doped SnO_2, which is very similar to $Sb:SnO_2$. So, in the hydrothermal growth, the exposed part of FTO between the seed particles also grew along with the nanorods and formed large isotropic crystals. (Figure 18)
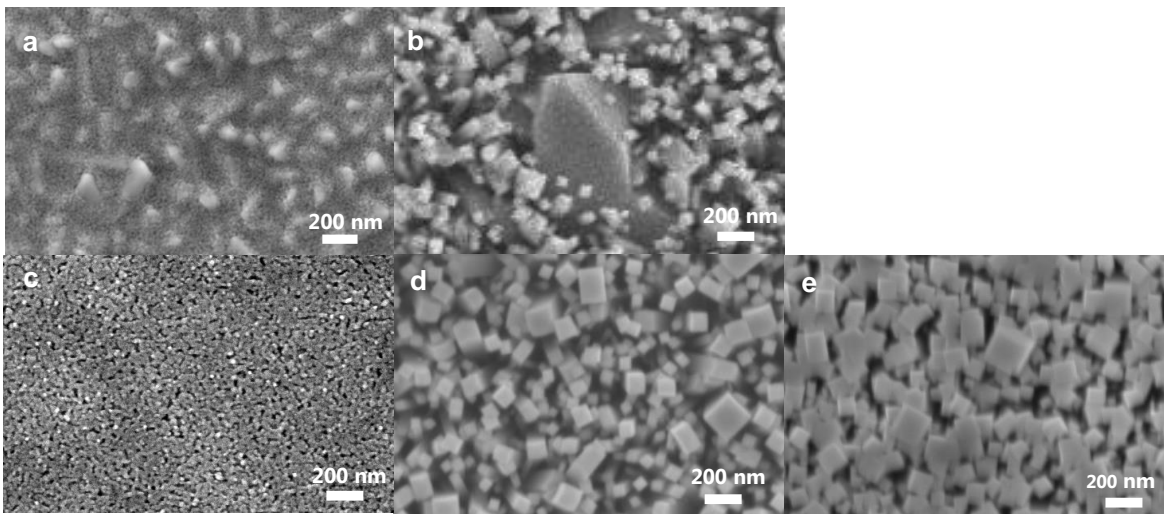
Figure 18. Scanning electron microscopy top-view images of a) FTO partially covered by SnO_2 seed layer; b) FTO partially covered by SnO_2 seed layer after 10 hours hydrothermal growth; c) FTO fully covered by SnO_2 seed layer;

d) FTO fully covered by SnO_2 seed layer after 10 hours hydrothermal growth; e) FTO fully covered by SnO_2 seed layer after 16 hours hydrothermal growth.

2.5 Results and Discussions of Sb:SnO₂ nanotubes/BiVO₄ Photoanodes

In order to solve the problem of uncontrollable growth of $Sb:SnO_2$ NRAs, we adopted a two-step approach involving the use of ZnO nanowires as templates. Instead of directly synthesizing $Sb:SnO_2$ NRAs, we firstly synthesized ZnO nanowires by hydrothermal growth, which was adapted from several previous reports, [53, 54] and used these ZnO nanowires as templates to synthesize $Sb:SnO_2$ nanotubes.

The morphologies and crystal structures of the core/shell $Sb:SnO_2/BiVO_4$ nanotubes on FTO substrates were characterized by scanning electron microscopy (SEM, JEOL 7000F, 5 kV) and X-ray diffraction (XRD, PANalytical Empyrean, Cu-kα, 45 kV, 40 mA). Monoclinic $BiVO_4$ and tetragonal SnO_2 are the only phases detected by XRD for the $Sb:SnO_2/BiVO_4$ nanotubes grown on FTO substrates (Figure 19). The absence of ZnO patterns in $Sb:SnO_2$ nanotubes/FTO indicates that the ZnO nanowires were dissolved in acetic acid during the etching process and almost no ZnO was present in the $Sb:SnO_2/BiVO_4$ nanotube photoanodes.

According to SEM images (Figure 20a and 20d), the ZnO nanowire templates are quasi-aligned to the FTO substrates. After 10 hours of growth, the length of ZnO nanowires ranges from 2.5 µm to 4.5 µm, with an average of 3.5 µm. The top and bottom diameters of the tapered nanowires are about 70 nm and 140nm, respectively, and the average inter-rod spacing is about 500 nm. After two times drop-casting of 5 layers of $Sb:SnO_2$, annealing, acetic acid etching and DI water washing, the ZnO nanowires were fully dissolved in the acetic acid solution and were washed away from the substrates. However, the $Sb:SnO_2$ coating kept its original shape with slightly increased top (80nm) and bottom (160nm) diameters and nanowire-shaped void space inside the nanotubes (Figure 20b and 20e). After 4 layers $BiVO_4$ drop casting and annealing, hemispherical $BiVO_4$ particles are uniformly coated on the $Sb:SnO_2$ nanotubes with an average diameter of about 50 nm and an average thickness of about 25 nm (Figure 21a-21d). This 25 nm-thick $BiVO_4$ coating is thin enough to allow most of the photo-excited electrons to transfer to the $Sb:SnO_2$ nanotube electron collectors without recombination. Figure 22 shows the synthesis

58

methods and the cross-section SEM images of the difference between our new Sb:SnO$_2$/BiVO$_4$ nanotubes and previous Sb:SnO$_2$/BiVO$_4$ nanorods. By controlling the ZnO seed layer concentration and growth time of ZnO nanowire templates, the inter-tube spacing of new Sb:SnO$_2$ nanotubes is increased from 170 nm to 500 nm and the length of the new Sb:SnO$_2$ nanotubes is increased from 1.0 µm to 3.5 µm. Figure 21e shows the structure schematic and energy band diagram of the new Sb:SnO$_2$/BiVO$_4$ nanotube arrays. The low packing density and long length nanotubes provided much larger space for the BiVO$_4$ coating which prevented the accumulation of BiVO$_4$ coating on the top of nanotubes and prevented the coating from bridging between nanotubes, as it did in the previous Sb:SnO$_2$/BiVO$_4$ nanorod photoanodes.
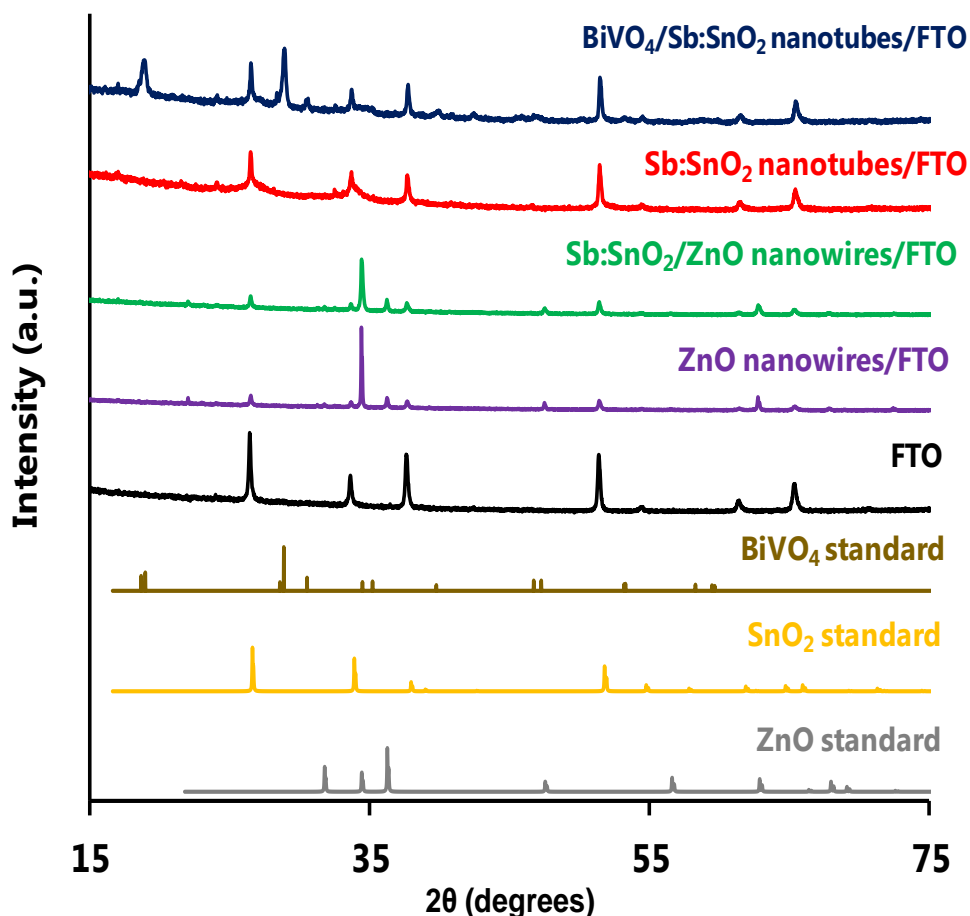
Figure 19. X-ray diffraction of standard ZnO pattern (grey), standard SnO$_2$ pattern (yellow), standard BiVO$_4$ pattern (brown), FTO (black), 10-hour-grown ZnO nanowires (purple), Sb:SnO$_2$ coated on ZnO nanowires (green), Sb:SnO$_2$ coated on ZnO nanowires after acetic acid etching of the ZnO, forming hollow Sb:SnO$_2$ nanotubes (red), and BiVO$_4$ coated onto the Sb:SnO$_2$ nanotubes to form Sb:SnO$_2$/BiVO$_4$ core/shell nanotubes (blue).
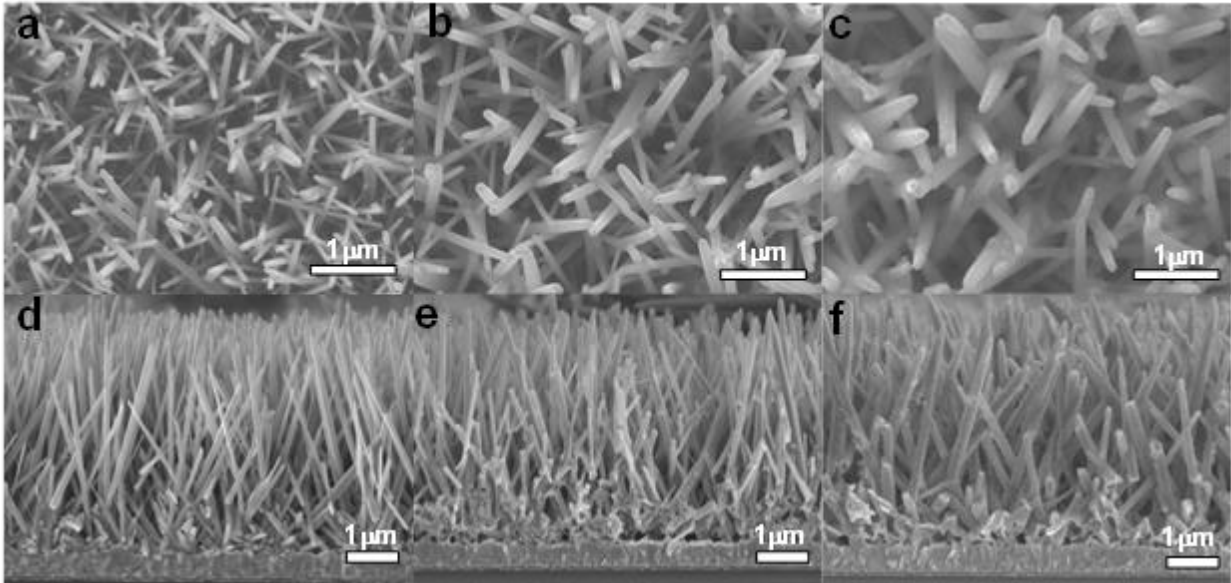
Figure 20. Scanning electron microscopy (SEM) of a) top and d) cross-section of ZnO nanowires, b) top and e) cross-section of Sb:SnO$_2$ nanotubes, c) top and f) cross-section of Sb:SnO$_2$/BiVO$_4$ nanotubes photoanode.
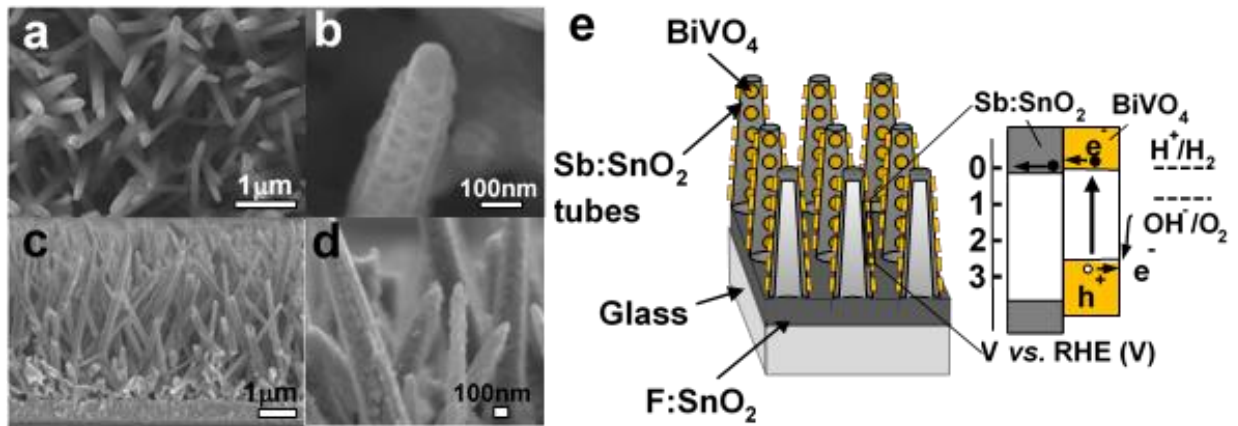
Figure 21. Scanning electron microscopy (SEM) top images of Sb:SnO$_2$/BiVO$_4$ nanotube arrays on FTO substrate at a) low and b) high magnification. SEM cross-section images of Sb:SnO$_2$/BiVO$_4$ nanotube arrays on FTO substrate at c) low and d) high magnification. e) Structure schematic and energy band diagram of the Sb:SnO$_2$/BiVO$_4$ nanotube arrays. These Sb:SnO$_2$/BiVO$_4$ nanotube arrays were obtained by using 10-hour-grown ZnO nanowire arrays as templates.
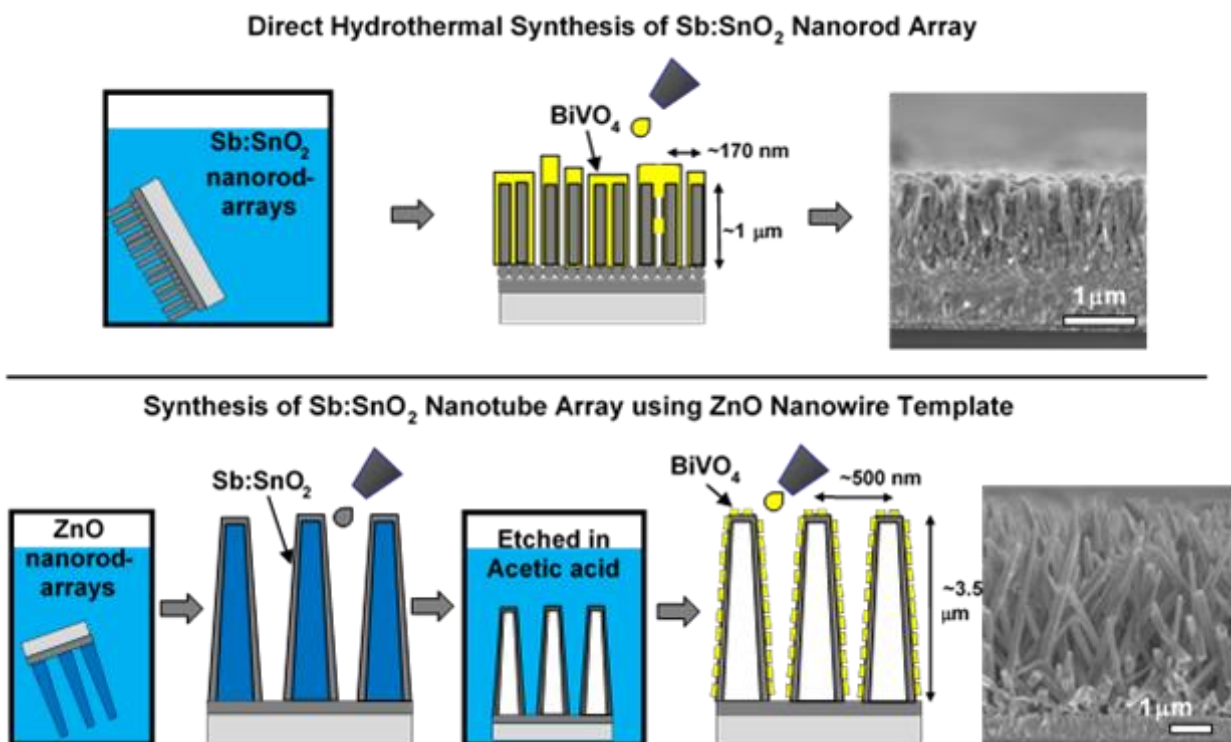
Figure 22. Synthesis procedure and scanning electron microscopy cross-section images of previous Sb:SnO$_2$/BiVO$_4$ nanorod arrays on FTO substrate (top) and new Sb:SnO$_2$/BiVO$_4$ nanotube arrays on FTO substrate (bottom), obtained using 10-hour-grown ZnO nanowires as a template.

The wavelength-dependent LHE of the photoanode was measured using an integrating sphere with white-light illumination from the solar simulator. The front- and back-side LHE of the Sb:SnO$_2$/BiVO$_4$ nanotubes and those of a photoanode made by drop-casting the same mass per area of BiVO$_4$ directly onto the FTO current collector to form a porous BiVO$_4$ film (FTO/BiVO$_4$) are plotted in Figure 23a. The η_{abs} of Sb:SnO$_2$/BiVO$_4$ nanotubes under front- and back-side illumination are 72.1% and 68.9%, and the η_{abs} of FTO/BiVO$_4$ under front- and back-side illumination are 65.6% and 66.2%. The η_{abs} of Sb:SnO$_2$/BiVO$_4$ nanotubes under front-side illumination is the highest among these four η_{abs} because the cone shaped nanotubes act as an anti-reflective layer.[55]

The J-V curves of Sb:SnO$_2$/BiVO$_4$ nanotubes for sulfite oxidation under front- and back-side illumination are plotted in Figure 23b. The Sb:SnO$_2$/BiVO$_4$ nanotube photoanodes achieved a photocurrent density for sulfite oxidation ($J_{sulfite}$) of 4.11 mA/cm^2 under front-side illumination and 4.26 mA/cm^2 under back-side illumination at 0.6 V$_{RHE}$. The J-V curves of FTO/BiVO$_4$ are

also plotted in Figure 23for comparison. A very high J_{front}/J_{back} ratio (0.96) was achieved by the Sb:SnO$_2$/BiVO$_4$ nanotube photoanodes compared to the FTO/BiVO$_4$ photoanode (0.30) and previously-reported BiVO$_4$ photoanodes (0.54 for nanoporous BiVO$_4$,[6] 0.62 for nanoporous Mo:BiVO$_4$ with H$_2$ treatment,[56] 0.69 for nanoporous BiVO$_4$ with N$_2$ treatment,[5] and 0.73 for Sb:SnO$_2$/BiVO$_4$ nanorods[34]). The surface charge transfer efficiency of the photoanode (η_{trans}) can be considered as 100% due to the fast oxidation kinetics of sulfite. Therefore, the product of $\eta_{abs} \times \eta_{sep}$ can be calculated from $\eta_{abs} \times \eta_{sep} \approx J_{sulfite}/J_{max}$. The $\eta_{abs} \times \eta_{sep}$-V curve of Sb:SnO$_2$/BiVO$_4$ nanotubes and FTO/BiVO$_4$ under front- and back-side illumination are plotted in Figure 23c. At 0.6 V_{RHE}, the Sb:SnO$_2$/BiVO$_4$ nanotubes achieved $\eta_{abs} \times \eta_{sep}$ products of 54.3% and 56.3% under front- and back-side illumination, which are 9.05 and 2.83 times as high as those of the FTO/BiVO$_4$ photoanode. At 1.23 V_{RHE}, the Sb:SnO$_2$/BiVO$_4$ nanotubes achieved $\eta_{abs} \times \eta_{sep}$ products of 65.2% and 68.9% under front- and back-side illumination, which are 7.33 and 2.26 times as high as those of the FTO/ BiVO$_4$ photoanode. These large improvements are results of the combination of high absorption efficiency provided by the long absorption path in the BiVO$_4$ coating along the nanotube axial direction and high separation efficiency provided by the thin and uniform BiVO$_4$ particle coating. The η_{sep}-V curves of Sb:SnO$_2$/BiVO$_4$ nanotubes and FTO/BiVO$_4$ under front- and back-side illumination were calculated by dividing the $\eta_{abs} \times \eta_{sep}$ product by the η_{abs} value, and are plotted in Figure 23d. The η_{sep} of Sb:SnO$_2$/BiVO$_4$ nanotube photoanodes reached 75.4% and 81.4% under front- and back-side illumination, which is 49.3% and 16.5% higher than the 50.5% and 69.9% η_{sep} achieved by the previous Sb:SnO$_2$/BiVO$_4$ nanorod photoanodes at 0.6 V_{RHE}. These improvements can be explained by the larger inter-tube distance in the Sb:SnO$_2$ nanotubes compared to the inter-rod distance in the previous Sb:SnO$_2$ nanorods, which minimized the bridging of the BiVO$_4$ coating across multiple tubes and prevented the accumulation of the BiVO$_4$ coating on the tops of the nanotubes.
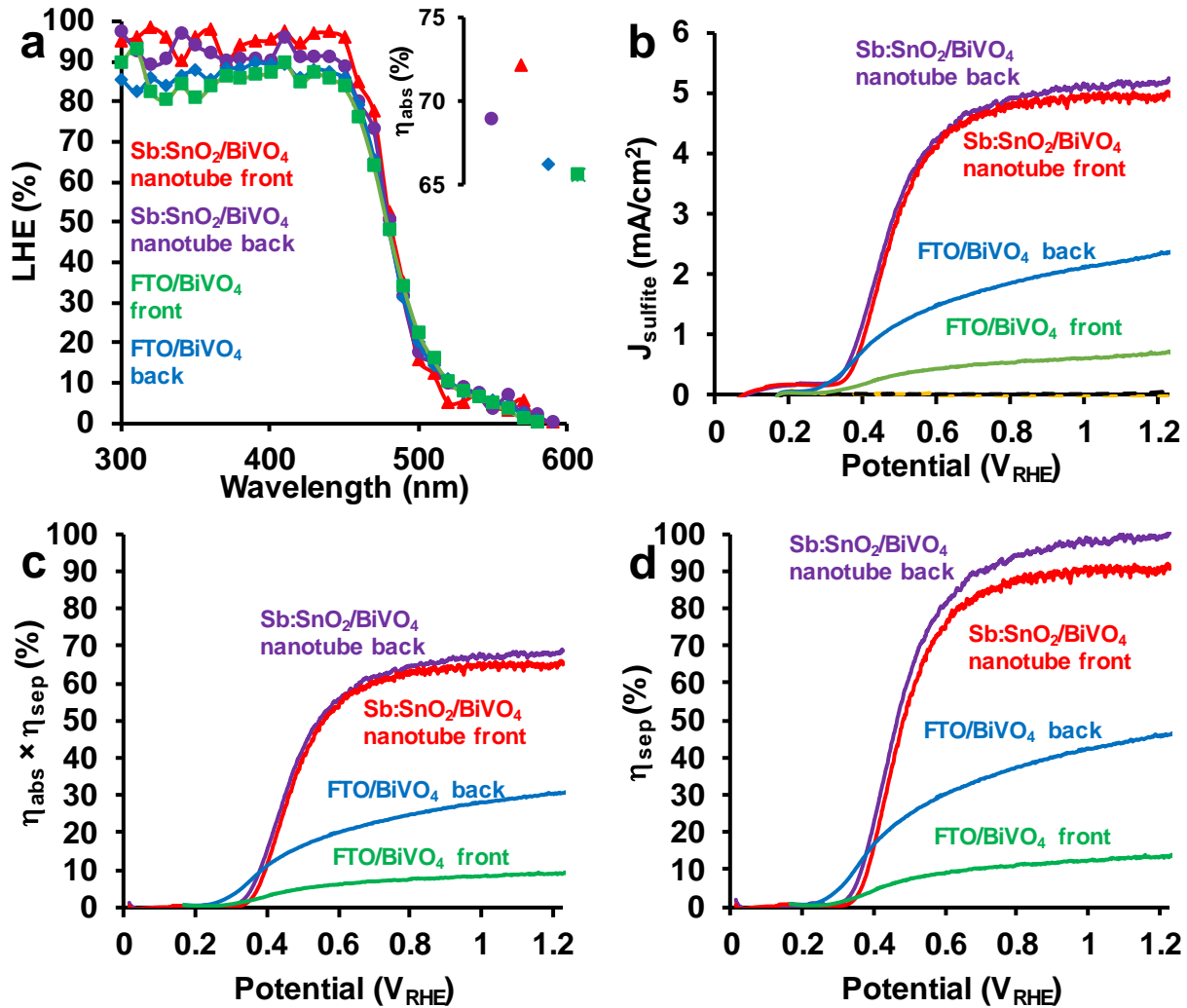
Figure 23. Optical and photoelectrochemical performance of Sb:SnO$_2$ nanotubes (obtained using 10-hour-grown ZnO nanowires as templates) coated with 4 layers of BiVO$_4$ (Sb:SnO$_2$/BiVO$_4$ nanotubes), and same-mass porous BiVO$_4$ film deposited directly onto FTO substrate (FTO/BiVO$_4$). For a-d, Sb:SnO$_2$/BiVO$_4$ nanotubes with back-side and front-side illumination are shown in purple and red, respectively, and FTO/BiVO$_4$ with back-side and front-side illumination are shown in blue and green, respectively. a) Light harvesting efficiency (LHE) and inset showing integrated light absorption efficiency (η_{abs}). b) Photocurrent for sulfite oxidation (J$_{sulfite}$) measured under simulated AM 1.5G illumination using a 3-electrode configuration in aqueous phosphate buffer (pH 7) with 1M Na$_2$SO$_3$. Dark currents for Sb:SnO$_2$/BiVO$_4$ nanotubes and FTO/BiVO$_4$ are shown as black and orange dashed lines, respectively. c) Product of light absorption and charge separation efficiency ($\eta_{abs} \times \eta_{sep}$) versus potential, with dark currents subtracted. d) Charge separation efficiency (η_{sep}) with dark current subtracted.

We additionally performed experiments to study the influence of Sb:SnO$_2$ nanotube length on the PEC performance, while keeping the total quantity of BiVO$_4$ fixed. Whereas the Sb:SnO$_2$ nanotubes in the Sb:SnO$_2$/BiVO$_4$ nanotube photoanodes mentioned until now were synthesized using ZnO nanowire templates that were grown for 10 hours, we additionally synthesized Sb:SnO$_2$/BiVO$_4$ nanotube photoanodes based on ZnO nanowires that were grown for

63

6, 8 and 12 hours (Figure 24) which had average lengths of 1.8, 2.4 and 4.1 µm, respectively, compared to the 3.5 µm average length of the 10-hours-grown ZnO nanowires. At 0.6 V_{RHE}, we found that the photoanodes obtained using the 6-hours-grown ZnO nanowires had the highest back-illumination photocurrent of 4.43 mA/cm^2 and the lowest front-illumination photocurrent of 3.77 mA/cm^2, and a ratio of front/back photocurrent of 0.85, which is less than one. On the other hand, the photoanodes obtained using the 12-hours-grown ZnO nanowires had the lowest back-illumination photocurrent of 4.24 mA/cm^2, the highest front-illumination photocurrent of 4.34 mA/cm^2, and a ratio of front/back photocurrent of 1.02, which is greater than one. To the best of our knowledge, both the back-illuminated photocurrent of 4.43 mA/cm^2 and the front-illuminated photocurrent of 4.34 mA/cm^2, both obtained under conditions of closely-calibrated simulated AM 1.5 G illumination, are records for BiVO$_4$ to date, and represent $\eta_{abs} \times \eta_{sep}$ products of 58.5% and 57.3% based on J_{max} of 7.57 mA/cm^2 obtained by integrating the spectral irradiance of the solar simulator over the range 300 - 520 nm. The trend of back-illumination photocurrent decreasing with increasing length of the Sb:SnO$_2$ nanotubes can be explained by increasing recombination at the Sb:SnO$_2$/BiVO$_4$ interface, since the interfacial surface area increases with the increasing length of the nanotubes and since photo-excited charges are generated close to this interface under back-illumination. Conversely, the trend of front-illumination photocurrent increasing with increasing length of the Sb:SnO$_2$ nanotubes can be explained by decreasing bulk recombination, since the thickness of the BiVO$_4$ layer is decreasing.

Since we are using ZnO nanowire templates to obtain the photoanodes in this study, we also synthesized photoanodes by depositing and annealing BiVO$_4$ directly onto the ZnO nanowires themselves, without first creating Sb:SnO$_2$ nanotubes (Figure 25), for comparison. The solvent we used to prepare the BiVO$_4$ drop-casting solution is acetic acid, which dissolves ZnO. Therefore, for this experiment, we changed the solvent to 2-methoxy ethanol, which does not damage ZnO. The resulting photoanode had good nanowire and BiVO$_4$ coating morphology but generated a sulfite oxidation photocurrent that was more than an order-of-magnitude smaller than those generated by the Sb:SnO$_2$ nanotube/BiVO$_4$ photoanodes. We expect that this decrease is due to detrimental and uncontrolled doping of Zn into BiVO$_4$ during annealing. We also performed experiments to illustrate the need for etching away the ZnO cores within the Sb:SnO$_2$ nanotubes before deposition of BiVO$_4$. We firstly prepared ZnO core/Sb:SnO$_2$ shell nanowires,
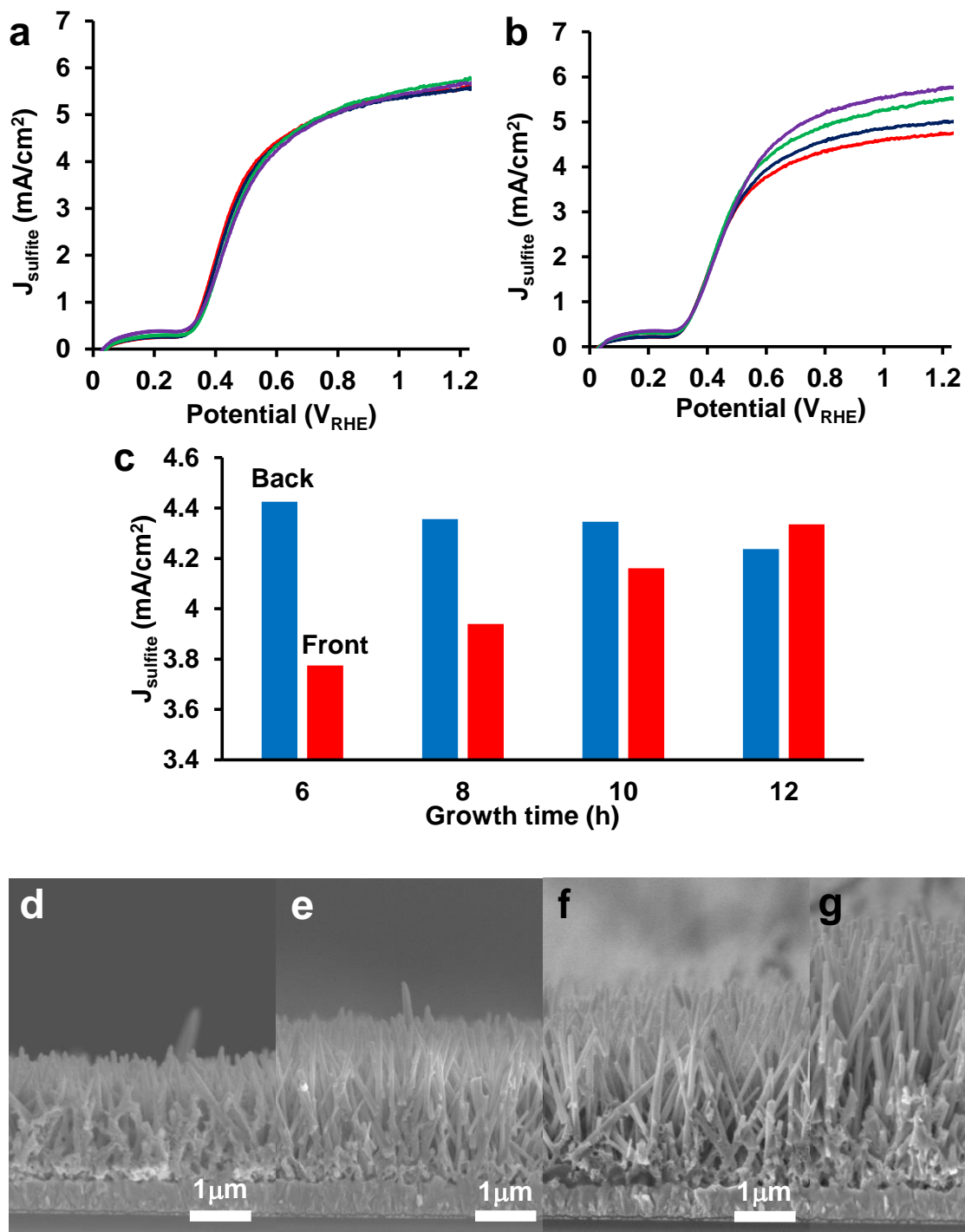
Figure 24. Photoelectrochemical performance and SEM cross-section images of Sb:SnO$_2$ nanotubes of different lengths (different growth time of ZnO nanowires that were used as templates) coated with the same amount (4 times drop-casting) of BiVO$_4$ to form Sb:SnO$_2$/BiVO$_4$ nanotubes. Photocurrent for sulfite oxidation (J$_{sulfite}$) measured using a 3-electrode configuration in aqueous phosphate buffer (pH 7) with 1M Na$_2$SO$_3$ under a) back-side and b) front-side simulated AM 1.5G illumination. Sb:SnO$_2$/BiVO$_4$ nanotubes obtained using ZnO nanowire templates that were grown for 6 h, 8 h, 10 h and 12 h are shown in red, blue, green and purple, respectively. c) Histogram summarizing photocurrent for sulfite oxidation (J$_{sulfite}$) at 0.6 V$_{RHE}$ under front- and back-side illumination. SEM cross-section images of Sb:SnO$_2$/BiVO$_4$ nanotubes obtained using ZnO nanowire templates that were grown for d) 6 h, e) 8 h, f) 10 h and g) 12 h.

then deposited an acetic acid solution of $BiVO_4$ onto these, and then annealed to obtain crystalline $BiVO_4$ (Figure 26). However, the acetic acid partially dissolved the ZnO, resulting in damaged structure and Zn incorporation into $BiVO_4$. The resulting photocurrents for sulfite oxidation were below 2.7 mA/cm^2 at 0.6 V_{RHE}. In addition, we also experimented with depositing a 2-methoxy ethanol solution of $BiVO_4$ onto the ZnO core/$Sb:SnO_2$ shell nanowires, so that the ZnO nanowires would not be damaged by the solvent, followed by annealing (Figure 27). The resulting photoanode had good nanowires and $BiVO_4$ coating morphology but generated photocurrents of less than 3.3 mA/cm^2 at 0.6 V_{RHE}. Again, these lower photocurrents compared to those of the $Sb:SnO_2$ nanotube/$BiVO_4$ photoanodes is likely due to Zn doping into the $BiVO_4$ during annealing, although it is not as severe as if the $Sb:SnO_2$ shell was not present. In contrast, the champion $Sb:SnO_2$ nanotube/$BiVO_4$ photoanodes synthesized here were obtained by drop-casting of 5 layers of $Sb:SnO_2$ onto the ZnO nanowires, annealing to crystallize the $Sb:SnO_2$, etching in acetic acid and washing in DI water to remove the ZnO nanowires and form $Sb:SnO_2$ nanotubes (which may contain some Zn due to diffusion from the ZnO nanowires during annealing), drop-casting and annealing an additional 5 layers of $Sb:SnO_2$ (which likely contains very low Zn content), followed by acetic acid and DI water wash, and deposition and annealing of $BiVO_4$, which then has negligible Zn doping. Therefore, removing the ZnO nanowires early in the fabrication process leads to the highest-performing $BiVO_4$ photoanodes.
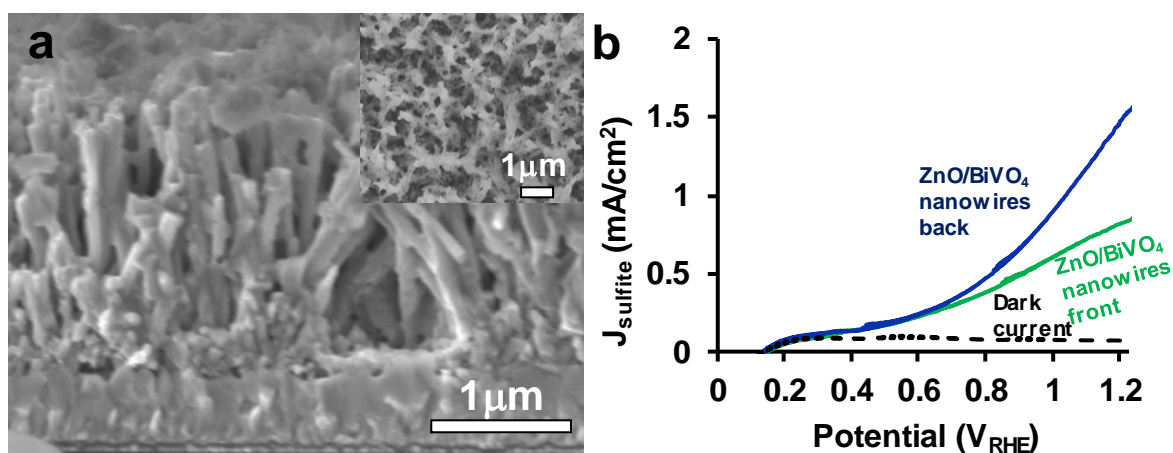
Figure 25. a) SEM images and b) J-V curves of $BiVO_4$ deposited directly onto 6-hr-grown ZnO nanowires using a 2-methoxy ethanol + acetylacetone solvent. Photocurrents are for sulfite oxidation ($J_{sulfite}$) measured under simulated AM 1.5 G illumination using a 3-electrode configuration in aqueous phosphate buffer (pH 7) with 1M Na_2SO_3.
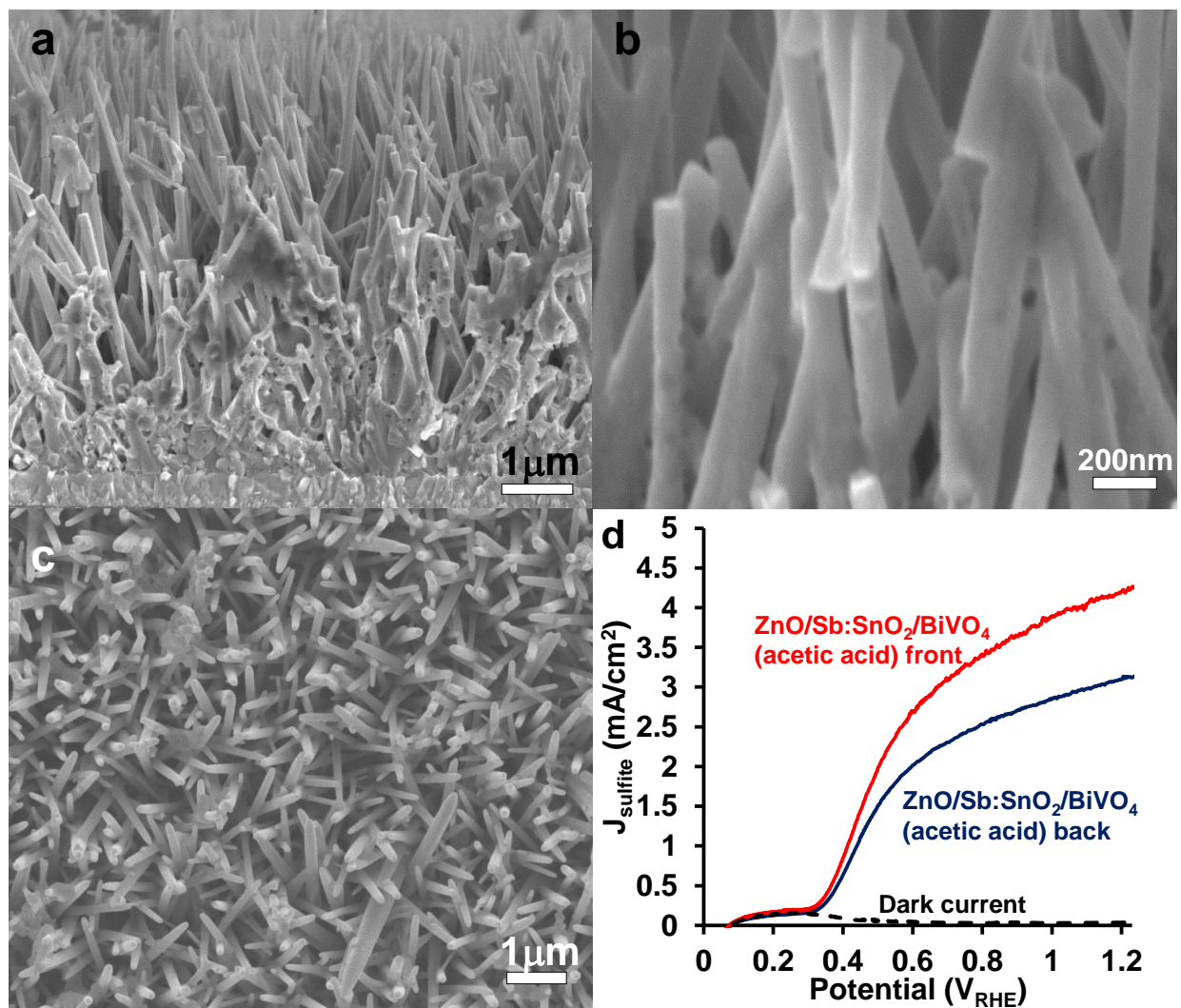
Figure 26. a-c) SEM images and d) J-V curves of BiVO$_4$ deposited onto 12-hr-grown ZnO core/Sb:SnO$_2$ shell nanowires using an acetic acid + acetylacetone solvent without intentionally etching away the ZnO cores beforehand. Photocurrents are for sulfite oxidation (J$_{sulfite}$) measured under simulated AM 1.5 G illumination using a 3-electrode configuration in aqueous phosphate buffer (pH 7) with 1M Na$_2$SO$_3$.
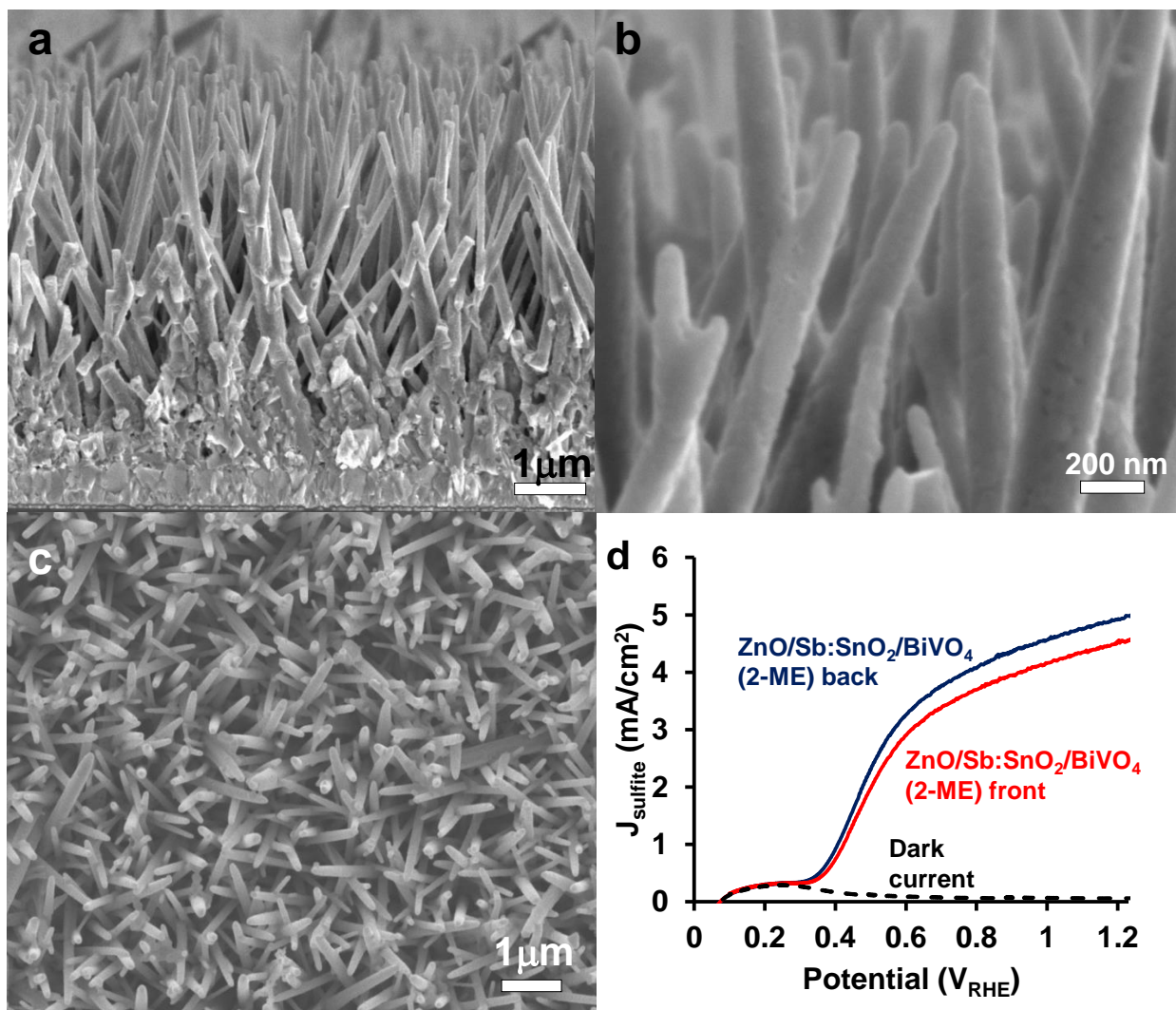
Figure 27. a-c) SEM images and d) J-V curves of BiVO$_4$ deposited onto 12-hr-grown ZnO core/Sb:SnO$_2$ shell nanowires using a 2-methoxy ethanol + acetylacetone solvent. Photocurrents are for sulfite oxidation (J$_{sulfite}$) measured under simulated AM 1.5 G illumination using a 3-electrode configuration in aqueous phosphate buffer (pH 7) with 1M Na$_2$SO$_3$.

2.6 Conclusions of Present Research on BiVO$_4$ Photoanodes

In conclusion, by changing the length and the packing density of nanotubes, these new Sb:SnO$_2$/BiVO$_4$ nanotubes provide higher charge separation efficiency under both front and back-side illumination. The new Sb:SnO$_2$/BiVO$_4$ nanotube photoanodes achieve $\eta_{abs} \times \eta_{sep}$ of ~ 58.5% under back illumination and ~ 57.3% under front illumination at 0.6 V$_{RHE}$ for simulated AM 1.5G sunlight, which are the highest reported values for BiVO$_4$-based photoanodes to date.

The Sb:SnO$_2$ nanotubes are promising electron collectors, and can possibly be widely used to improve the PEC performance of other semiconductors which have similar charge transport limitations as BiVO$_4$.

Reference

[1]   Park, Y.; McDonald, K. J.; Choi, K.-S. *Chemical Society Reviews* **2013,** 42, (6), 2321-2337.

[2]   Abdi, F. F.; Firet, N.; van de Krol, R. *ChemCatChem* **2013,** 5, (2), 490-496.

[3]   Chemelewski, W. D.; Lee, H.-C.; Lin, J.-F.; Bard, A. J.; Mullins, C. B. *Journal of the American Chemical Society* **2014,** 136, (7), 2843-2850.

[4]   Tamirat, A. G.; Su, W.-N.; Dubale, A. A.; Chen, H.-M.; Hwang, B.-J. *Journal of Materials Chemistry A* **2015,** 3, (11), 5949-5961.

[5]   Kim, T. W.; Ping, Y.; Galli, G. A.; Choi, K.-S. *Nature Communications* **2015,** 6, 8769.

[6]   Kim, T. W.; Choi, K.-S. *Science* **2014,** 343, (6174), 990-994.

[7]   Luo, W.; Yang, Z.; Li, Z.; Zhang, J.; Liu, J.; Zhao, Z.; Wang, Z.; Yan, S.; Yu, T.; Zou, Z. *Energy & Environmental Science* **2011,** 4, (10), 4046-4051.

[8]   Liang, Y.; Tsubota, T.; Mooij, L. P. A.; van de Krol, R. *The Journal of Physical Chemistry C* **2011,** 115, (35), 17594-17598.

[9]   Zhong, D. K.; Choi, S.; Gamelin, D. R. *Journal of the American Chemical Society* **2011,** 133, (45), 18370-18377.

[10]   Parmar, K. P. S.; Kang, H. J.; Bist, A.; Dua, P.; Jang, J. S.; Lee, J. S. *ChemSusChem* **2012,** 5, (10), 1926-1934.

[11]   Zhang, K.; Shi, X.-J.; Kim, J. K.; Park, J. H. *Physical Chemistry Chemical Physics* **2012,** 14, (31), 11119-11124.

[12]   Jeong, H. W.; Jeon, T. H.; Jang, J. S.; Choi, W.; Park, H. *The Journal of Physical Chemistry C* **2013,** 117, (18), 9104-9112.

[13]   Abdi, F. F.; Han, L.; Smets, A. H. M.; Zeman, M.; Dam, B.; van de Krol, R. *Nat Commun* **2013,** 4.

［14］ Seabold, J. A.; Zhu, K.; Neale, N. R. *Physical Chemistry Chemical Physics* **2014,** 16, (3), 1121-1131.

［15］ Park, H. S.; Kweon, K. E.; Ye, H.; Paek, E.; Hwang, G. S.; Bard, A. J. *The Journal of Physical Chemistry C* **2011,** 115, (36), 17870-17879.

［16］ Berglund, S. P.; Rettie, A. J. E.; Hoang, S.; Mullins, C. B. *Physical Chemistry Chemical Physics* **2012,** 14, (19), 7065-7075.

［17］ Abdi, F. F.; Savenije, T. J.; May, M. M.; Dam, B.; van de Krol, R. *Journal of Physical Chemistry Letters* **2013,** 4, (16), 2752-2757.

［18］ Zhou, M.; Wu, H. B.; Bao, J.; Liang, L.; Lou, X. W.; Xie, Y. *Angewandte Chemie, International Edition* **2013,** 52, (33), 8579-8583.

［19］ Jo, W. J.; Jang, J.-W.; Kong, K.-j.; Kang, H. J.; Kim, J. Y.; Jun, H.; Parmar, K. P. S.; Lee, J. S. *Angewandte Chemie International Edition* **2012,** 51, (13), 3147-3151.

［20］ Wang, G.; Ling, Y.; Lu, X.; Qian, F.; Tong, Y.; Zhang, J. Z.; Lordi, V.; Rocha Leao, C.; Li, Y. *The Journal of Physical Chemistry C* **2013,** 117, (21), 10957-10964.

［21］ Kim, T. W.; Ping, Y.; Galli, G. A.; Choi, K.-S. *Nat Commun* **2015,** 6.

［22］ Chatchai, P.; Murakami, Y.; Kishioka, S. Y.; Nosaka, A. Y.; Nosaka, Y. *Electrochimica Acta* **2009,** 54, (3), 1147-1152.

［23］ Hong, S. J.; Lee, S.; Jang, J. S.; Lee, J. S. *Energy & Environmental Science* **2011,** 4, (5), 1781-1787.

［24］ Shi, X.; Zhang, K.; Shin, K.; Ma, M.; Kwon, J.; Choi, I. T.; Kim, J. K.; Kim, H. K.; Wang, D. H.; Park, J. H. *Nano Energy* **2015,** 13, 182-191.

［25］ Moniz, S. J. A.; Zhu, J.; Tang, J. *Advanced Energy Materials* **2014,** 4, (10), n/a-n/a.

［26］ Zhang, L.; Reisner, E.; Baumberg, J. J. *Energy & Environmental Science* **2014,** 7, (4), 1402-1408.

［27］   Rao, P. M.; Cai, L.; Liu, C.; Cho, I. S.; Lee, C. H.; Weisse, J. M.; Yang, P.; Zheng, X. *Nano Letters* **2014,** 14, (2), 1099-1105.

［28］   Su, J.; Guo, L.; Bao, N.; Grimes, C. A. *Nano Letters* **2011,** 11, (5), 1928-1933.

［29］   Pilli, S. K.; Janarthanan, R.; Deutsch, T. G.; Furtak, T. E.; Brown, L. D.; Turner, J. A.; Herring, A. M. *Physical Chemistry Chemical Physics* **2013,** 15, (35), 14723-14728.

［30］   Pihosh, Y.; Turkevych, I.; Mawatari, K.; Uemura, J.; Kazoe, Y.; Kosar, S.; Makita, K.; Sugaya, T.; Matsui, T.; Fujita, D.; Tosa, M.; Kondo, M.; Kitamori, T. *Scientific Reports* **2015,** 5, 11141.

［31］   Sun, Y.; Chemelewski, W. D.; Berglund, S. P.; Li, C.; He, H.; Shi, G.; Mullins, C. B. *ACS Applied Materials & Interfaces* **2014,** 6, (8), 5494-5499.

［32］   Shi, X.; Choi, I. Y.; Zhang, K.; Kwon, J.; Kim, D. Y.; Lee, J. K.; Oh, S. H.; Kim, J. K.; Park, J. H. *Nature Communications* **2014,** 5, 4775.

［33］   Abdi, F. F.; Han, L.; Smets, A. H. M.; Zeman, M.; Dam, B.; van de Krol, R. *Nature Communications* **2013,** 4, 2195.

［34］   Zhou, L.; Zhao, C.; Giri, B.; Allen, P.; Xu, X.; Joshi, H.; Fan, Y.; Titova, L. V.; Rao, P. M. *Nano Letters* **2016,** 16, (6), 3463-3474.

［35］   Liang, Y.; Tsubota, T.; Mooij, L. P. A.; van de Krol, R. *J. Phys. Chem. C* **2011,** 115, (35), 17594-17598.

［36］   Jing, D.; Guo, L.; Zhao, L.; Zhang, X.; Liu, H.; Li, M.; Shen, S.; Liu, G.; Hu, X.; Zhang, X.; Zhang, K.; Ma, L.; Guo, P. *International Journal of Hydrogen Energy* **2010,** 35, (13), 7087-7097.

［37］   Chemseddine, A.; Ullrich, K.; Mete, T.; Abdi, F. F.; van de Krol, R. *Journal of Materials Chemistry A* **2016,** 4, (5), 1723-1728.

［38］   Kuang, Y.; Jia, Q.; Nishiyama, H.; Yamada, T.; Kudo, A.; Domen, K. *Adv. Energy Mater.* **2016,** 6, (2), 1501645.

[39]   LaForge, J. M.; Cocker, T. L.; Beaudry, A. L.; Cui, K.; Tucker, R. T.; Taschuk, M. T.; Hegmann, F. A.; Brett, M. J. *Nanotechnology* **2014,** 25, (3), 035701.

[40]   Chen, J.-Z.; Ahn, H.; Yen, S.-C.; Tsai, Y.-J. *ACS Applied Materials & Interfaces* **2014,** 6, (23), 20994-20999.

[41]   Hannah, J. J.; Callum, J. D.; Qiang, G.; Tan, H. H.; Chennupati, J.; James, L.-H.; Laura, M. H.; Michael, B. J. *Nanotechnology* **2013,** 24, (21), 214006.

[42]   Xingquan, Z.; Jingshan, L.; Dongwook, L.; Chuanwei, C.; Daniel, S.; Saritha, K. N.; Siew Ann, C.; Hong Jin, F.; Elbert, E. M. C. *Journal of Physics D: Applied Physics* **2012,** 45, (46), 465101.

[43]   Strait, J. H.; George, P. A.; Levendorf, M.; Blood-Forsythe, M.; Rana, F.; Park, J. *Nano Letters* **2009,** 9, (8), 2967-2972.

[44]   Baxter, J. B.; Schmuttenmaer, C. A. *Journal of Physical Chemistry B* **2006,** 110, (50), 25229-25239.

[45]   Yang, C.-S.; Chang, C.-H.; Lin, M.-H.; Yu, P.; Wada, O.; Pan, C.-L. *Optics Express* **2012,** 20, (S4), A441-A451.

[46]   Titova, L. V.; Cocker, T. L.; Cooke, D. G.; Wang, X.; Meldrum, A.; Hegmann, F. A. *Physical Review B* **2011,** 83, (8), 085403.

[47]   Button, K. J.; Fonstad, C. G.; Dreybrodt, W. *Physical Review B* **1971,** 4, (12), 4539-4542.

[48]   White, M. E.; Bierwagen, O.; Tsai, M. Y.; Speck, J. S. *Journal of Applied Physics* **2009,** 106, (9), 093704.

[49]   Cocker, T. L.; Titova, L. V.; Fourmaux, S.; Holloway, G.; Bandulet, H. C.; Brassard, D.; Kieffer, J. C.; El Khakani, M. A.; Hegmann, F. A. *Physical Review B* **2012,** 85, (15), 155120.

[50]   Cocker, T. L.; Titova, L. V.; Fourmaux, S.; Bandulet, H.-C.; Brassard, D.; Kieffer, J.-C.; El Khakani, M. A.; Hegmann, F. A. *Applied Physics Letters* **2010,** 97, (22), 221905.

[51]   Beard, M. C.; Turner, G. M.; Schmuttenmaer, C. A. *Journal of Physical Chemistry B* **2002,** 106, (29), 7146-7159.

［52］　Baxter, J. B.; Guglietta, G. W. *Analytical Chemistry* **2011,** 83, (12), 4342-4368.

［53］　Law, M.; Greene, L. E.; Johnson, J. C.; Saykally, R.; Yang, P. *Nat Mater* **2005,** 4, (6), 455-459.

［54］　Greene, L. E.; Law, M.; Tan, D. H.; Montano, M.; Goldberger, J.; Somorjai, G.; Yang, P. *Nano Letters* **2005,** 5, (7), 1231-1236.

［55］　Lee, Y.-J.; Ruby, D. S.; Peters, D. W.; McKenzie, B. B.; Hsu, J. W. P. *Nano Letters* **2008,** 8, (5), 1501-1505.

［56］　Kim, J. H.; Jo, Y.; Kim, J. H.; Jang, J. W.; Kang, H. J.; Lee, Y. H.; Kim, D. S.; Jun, Y.; Lee, J. S. *ACS Nano* **2015,** 9, (12), 11820-11829.

Chapter 3 BiVO$_4$ for Photovoltaics (PV)

3.1 Literature Review of Metal Oxides as Light Absorber for PV

As we mentioned in the last chapter, BiVO$_4$ is a very promising metal oxide light absorber, and shows decent performance in PEC cell. Today, most of the researches on BiVO$_4$ are focusing on improving its PEC performance, no one has reported any results for BiVO$_4$ PV cell.[1-5] The materials cost of bismuth metal and vanadium metal in BiVO$_4$ PV cells are \$ 29/kg and \$ 14/kg, respectively, which are much lower than the materials cost of tellurium metal (\$ 240/kg) in CdTe PV cells, gallium metal (\$ 525/kg) in GaAs PV cells, and indium metal (\$ 1000/kg) in CIGS PV cells.[6] The manufacturing temperature of BiVO$_4$ in BiVO$_4$ PV cell is 550 °C, which is much lower than the manufacturing temperature of Si (2200 °C) in crystalline Si PV cell. Theoretically, BiVO$_4$ PV cells have lower cost compared to most of the current commercialized PV cells. It will be interesting to see what solar conversion efficiency can be achieved by a BiVO$_4$ PV cell.

3.2 Objective of Present BiVO$_4$ PV Cells Research

The objective of present BiVO$_4$ PV Cells research is to obtain efficient BiVO$_4$ PV cells. This objective can be realized by following approach: (1), develop deposition techniques to conformably deposit hole transport layer and Au electrode onto BiVO$_4$ to obtain BiVO$_4$ PV cells. (2), add nanostructured Sb:SnO$_2$ scaffolds to BiVO$_4$ PV cells to improve solar conversion efficiency. (3), construct liquid junction BiVO$_4$ PV cells with nonaqueous electrolyte.

3.3 Experimental Methods of BiVO4 PV Cells

3.3.1 Synthesis of FTO/SnO$_2$/Sb:SnO$_2$ Nanorod/BiVO$_4$/V$_2$O$_5$/Au PV Cells

The FTO/Sb:SnO$_2$ nanorod/SnO$_2$/BiVO$_4$/V$_2$O$_5$/Au PV cells were synthesized by a combination of spin-coating of SnO$_2$, hydrothermal synthesis of Sb:SnO$_2$ NRAs onto FTO substrates, drop-casting of BiVO$_4$ onto the NRAs, sputtering V$_2$O$_5$, and thermal evaporating Au.

The FTO substrates were firstly spin coated (2000 rpm for 30 s) with SnO_2 precursor solution which was composed of 0.25 M $SnCl_2$, dissolved in 10 mL 2-methoxyethanol (99%, Alfa Aesar). The synthesis methods of hydrothermal synthesis of $Sb:SnO_2$ NRAs onto FTO substrates and drop-casting of $BiVO_4$ onto the NRAs are same as the synthesis methods of $Sb:SnO_2/BiVO_4$ NRA photoanodes in chapter 2. After drop-casting $BiVO_4$ onto the nanorods, the substrates were coated with 10 nm thick V_2O_5 by magnetron sputtering using a RF gun (AJA, sputtering system - 3 target). Then the substrates were deposited with Au electrode by thermal evaporation to obtain FTO/Sb:SnO_2 nanotube/$BiVO_4$/V_2O_5/Au PV Cells.

3.3.2 Synthesis of FTO/SnO$_2$/Sb:SnO$_2$ Nanotube/BiVO$_4$/V$_2$O$_5$/Au Nanotubes PV Cells

The FTO/SnO$_2$/Sb:SnO$_2$ nanotube /BiVO$_4$/V$_2$O$_5$/Au PV cells were synthesized by a combination of hydrothermal synthesis of ZnO nanowires onto FTO substrates, drop-casting of Sb:SnO$_2$ onto the ZnO nanowires, etching and washing out ZnO nanowires, drop-casting of BiVO$_4$ onto the nanotubes, sputtering V$_2$O$_5$, and thermal evaporating Au. The synthesis methods of hydrothermal synthesis of ZnO nanowires onto FTO substrates, drop-casting of Sb:SnO$_2$ onto the ZnO nanowires, etching and washing out ZnO nanowires and drop-casting of BiVO$_4$ onto the nanotubes are same as the synthesis methods of Sb:SnO$_2$/BiVO$_4$ nanotube photoanodes in chapter 2. After drop-casting BiVO$_4$ onto the nanotubes, the substrates were coated with 10 nm thick V$_2$O$_5$ by magnetron sputtering using a RF gun (AJA, sputtering system - 3 target). Then the substrates were deposited with Au electrode by thermal evaporation to obtain FTO/Sb:SnO$_2$ nanotube/BiVO$_4$/V$_2$O$_5$/Au PV Cells.

3.3.3 Synthesis of FTO/Sb:SnO$_2$ Nanotube /BiVO$_4$ Liquid Junction PV Cells

Each FTO/Sb:SnO$_2$ Nanotube /BiVO$_4$ liquid junction PV Cell was constructed in a sandwich structure with a shell FTO/Sb:SnO$_2$ Nanotube /BiVO$_4$ electrode, core nonaqueous electrolyte and a shell Pt/FTO electrode. The shell FTO/Sb:SnO$_2$ Nanotube /BiVO$_4$ electrode was synthesized using same methods as the synthesis methods of Sb:SnO$_2$/BiVO$_4$ nanotube photoanodes in chapter 2. The core nonaqueous electrolyte was composed of 1.5 M 1-butyl-3-methylimidazolium bromide (BMIBr), 50 mM LiBr, 20 mM Br$_2$ and 0.5 M tert-butyl pyridine,

dissolved in 2 mL acetonitrile. The shell Pt/FTO electrode was synthesized by firstly, dissolving 100 mM chloroplatinic acid hexahydrate into IPA to obtain Pt precursor solution. Then, the Pt precursor solution was 1-time spin coated onto FTO substrate at 2000 rpm for 30 s. Finally, the substrate was annealed in air at 350 °C for 30 min to obtain Pt/FTO electrode.

3.4 Results and Discussions of BiVO$_4$ PV Cells

The main challenge of making efficient BiVO$_4$ PV cells is the 1D core/shell nanostructure, which simultaneously improve light absorption efficiency and charge separation efficiency in BiVO$_4$ PEC cells, produces non-uniform coating and short circuit problems in BiVO$_4$ PV cells, due to the random orientated nanorods/nanotubes, which block coating, and the imperfect nanorod/nanotube scaffolds, which produce exposed FTO electrode. The problems were solved by coating a layer of SnO$_2$ to fully cover the FTO, decreasing hydrothermal growth time to obtain shorter nanorods, and drop casting just enough amount of BiVO$_4$ to fill the nanorods. After synthesis, the morphologies of the FTO/SnO$_2$/Sb:SnO$_2$ nanorod/BiVO$_4$/V$_2$O$_5$/Au PV cells were characterized by scanning electron microscopy (SEM, JEOL 7000F, 5 kV). Figure 1a and 1b shows SEM top image and cross-section image of FTO/SnO2/Sb:SnO$_2$ nanorod/BiVO$_4$/V$_2$O$_5$/Au PV cell, respectively. A planar BiVO$_4$ PV cell with same amount of BiVO$_4$ is used to compare with our nanostructured BiVO$_4$ PV cell, and the SEM top image and cross-section images are shown in Figure 1c and 1d, respectively. According to the Figure 1a and 1b, the FTO is fully covered by the spin coated SnO$_2$. The Sb:SnO$_2$ nanorods are about 300 nm long and were fully filled with drop casted BiVO$_4$, which forms a relatively flat surface on the top of the cell. This flat surface leads to more uniform coating of the hole transport layer of V$_2$O$_5$ and the Au electrode. Figure 1e. shows a SEM cross-section image of a FTO/SnO$_2$/Sb:SnO$_2$ Nanotube/BiVO$_4$/V$_2$O$_5$/Au cell which has long Sb:SnO$_2$ nanotube scaffolds. Because the deposition of V$_2$O$_5$ sputtering and Au thermal evaporation are both from vertical direction. The long and random oriented nanotubes block the area underneath, which leads to non-uniform coating of the hole transport layer of V$_2$O$_5$ and the Au electrode onto long Sb:SnO$_2$ nanotubes/BiVO$_4$. These discontinuous layers of V$_2$O$_5$ and Au electrode prevent the holes transport, which makes the cell has almost zero performance.
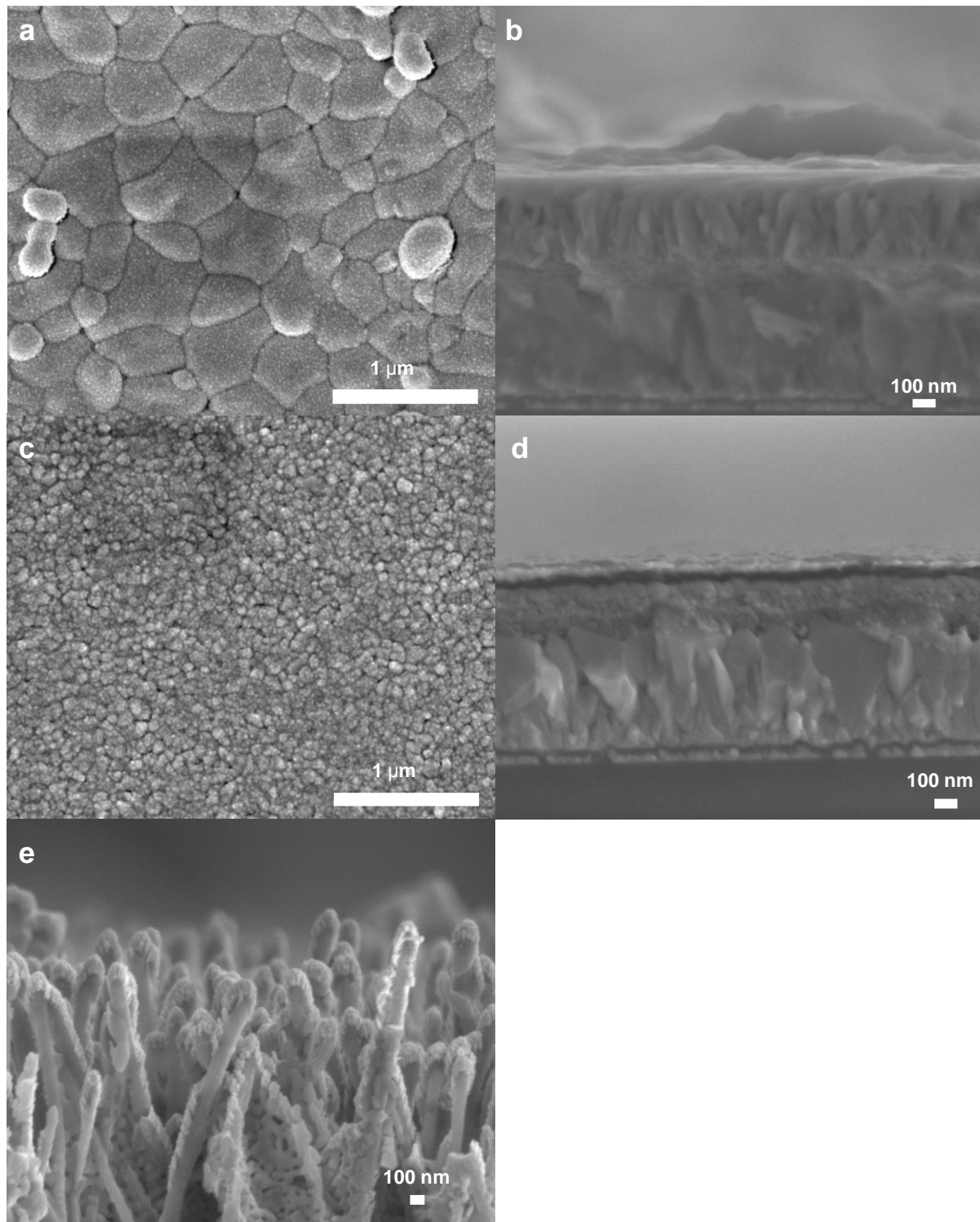
Figure 1. Scanning electron microscopy (SEM) of a) top and b) cross-section of FTO/SnO$_2$/Sb:SnO$_2$ nanorod/BiVO$_4$/V$_2$O$_5$/Au PV cell, c) top and d) cross-section of planar BiVO$_4$ PV cell, e) cross-section of non-uniform coating of the hole transport layer of V$_2$O$_5$ and the Au electrode onto long Sb:SnO$_2$ nanotubes/BiVO$_4$.

The performance of the FTO/SnO$_2$/Sb:SnO$_2$ nanorod/BiVO$_4$/V$_2$O$_5$/Au PV cell and the planar BiVO$_4$ PV cell were evaluated by measuring the current density-voltage (J-V) curve (i.e. linear sweep voltammogram) under AM 1.5 G sunlight using a potentiostat (Model SP-200, BioLogic). Each cell has working area of about 0.2 cm^2, and the J-V curve was measured at a scan rate of 10mV/s. The J-V curve of the FTO/SnO$_2$/Sb:SnO$_2$ nanorod/BiVO$_4$/V$_2$O$_5$/Au PV cell and the planar BiVO$_4$ PV cell are show in Figure 2a and 2b, respectively. These two cells have similar open circuit voltage of ~ 0.15 V, however, the nanostructured BiVO$_4$ PV cell generates much higher current than the planar BiVO$_4$ PV cell. The solar conversion efficiency of the FTO/SnO$_2$/Sb:SnO$_2$ nanorod/BiVO$_4$/V$_2$O$_5$/Au PV cell and the planar BiVO$_4$ PV cell are 0.08% and 0.01% respectively, which indicates that the core/shell nanostructure can significantly improve the solar conversion efficiency of BiVO$_4$ PV cell. However, even with the core/shell nanostructure, the solar conversion efficiency of the BiVO$_4$ PV cell is still very low compared to the theoretical maximum efficiency of 18%. One of the main reasons for the low efficiency is the charge separation in BiVO$_4$ PV cell is very low. That is because obtaining a flat surface for uniform V$_2$O$_5$ and Au electrode coating requires a thick layer of BiVO$_4$ coating. Even though the core/shell nanostructure can help and improve charge separation in BiVO$_4$ cells, the thickness of BiVO$_4$ layer is still too thick to have efficient charge separation.
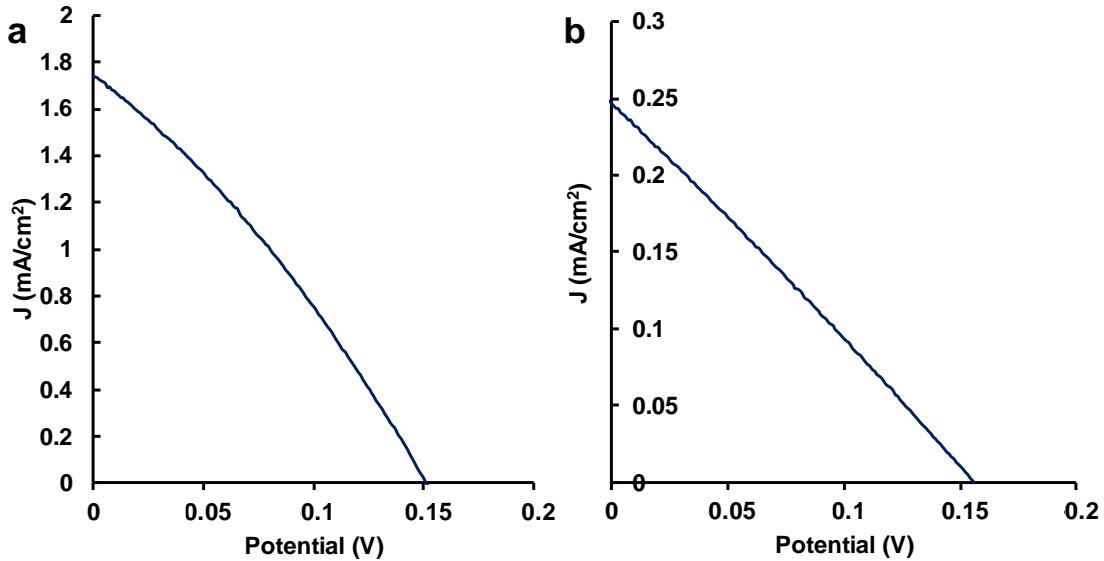
Figure 2. Current density-voltage (J-V) curve of a) FTO/SnO$_2$/Sb:SnO$_2$ nanorod/BiVO$_4$/V$_2$O$_5$/Au PV cell b) planar BiVO$_4$ PV cell.

A liquid junction BiVO4 PV cell was made to improve the charge separation efficiency in BiVO4 PV cell. The liquid junction BiVO4 PV cell was composed of a FTO/Sb:SnO2 nanotube /BiVO4 electrode, Br$^-$/Br^{3-} redox couple nonaqueous electrolyte and a Pt/FTO electrode. Because in liquid junction PV cell, the electrolyte can connect two electrodes, consume charge carriers and conduct electricity, the BiVO4 does not need to have flat surface for uniform coating. Therefore, long Sb:SnO2 nanotube scaffolds with thin BiVO4 coating were used in liquid junction PV cell, which can significantly improve charge separation efficiency in BiVO4 compared to short Sb:SnO2 nanorods with thick layer of BiVO4 coating. The performance of the FTO/Sb:SnO2 Nanotube /BiVO4 liquid junction PV Cell was evaluated by measuring the current density-voltage (J-V) curve (i.e. linear sweep voltammogram) under AM 1.5 G sunlight using a potentiostat (Model SP-200, BioLogic). Each cell has working area of about 0.1 cm^2, and the J-V curve was measured at a scan rate of 10mV/s. The J-V curve of the FTO/Sb:SnO2 Nanotube /BiVO4 liquid junction PV Cell is show in Figure 3. The FTO/Sb:SnO2 Nanotube /BiVO4 liquid junction PV Cell has significant improvement on both open circuit voltage and short circuit current compared to solid state BiVO4 PV cells. The solar conversion efficiency is 1.22 %.
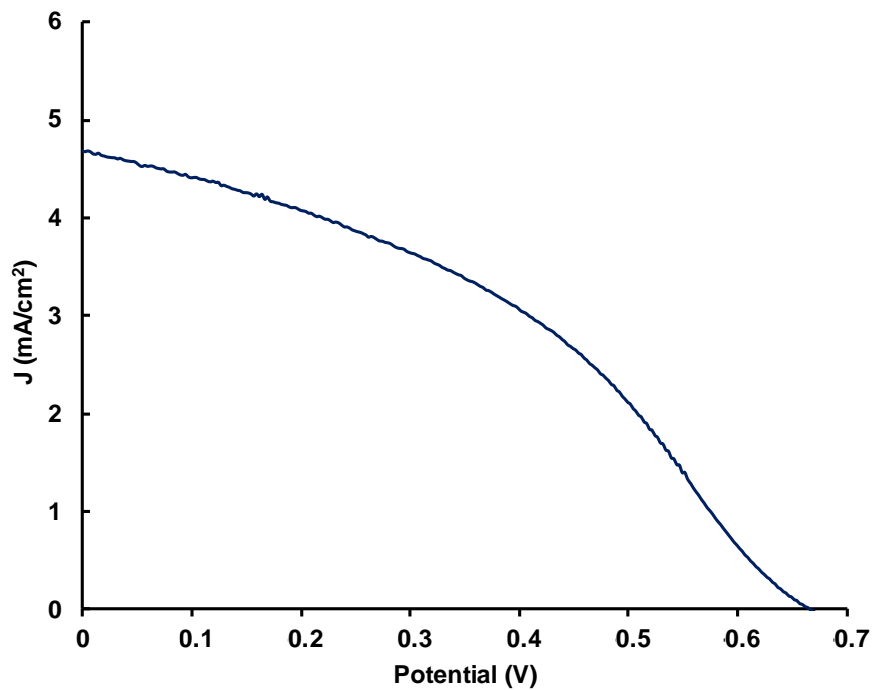
Figure 3. Current density-voltage (J-V) curve of FTO/Sb:SnO2 Nanotube /BiVO4 liquid junction PV Cell.

3.5 Conclusions of BiVO₄ PV Cells

In conclusion, $BiVO_4$ PV cells have been successfully synthesized and the performance of $BiVO_4$ PV cells have been investigated. The modified core/shell nanostructure with short $Sb:SnO_2$ nanorods and thick layer of $BiVO_4$ coating forms a flat surface for uniform coating of hole transport layer V_2O_5 and Au electrode, which can significantly improve the solar conversion efficiency of $BiVO_4$ PV cell. The solar conversion efficiency of $BiVO_4$ PV cell was further improved by constructing a liquid junction $BiVO_4$ PV cell which was composed of a FTO/$Sb:SnO_2$ nanotube /$BiVO_4$ electrode, Br^-/Br^{3-} redox couple nonaqueous electrolyte and a Pt/FTO electrode. The FTO/$Sb:SnO_2$ Nanotube /$BiVO_4$ liquid junction PV Cell achieved 1.22 % of solar conversion efficiency, which is the highest reported values for $BiVO_4$-based PV cells to date. However, this 1.22 % efficiency still much lower the theoretical maximum efficiency of ~18 %. That is because the redox potential of Br^-/Br^{3-} redox couple does not have good match with $BiVO_4$ band position so that limits the open circuit voltage in liquid junction $BiVO_4$ PV cells.

Reference

［1］　　Lee, D. K.; Choi, K.-S. *Nature Energy* **2018,** 3, (1), 53-60.

［2］　　Yao, X.; Wang, D.; Zhao, X.; Ma, S.; Bassi, P. S.; Yang, G.; Chen, W.; Chen, Z.; Sritharan, T. *Energy Technology* **2018,** 6, (1), 100-109.

［3］　　Wang, S.; Chen, P.; Bai, Y.; Yun, J.-H.; Liu, G.; Wang, L. *Advanced Materials* **2018,** 30, (20), 1800486.

［4］　　Kalanoor, B. S.; Seo, H.; Kalanur, S. S. *Materials Science for Energy Technologies* **2018,** 1, (1), 49-62.

［5］　　Zhang, H.; Yu, Y.; Zhang, L.; Dong, S. *Angewandte Chemie International Edition* **2018,** 57, (6), 1547-1551.

［6］　　Prices of Elements and Their Compounds. https://en.wikipedia.org/wiki/Prices_of_elements_and_their_compounds

Chapter 4 New Metal Oxide CuBiW$_2$O$_8$ (CBTO) as Light Absorber

4.1 Literature Review of CBTO as Light Absorber

Apart from BiVO$_4$, other ternary metal oxides were also found to be promising for light absorber. Another typical ns^2-md^0 ternary metal oxide, Bi$_2$WO$_6$ with 2.8 eV[1] band gap, showed some potential in photocatalytic applications.[2, 3] Recently, a promising ternary metal oxide light absorber CuBi$_2$O$_4$ was investigated. The CuBi$_2$O$_4$ is a p-type semiconductor with band gap of ~ 1.8 eV, carrier mobility of 1.2×10^{-3} cm^{2}V^{-1}s^{-1}, carrier life time of ~ 800 ns and carrier diffusion length of 52 nm.[4] It has been investigated as a photocathode for photoelectrochemical water splitting, and many efforts have been made to improve the charge separation efficiency in CuBi$_2$O$_4$.[5-7] However, even though the band gaps of these ternary metal oxides are smaller than those of typical binary metal oxides, they are still much larger than the 1.0 – 1.6 eV range that is needed to achieve high solar energy conversion efficiency according to the Shockley-Queisser limit. Therefore, if metal oxide light absorbers are to challenge silicon in solar cell market, discovering new metal oxide light absorber materials with smaller band gaps and better electrical properties is necessary.

Meanwhile, a quaternary metal oxide CuBiW$_2$O$_8$ (CBTO) has been predicted as a promising semiconductor with strong optical absorption and an indirect band gap of 1.49 eV.[8] The bottom of the conduction band in CBTO is dominated by Bi 6p and W 5d orbitals, which is similar to the conduction band of Bi-W based oxides.[8, 9] On the other hand, the band gap of CBTO is significantly reduced compared to BiW$_2$O$_6$ due to the presence of the Cu 3d orbital (~ -5.9 eV vs vacuum), which raises the energy of the top of the valence band compared to that of Bi$_2$WO$_6$ (~ -6.8 eV vs vacuum[10], formed by hybridization of Bi 6s and the O 2p orbitals). Out of the promising multinary metal oxide light absorbers BiVO$_4$, CuBi$_2$O$_4$, and CBTO, CBTO has the smallest band gap with the best match to solar spectrum for high PV efficiency. Until now, no CBTO-based devices have been reported as CBTO synthesis presents many challenges such as maintaining Cu in Cu^{1+} rather than in Cu^{2+} oxidation state, suppressing the loss of volatile Cu and contamination by the interdiffusion between substrates and CBTO at high growth

temperatures.[11] The only report of CBTO synthesis over two decades ago didn't provide details on fabrication or optical, electrical or photoelectrical characterization.[12]

4.2 Objective of Present CBTO Light Absorbers Research

The objective of present CBTO light absorbers research is to fabricate and characterize CBTO. This objective can be realized by the following approach: (1), use a solid state synthesis method to prevent interdiffusion of CBTO and regular TCO substrates. (2), synthesize CBTO in a Cu-rich condition to suppress the loss of volatile Cu. (3), purify CBTO by modifying the CBTO synthesis process. (4), characterize crystallinity, morphology and optoelectronic properties of CBTO by X-ray diffraction, SEM, UV-VIS absorbance, time-resolved photoluminescence spectroscopy, optical pump-terahertz (THz) probe spectroscopy, Hall Effect measurement, X-ray photoelectron spectroscopy (XPS) and ultraviolet photoelectron spectroscopy (UPS).

4.3 Experimental Methods of CBTO Light Absorbers

In this research, we demonstrate a tailored Cu-rich solid state synthesis method that enables the successful synthesis of CBTO powders and thin films. Synthesis of CBTO powders was firstly attempted by a standard solid state synthesis method in argon atmosphere (99.995 %, Praxair). In this method, 0.466 g Bi_2O_3 (99.9%, Sigma Aldrich), 0.928 g WO_3 (99.9%, Sigma Aldrich) and 0.143 g Cu_2O (> 99.99%, Sigma Aldrich) were mixed and ground in a glass vial by ball milling (500 rpm) for 20 hours. The oxygen partial pressure of our Ar gas is 0.5 ppm (~ 0.0004 Torr), in order to maintain Cu in Cu^{1+} oxidation state as well as reduce the synthesis temperature, 600 °C was selected to be CBTO synthesis temperature. (Figure 1a. shows the phase diagram of copper–oxygen system) Therefore, the mixed powders were then placed in a ceramic boat, and reacted by annealing in a tube furnace at 600 °C for 9 hours under 500 sccm flow rate of argon. However, CBTO was not synthesized under this condition due to the high volatility and mobility of Cu, causing loss of Cu during the annealing process. The SEM-EDS result of the mixed powder after annealing (Figure 1b) indicates the miss of Cu element in the mixed powder. The solid state synthesis method was then modified by annealing mixed powders

84

in a Cu-rich argon atmosphere. In the modified method, the same quantities of mixed powders were placed in a copper box constructed from Cu sheets (99.9%. Alfa Aesar). Then, the copper box was sealed by thin copper foil (99.99%. Alfa Aesar) to ensure that the mixed powders were reacted in a nearly closed environment with Cu-rich atmosphere. The mixed powders in the sealed copper box were then annealed and reacted in a tube furnace at the same condition. CBTO powders were successfully synthesized by this modified solid state method because the sealed Cu box prevented Cu loss in the mixed powders. The as-synthesized CBTO powders were then purified by repeating the ball milling and Cu-rich argon atmosphere annealing processes 3 times to obtain high purity CBTO powders.
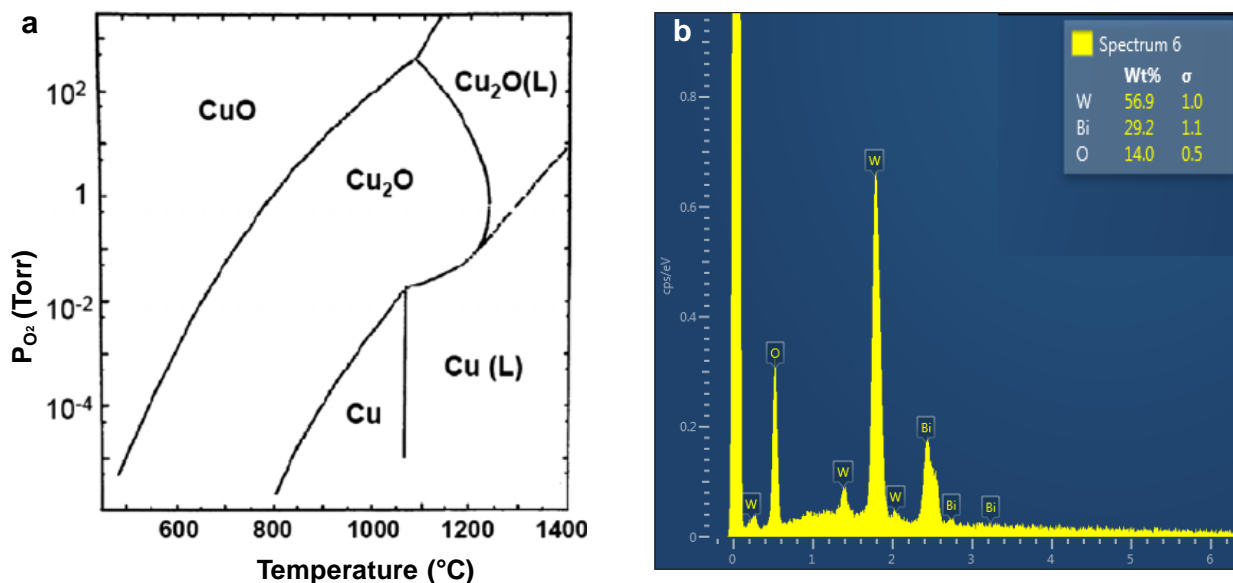
Figure 1. a) Phase diagram of copper–oxygen system. b) SEM-EDS result of the mixed powder after annealing without Cu box.

4.4 Results and Discussions of CBTO Light Absorbers

The purity and crystallinity of CBTO powders were characterized by X-ray diffraction (XRD, PANalytical Empyrean, Cu-kα, 45 kV, 40 mA). The XRD spectra of the mixed powders annealed without Cu-rich atmosphere, with Cu-rich atmosphere (as-synthesized CBTO), and after 1, 2, 3 times purification are shown in Figure 2. As we can see in Figure 2, the mixed

powders annealed without Cu-rich atmosphere are composed of WO_3, Bi_2O_3 and Bi_2WO_6. CBTO was not synthesized, and there was no Cu or Cu compound in the mixed powder, which indicates the loss of Cu element during the annealing process. In the powders synthesized by reaction in the Cu-rich atmosphere, however, CBTO was successfully synthesized. The major phase is triclinic CBTO and the only detectable impurity phase is orthorhombic Bi_2WO_6. The XRD peaks for orthorhombic Bi_2WO_6 became weaker and weaker after one time and two times purification, which indicates that the amount of Bi_2WO_6 in CBTO powders are significantly reduced by the purification. However, the XRD data of 3 times purified CBTO is almost identical to 2 times purified CBTO powders, which indicates that the presence of Bi_2WO_6 may be due to thermodynamic, rather than kinetic, limitations.
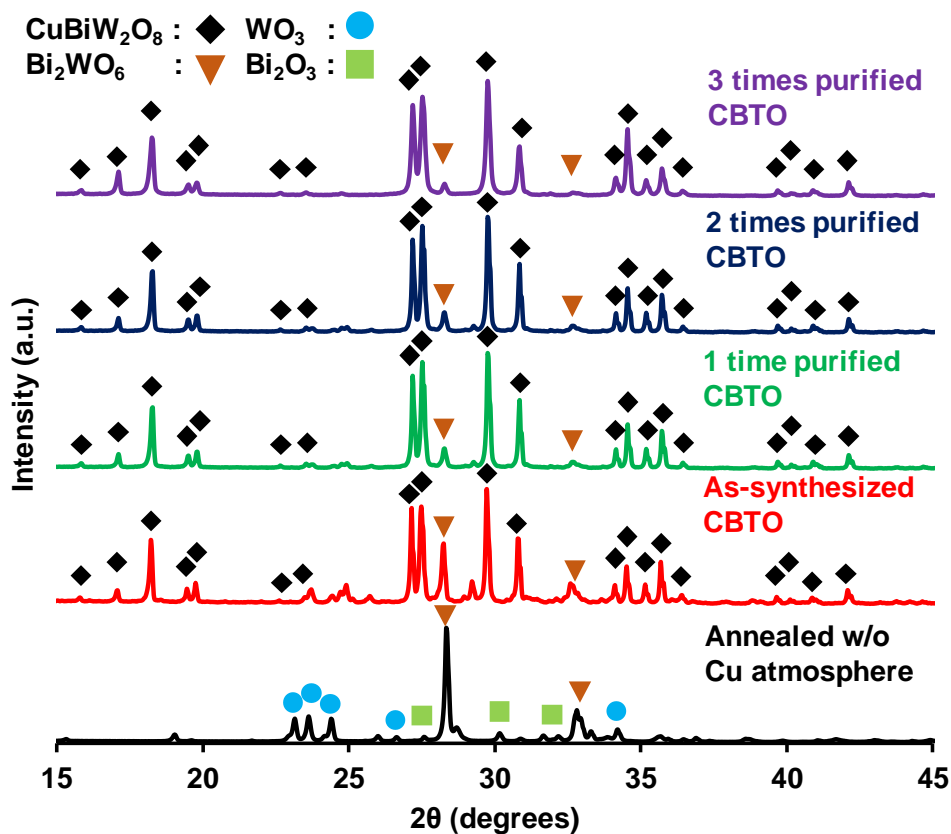
Figure 2. X-ray diffraction of mixed powder annealed without Cu-rich atmosphere (black), as-synthesized CBTO powders (red), CBTO powders after 1 time purification (green), after 2 times purification (blue), after 3 times purification (purple).

86

To test this, we conducted a study of the chemical potential landscape[13] of CBTO and its stable fragments within the framework of density functional theory (DFT).[14] This approach allows prediction of a single-phase region, if one exists, within thermodynamic stability limits of a compound. The region is obtained via the solution of the system of inequalities reflecting enthalpic conditions for the primary compound and any of its possible secondary phases,

$$\sum_\alpha n_\alpha \Delta\mu_\alpha = \Delta H_{f,p} \qquad (1a)$$

$$\sum_\alpha n_\beta \Delta\mu_\beta < \Delta H_{f,s} \qquad (1b)$$

as a function of chemical potentials of the constituent species of the primary phase.[15] In the above equations, $n_{\alpha,\beta}$ and $\Delta\mu_{\alpha,\beta}$ respectively represent the fraction of each species in the formula unit and its chemical potential bounded by

$$\Delta H_f \leq n_\alpha \Delta\mu_\alpha \leq 0 \qquad (2)$$

ΔH_f is the calculated formation enthalpy of the primary/secondary phase derived from E_{solid}, the total ground state energies of the compound, as

$$\Delta H_f = E_{solid} - \sum_\alpha n_\alpha E_\alpha^{bulk} \qquad (3)$$

where E_α^{bulk} is the ground state energy of α in its standard elemental phase. Tuning synthesis conditions to within the bounds of the single-phase region ensures the purity of the product by enthalpically eliminating the formation of its fragments. For CBTO, the process involves the following system of inequalities:

$$\mu_{Cu} + \mu_{Bi} + 2\mu_W + 4\mu_{O_2} = \Delta H_{f,CBTO} = -21.386 \ eV \qquad (4a)$$

$$\mu_{Cu} + \mu_{O_2} < \Delta_{f,CuO} = -1.590 \ eV \qquad (4b)$$

$$2\mu_{Cu} + \frac{1}{2}\mu_{O_2} < \Delta_{f,Cu_2O} = -1.602 \ eV \qquad (4c)$$

$$2\mu_{Bi} + \frac{3}{2}\mu_{O_2} < \Delta_{f,Bi_2O_3} = -6.242 \ eV \qquad (4d)$$

$$\mu_W + \frac{3}{2}\mu_{O_2} < \Delta_{f,WO_3} = -8.588 \ eV \qquad (4e)$$

$$\mu_{Cu} + \mu_W + 2\mu_{O_2} < \Delta_{f,CuWO_4} = -10.253 \ eV \qquad (4f)$$

$$2\mu_{Cu} + \mu_W + 2\mu_{O_2} < \Delta_{f,Cu_2WO_4} = -10.013 \ eV \qquad (4g)$$

$$2\mu_{Bi} + \mu_W + 3\mu_{O_2} < \Delta_{f,Bi_2WO_6} = -15.547 \; eV \qquad (4h)$$

$$2\mu_{Bi} + 2\mu_W + \frac{9}{2}\mu_{O_2} < \Delta_{f,Bi_2W_2O_9} = -24.166 \; eV \qquad (4i)$$

Ground state energy calculations were carried out in the Vienna *ab initio* Simulation package (VASP 5.4.4)[16, 17] utilizing the generalized gradient approximation as parameterized by Perdew-Burke-Ernzerhof (GGA-PBE)[18, 19] in treating the exchange and correlation potential of the Kohn-Sham solutions of DFT[20] Core electrons were treated within the frozen-core projector augmented-wave (PAW) framework[21, 22] while valence electrons were expanded in a plane wave basis set with a kinetic energy cutoff of 600 eV. Integrations in the Brillouin zone (BZ) were performed without symmetry considerations using the second order Methfessel-Paxton method[23] on a Monkhorst-Pack[24]k-point mesh of $5 \times 9 \times 11$ derived from lattice shape and size. Both energy cutoff and k-point mesh values were converged within a total energy of 1 meV. As was done in the original theoretical work on CBTO[8], a Hubbard-U[25-27] on-site Coulomb potential of U_{eff} = 6 eV was applied to Cu 3d to correct the underestimation of d-electron localization by DFT.[25, 28, 29]

The chemical potential landscape of CBTO is presented in Figure 3. CBTO, a quaternary metal oxide, would require a 3-dimentional landscape. Alternatively, as was done here, one can project the landscape onto several 2-dimentioanl planes by allowing for a given species' chemical potential to be varied manually. In Figure 3, extreme Cu-rich conditions were considered, i.e. μ_{Cu} = 0 eV, in preparing the landscape to better reflect the experimental setup mentioned above. The highlighted region represents one in which all phases but the two bismuth tungstate fragments of CBTO are thermodynamically unstable. The tungstate solutions take on the following form:

$$\mu_W \geq \frac{3}{2}\Delta H_{f,CBTO} - 2\Delta_{f,Bi_2WO_6} - \frac{3}{2}\mu_{Cu} + \frac{5}{2}\mu_{Bi} \qquad (5a)$$

$$\mu_W \geq \frac{9}{2}\Delta H_{f,CBTO} - 4\Delta_{f,Bi_2W_2O_9} - \frac{9}{2}\mu_{Cu} + \frac{7}{2}\mu_{Bi} \qquad (5b)$$

In this form, it is understood that regions below the tungstate bounds in Figure 3 represent thermodynamically stable conditions for the formation of either of the bismuth tungstates. Thus, they are deemed stable within the highlighted region of interest. Stability of the two phases persists throughout the possible range of Cu chemical potentials in which the region of interest is maintained. We provide similar analyses with respect to variations of Bi and W

chemical potentials, in which again the two tungstate phases persist throughout the respective regions of interest. This matches our experimental findings, in which even annealing the powders in a Cu-rich atmosphere did not completely prevent the formation of Bi_2WO_6. We conclude that the presence of bismuth tungstate in CBTO is a thermodynamic phenomenon.

Making further use of calculated formation enthalpies, a defect formation analysis[13, 30-32] was conducted to study intrinsic point defect formations in CBTO, including vacancies and anti-sites, at 0 K. Defect formation enthalpies are given by

$$\Delta H_\delta = E_\delta - E_p + \sum_\alpha m_\alpha \mu_\alpha \qquad (6a)$$

$$\mu_\alpha = \mu_\alpha^0 + \Delta\mu_\alpha \qquad (6b)$$

where E_δ and E_p are the total ground state energies of the primary compound with and without the defect, respectively. By convention, $m_\alpha = -1$ corresponds to the addition of one α atom to the system. μ_α^0 is a reference chemical potential from the standard elemental phase of α.
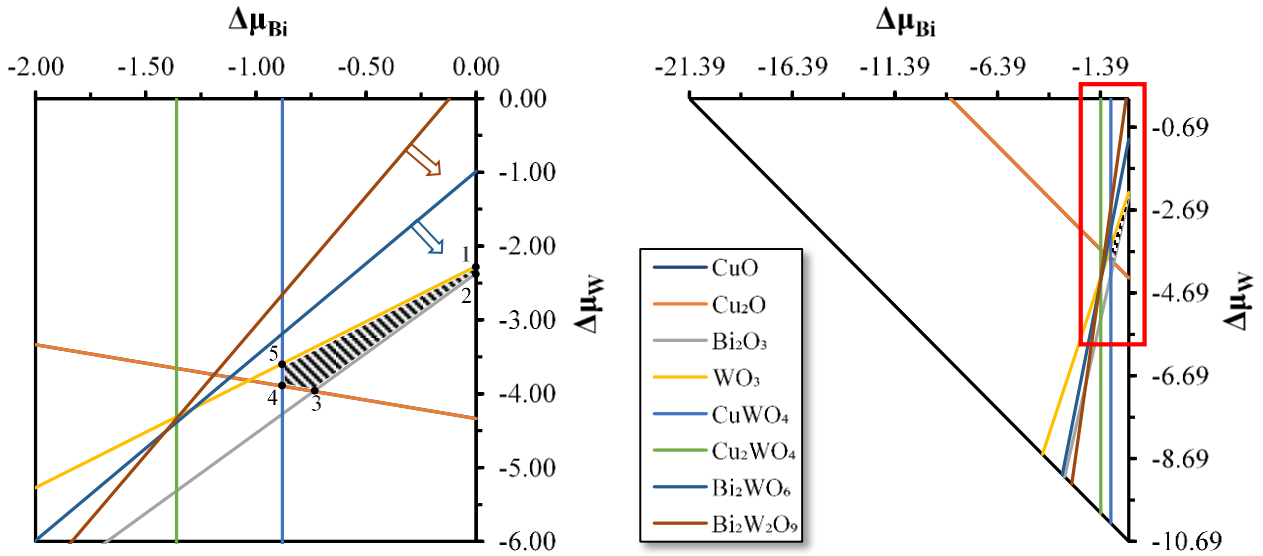
Figure 3. Chemical potential landscape for $CuBiW_2O_8$ (CBTO) as a function of constituent chemical potentials (zoomed at left). Triangular bounds represent the entire CBTO thermodynamic stability region. Cu chemical potential is set to zero reflecting extreme Cu-rich experimental conditions. The highlighted region corresponds to ideal synthesis conditions aiming at a pure, single-phase CBTO product. The bounding CBTO fragments Bi_2O_3, Cu_2O, and WO_3 reflect the synthesis route taken experimentally. Arrows represent the inequality solutions for the

two bismuth tungstate phases for which the fragments are thermodynamically stable and point towards the region of interest. The numbered corners reflect conditions used for defect formation calculations presented in Figure 4.

$\Delta\mu_\alpha$ determines the chemical environment by representing the additional energy required to get α from a source during synthesis, with $\Delta\mu_\alpha = 0$ reflecting α-rich conditions. $\Delta\mu_\alpha$ is bounded according to eq. 3. Conditions at the five corners of the region of interest (Figure 3) were selected as input in the derivation of defect formation energies.

Results are given in Figure 4. Cu vacancies, or V_{Cu}, are constant at 0.348 eV due to Cu-rich conditions, which suggests the likelihood of Cu vacancy formation at synthesis temperatures. Cu-in-Bi anti-site, or Cu_{Bi}, and V_{Bi} dip in energy with increasing Bi and W chemical potentials. Bi_W behaves similarly, though the decrease in $\Delta\mu_W$ past point 3 overshadows the increasing $\Delta\mu_{Bi}$. Other defects remain relatively high in energy and are less likely to form. Overall, a high concentration of Bi and W during synthesis is determined to reduce the likelihood of defect formation, though further study of the effects of such defects on the properties of CBTO is warranted.
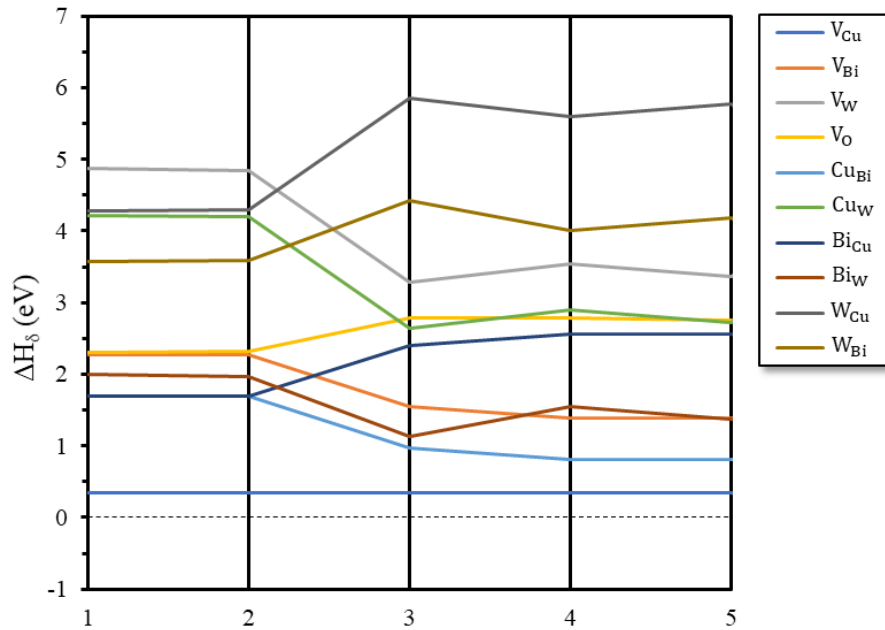
Figure 4. Calculated defect formation enthalpies for vacancies and anti-sites in CBTO. Enthalpies are calculated at conditions bounding the region of interest (Figure 3). Negative enthalpies are understood as spontaneous.

The morphology of the as-synthesized CBTO powders and the 3 times purified CBTO powders were characterized by scanning electron microscopy (SEM, JEOL 7000F, 5 kV). The samples for SEM were prepared by firstly ball milling the CBTO powders for 20 hours. Then, the powders were dispersed in a mixed solvent including 14 mL 1-butanol (99.9%, Sigma Aldrich), 1 mL chloroform (99.5%, Sigma Aldrich) and 1 mL methanol (99.9%, Sigma Aldrich) to make a suspended solution. After 10 min sonication, the suspended solution was drop-casted onto a quartz substrate. According to SEM images (Figure 5), the as-synthesized CBTO powders were composed of crystallites in the form of plates and rounded particles, while the only visible particle morphology in the 3 times purified CBTO powders is rounded particles. According to previous Bi_2WO_6 publications, most of crystalline Bi_2WO_6 particles have plate or flake shapes.[3, 33, 34] Therefore, we believe that the rounded particles are CBTO, and the particle size ranged from 100 nm to 10 μm.
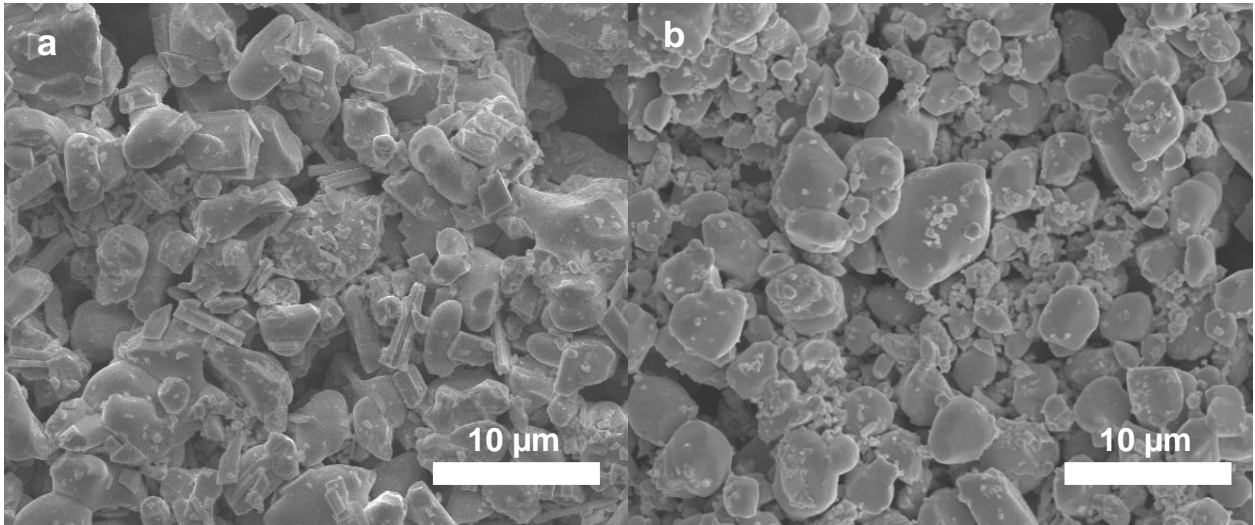
Figure 5. Scanning electron microscopy (SEM) top images of a) as-synthesized CBTO powders and b) 3 times purified CBTO powders.

The wavelength-dependent optical absorption coefficient (α) of 3 times purified CBTO powders was measured using an integrating sphere with white-light illumination from a Xe lamp, and calculated from the measured reflection (R), transmission (T) and effective layer thickness (t) as $\alpha(\lambda)(\%) = -\ln(100\% - R(\lambda)(\%) - T(\lambda)(\%))/t$. The effective layer thickness is

calculated from the measured powder mass (m), sample area (A) and CBTO density (ρ) as t = m / (ρA). The sample for optical measurement was prepared in the same way as the sample for SEM. The optical absorption coefficient vs. wavelength plot in Figure 6a shows that the CBTO has a light absorption edge at 850 nm. The corresponding Tauc plots ((αE)$^{1/r}$ vs. E) of the CBTO with exponent r = 0.5 and r = 2 in Figure 6b and Figure 6c show that the CBTO has a direct band gap of 1.92 eV and an indirect band gap of 1.46 eV. The absorption depth (t_a) of the CBTO powders is calculated by (t_a) (λ) = - ln (1/e - 1) / α (λ), and plotted in Figure 6d. According to Figure 6d, most of the light with wavelength shorter than 650 nm can be absorbed within 100 nm thick CBTO, and most of the light with wavelength shorter than 750 nm can be absorbed within 220 nm thick CBTO. The optical absorption coefficient of 2.1×10^4 cm^{-1} for 1.65 eV photons is one order of magnitude higher than that of Si (1.5×10^3 cm^{-1}) and similar to that of GaAs (2.0×10^4 cm^{-1}) and CdTe (3.0×10^4 cm^{-1}), which indicates that CBTO is a very good light absorber.[35]

Theoretical calculations of the optical absorption coefficient were also carried out in VASP.[36] The frequency dependent absorption coefficient $\alpha(\omega)$ was derived from the extinction coefficient $k(\omega)$ as follows[37]:

$$\alpha_{ii}(\omega) = \frac{2\omega}{c} k_{ii}(\omega) \tag{7a}$$

$$k_{ii}(\omega) = \left\{ \frac{1}{2} \left[\left[\left(\text{Re } \varepsilon_{ii}(\omega) \right)^2 + \left(\text{Im } \varepsilon_{ii}(\omega) \right)^2 \right]^{1/2} - \text{Re } \varepsilon_{ii}(\omega) \right] \right\}^{1/2} \tag{7b}$$

where c is the speed of light, and the real and imaginary parts of $\varepsilon(\omega)$, the dielectric tensor, are calculated from the following[38]:

$$\text{Im } \varepsilon_{ij}(\omega) = \frac{4\pi^2 e^2}{\Omega} \lim_{q \to 0} \frac{1}{q^2} \sum_{c,v,k} 2w_k \delta(\varepsilon_{ck} - \varepsilon_{vk} - \omega) \times \langle u_{ck+e_i q} | u_{ck} \rangle \langle u_{ck+e_j q} | u_{ck} \rangle \tag{8a}$$

$$\text{Re } \varepsilon_{ij}(\omega) = 1 + \frac{2}{\pi} P \int_0^\infty \frac{\text{Im } \varepsilon_{ij}(\omega')\omega'}{\omega'^2 - \omega^2 + i\eta} d\omega' \tag{8b}$$

where Ω is the volume of the primitive cell, q the Bloch wave vector of the incident wave, c and v the conduction and valence states, k the Bloch wave vector used to expand the Kohn-Sham solutions, and w_k the k-point weights. The Dirac delta function ensures energy conservation. Equation 5b is the Kramers-Kronig dispersion relation. Results are given in Figure 7. The light absorption edge and optical direct gap were estimated at 770 nm and 1.73 eV, respectively. The

lower values with respect to experimental results may be due to approximations in the theoretical framework, as well as the purity of CBTO considered in the calculation – the presence of Bi_2WO_6 may play a role in shaping the band edges, and consequently the optical properties.
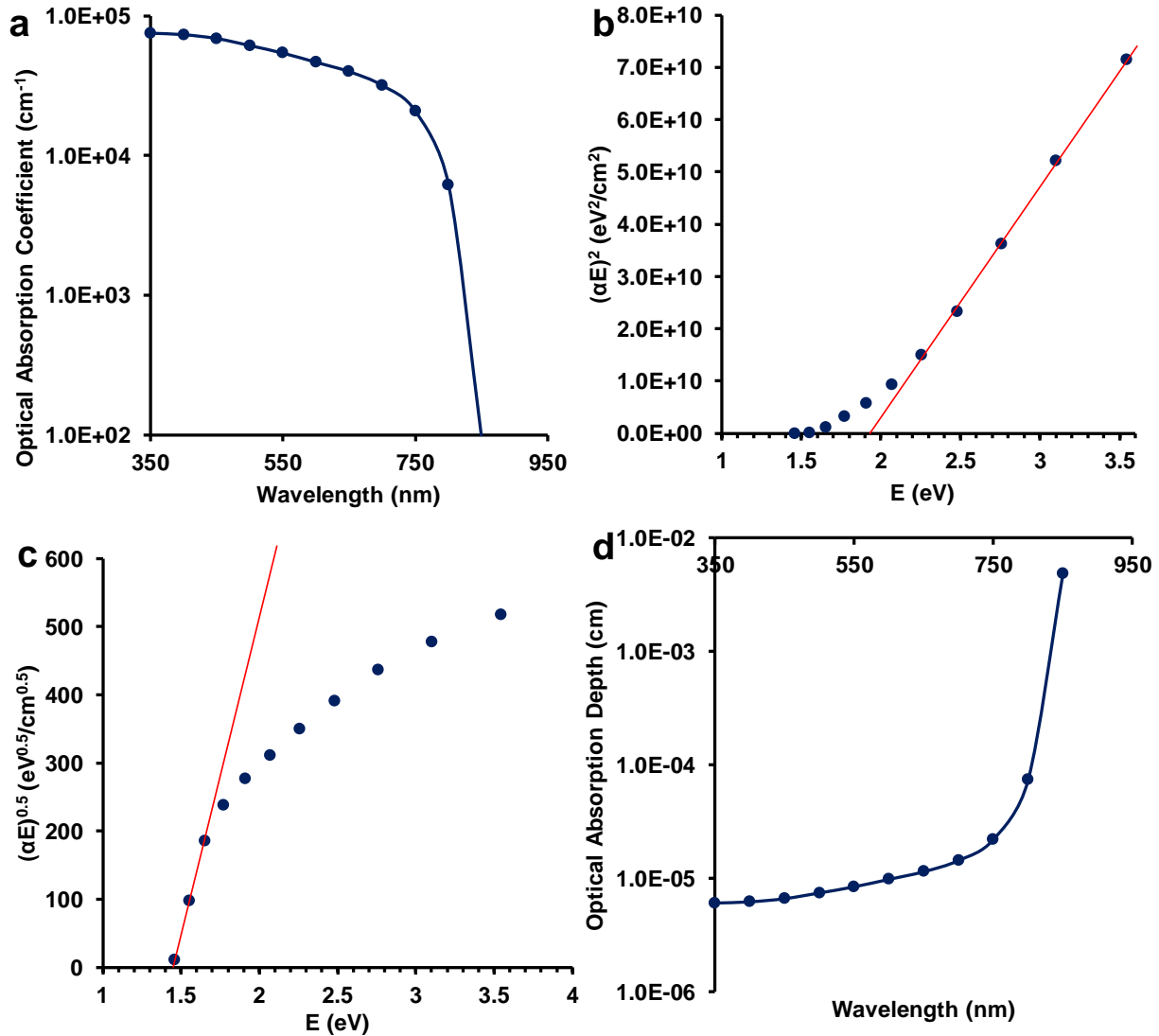
Figure 6. Optical properties of 3 times purified CBTO powders. a) optical absorption coefficient, Tauc plot of 3 times purified CBTO powders with exponent b) r = 0.5 (direct transition) and c) r= 2 (indirect transition), d) optical absorption depth of 3 times purified CBTO powders.
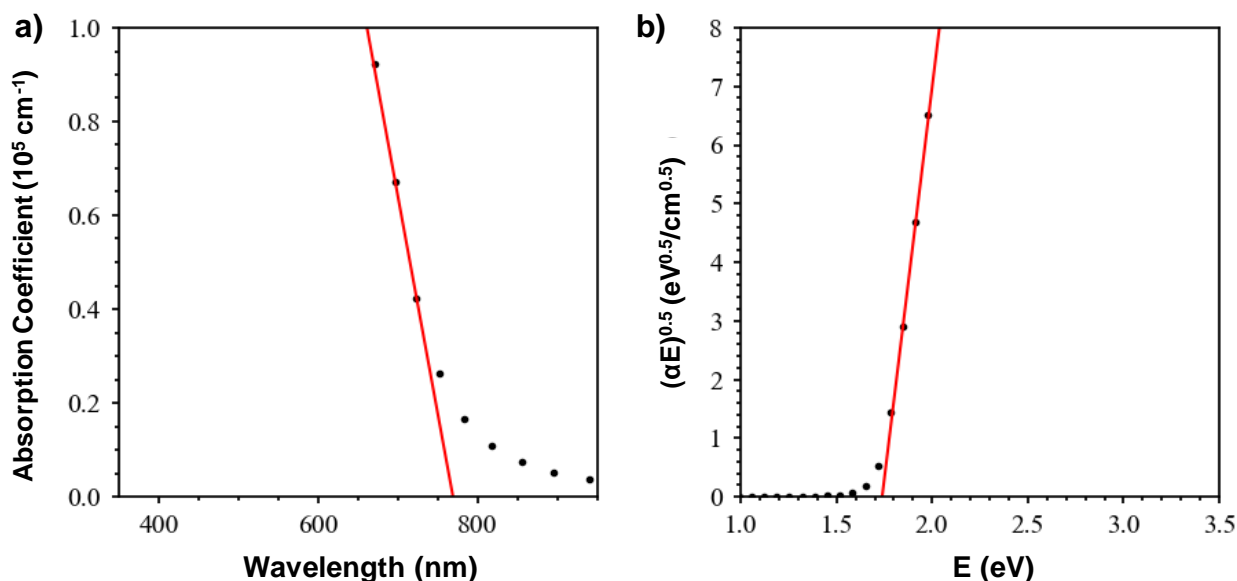
Figure 7. a) Wavelength-dependent absorption coefficient and b) Tauc plot for pristine CBTO. r = 0.5 was used for the Tauc plot reflecting direct transitions.

The photoluminescence (PL) properties of CBTO are consistent with a direct band gap of around 1.9 eV and an indirect band gap of 1.4 eV determined by the optical absorption measurements. The time-integrated PL spectrum of drop-casted 3 times purified CBTO powders on quartz substrate excited by the 533 nm line of a 10 Hz, 4 ns pulsed Nd:YAG laser is shown in Figure 8a. The CBTO sample exhibits a strong PL peak at 655 nm (1.89 eV) and a weak and broad PL peak at 870 nm (1.43 eV). This result indicates that the CBTO has a direct band gap of 1.89 eV and an indirect band of 1.43 eV, which closely matches the result of our light absorption measurement (direct band gap of 1.92 eV and indirect band gap of 1.46 eV).

The 3 times purified CBTO powders were then pelletized by mechanical pressing into a sealed tailored Cu box. The powders were then annealed and sintered in a tube furnace at 600 °C for 9 hours with 500 sccm flow rate of argon to obtain a dense CBTO pellet. The optical image and the SEM images of CBTO pellet are provided in Figure 9 and Figure 10. The CBTO pellet was 450 µm thick with 1 cm^2 area and was used to study CBTO properties further.

The radiative lifetime of photoexcited carriers in CBTO was characterized by the time-resolved photoluminescence (TRPL). TRPL measurement was performed at room temperature with 633 nm excitation pulses produced by an Nd:YAG laser with 20s pulse duration and 19.4

MHz repetition rate. The emission was collected using a time correlated single photon counting system (Becker & Hickl SPC-150) and the signal was integrated using a single photon avalanche photodiode (ID Quantique ID-100-50-std). The time-averaged pulsed laser power (P_{avg}) was measured by a portable silicon photodiode to be 0.5 µW, and the illuminated area of sample was 1 mm^2. The instantaneous pulsed laser intensity (I_{inst}, i.e. the intensity of the laser when it is on) is calculated from P_{avg}, the pulse duration (t_{on}), repetition frequency (F) and illuminated area (A) as $I_{inst} = P_{avg} / (t_{on} \times F \times A)$, and is equal to 128.8 mW/cm^2, which is very close to the light intensity of one-sun (100 mW/cm^2). Thus, the photoexcited carrier radiative lifetime obtained from this TRPL measurement is similar to the lifetime that can be expected under one-sun illumination conditions. 3 times purified CBTO and as-synthesized CBTO pellets were used for the TRPL measurements, and the results are plotted in Figure 8b. The TRPL decay dynamics of 3 times purified CBTO and as-synthesized CBTO emissions in indirect band gap region (800 nm to 1000 nm) were accurately fitted by double exponential decay with time constants of 0.09 ns and 1.12 ns, and 0.09 ns and 1.08 ns, respectively. The 0.09 ns decay time in both of cases are ascribed to internal light reflection within the TRPL system, and the 1.12 ns and 1.08 ns decay time are taken to be the indirect bandgap photoexcited carrier lifetime in 3 times purified CBTO and as-synthesized CBTO, respectively. The indirect bandgap photoexcited carrier lifetime in
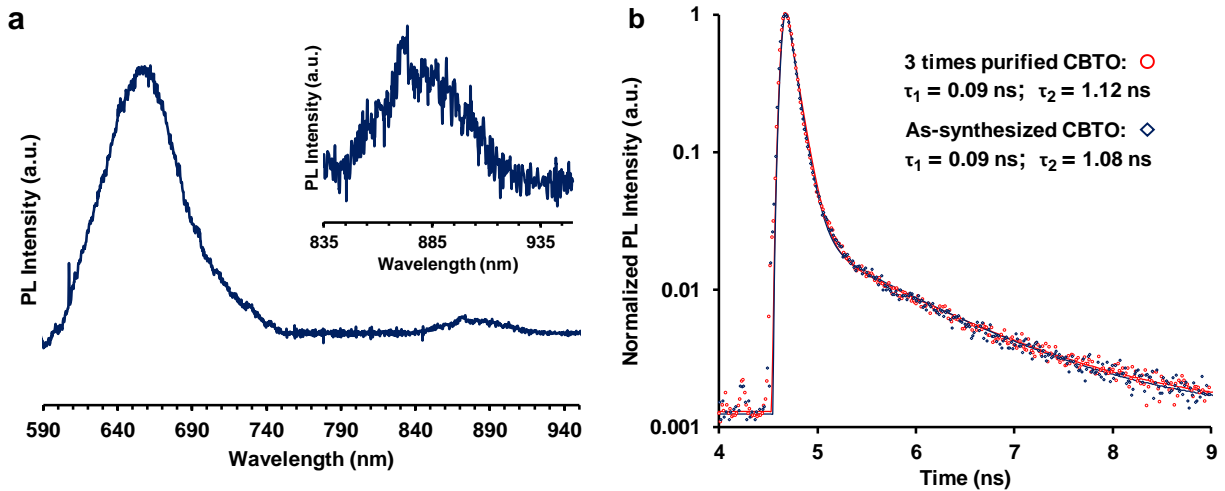
Figure 8. a) Photoluminescence spectrum of 3 times purified CBTO powders. b) Time-resolved PL decay measurements of 3 times purified CBTO (red) and as-synthesized CBTO (blue) pellets emission from 800 nm to 1000 nm, showing double-exponential decay behavior.

CBTO was slightly improved by our purification process. The TRPL measurement results of 3 times purified CBTO and as-synthesized CBTO emissions in direct band gap region (530 nm to 750 nm) are plotted in Figure 11.
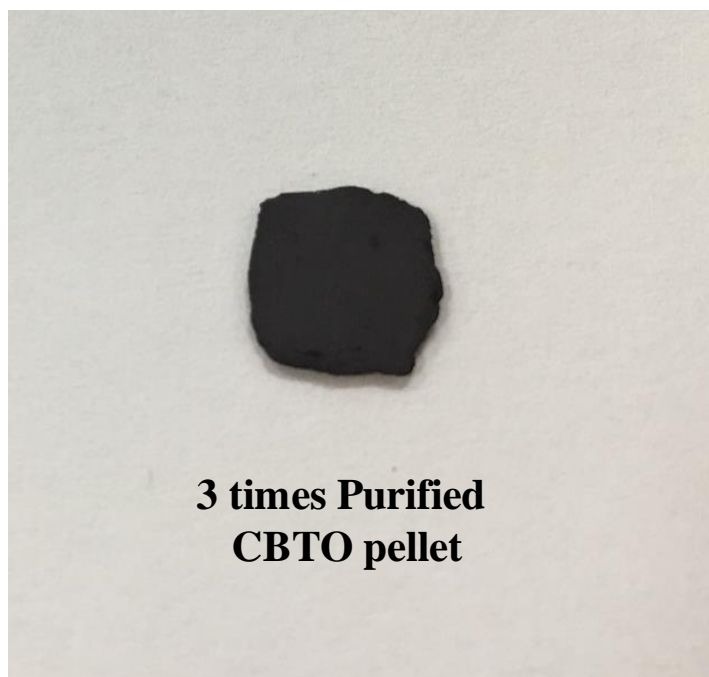
Figure 9. Optical image of 3 times purified CBTO pellet.
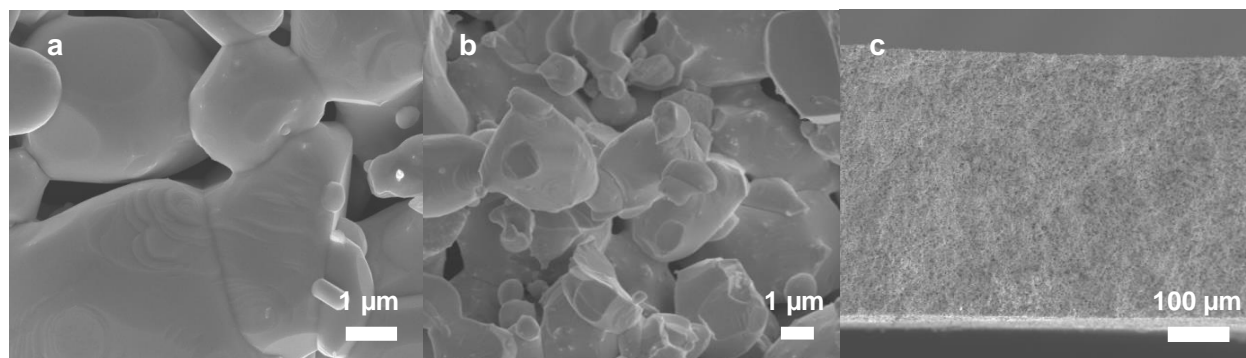
Figure 10. Scanning electron microscopy (SEM) a) top, b) and c) cross-section images of 3 times purified CBTO pellet.
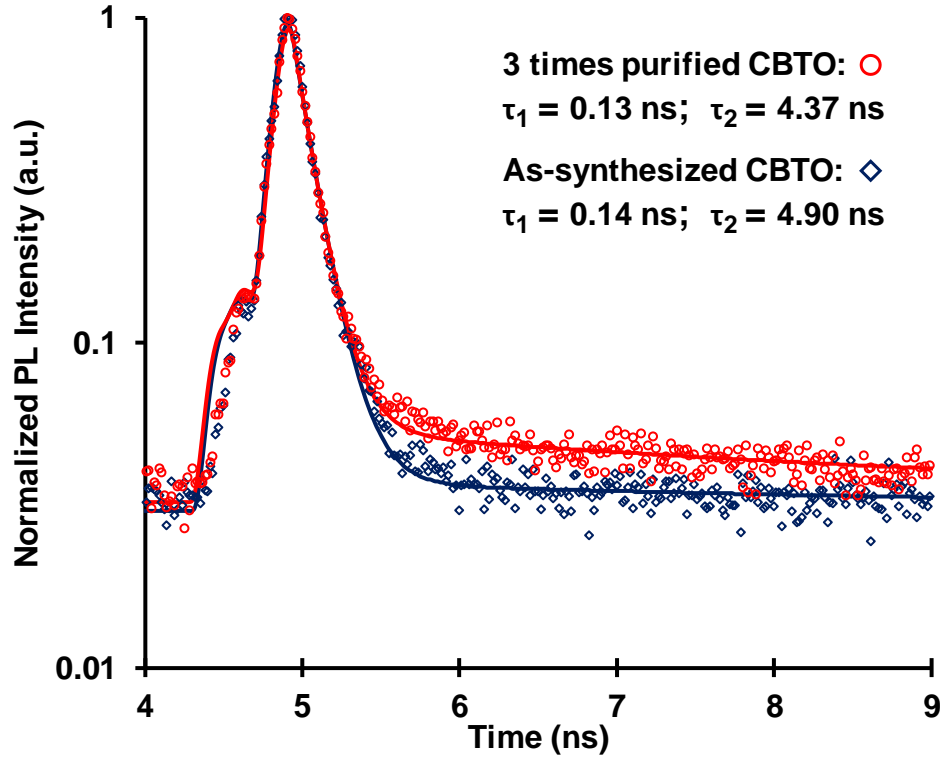
Figure 11. Time-resolved PL decay measurements of 3 times purified CBTO (red) and as-synthesized CBTO (blue) pellets emission from 530 nm to 750 nm, showing double-exponential decay behavior.

The electrical transport properties of CBTO were characterized by Hall Effect measurement (MMR Technologies K2500) using van der Pauw method in a magnetic field of12500 G, with a current of 36.7 nA. The CBTO sample for Hall Effect measurement was prepared by thermal evaporation of 70 nm-thick gold contacts onto the four corners of a square-shaped 3 times purified CBTO pellet. The CBTO pellet has a lateral size of 1 cm x 1 cm with thickness of 450 μm, while the gold contacts at the corners each had a size of ~ 1mm x 1mm and had 7.5 mm center-to-center spacing. The majority carrier type of the CBTO pellet was found to be holes (p-type semiconductor) with carrier density of 3.0×10^{13} cm^{-3} The p-type doping in CBTO is typical of Cu-containing compounds due to Cu vacancies, as in Cu_2O[39], Cu_2S[40], and CZTS[41]. The Hall effect also yields a long-range charge carrier mobility of 0.32 cm^{2}V^{-1}s^{-1}. The low Hall mobility is indicative of the deleterious effect of grain boundaries and defect-associated trap states and suggest that long-range transport occurs by hopping and de-trapping. However, low mobility is somewhat compensated by a relatively low carrier lifetime of 1.12 ns as

determined from TRPL measurements as the photoexcited carrier diffusion length (L) of CBTO is found to be $L = (\tau\mu KT/e)^{0.5}$ ~31.0 nm, where τ is the carrier lifetime, μ is Hall carrier mobility, K is Boltzmann's constant, T is absolute temperature and e is the electron charge. This diffusion length is comparable to that in the successful oxides $BiVO_4$ (~70 nm) and $CuBi_2O_4$ (~50 nm), for instance.[42, 43] However, the optical absorption depth of 100-200 nm is larger than the carrier diffusion length, meaning that heterojunction device architectures involving the coating of thin CBTO layers onto nanostructured charge transport layers or current collectors may be necessary for achieving high-efficiency solar energy conversion.

We then performed chemical characterization of the surface of the 3 times purified CBTO pellets using XPS measurements, and also performed UPS measurements in order to determine the band energies and Fermi level of CBTO. These measurements are crucial for the selection of n-type heterojunction partners with appropriate band energies for pairing with CBTO. Our XPS measurements (Figure 12) indicate the presence of Cu^{2+} based oxide and Bi_2WO_6 impurity phases on the surface of CBTO. Figure 12a reports the XP spectrum of the Cu 2p region, for which prior studies ascribed peaks in the range of 932.7 - 935.7 eV to the Cu 2p 3/2 features from Cu^{2+} ions in Cu-oxide compounds and 931.6 - 932.8 eV to the corresponding features from Cu^{1+} ions in Cu-oxide compounds.[44-47] We ascribe the fitted peaks at 935.62 eV and 934.33 to Cu^{2+}, which may come from impurities such as CuO and $CuWO_4$, and the peak at 932.10 eV to Cu^{1+} from CBTO. For the Bi 4f region in Figure 12b, peaks in the 157.8 - 161.5 eV and peaks in the 163.1 - 166.0 eV range were ascribed to Bi^{3+} 4f 7/2 and 5/2 features, respectively, from Bi-oxide compounds in prior studies.[48, 49] We ascribe fitted peaks at 164.92 eV, 164.41 eV, 159.52 eV and 159.09 eV to Bi^{3+} features, with the two sets of Bi^{3+} peaks likely generated by CBTO and Bi_2WO_6. For the W 4f region in Figure 12c, prior studies ascribed peaks in the 34.5 - 36.6 eV and 37.1 - 39.6 eV range to W^{6+} 4f 7/2 and 5/2 features, respectively, in W-oxide compounds.[50-53] We ascribe the fitted peaks at 37.98 eV, 37.10 eV, 35.80 eV and 34.95 eV to W^{6+} features, with the two sets of peaks likely coming from CBTO and Bi_2WO_6.
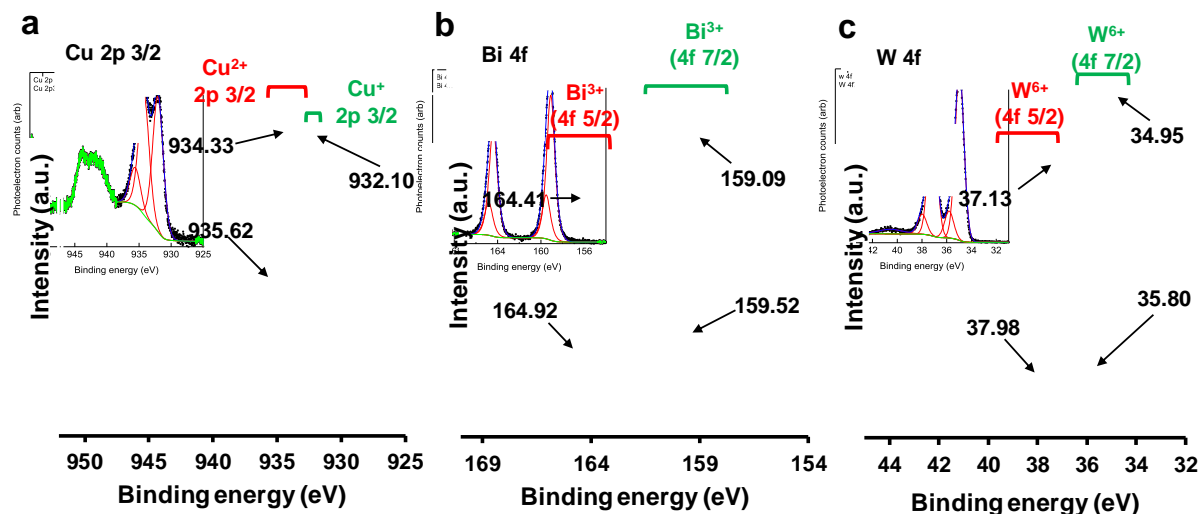
Figure 12. X-ray photoelectron spectra of 3 times purified CBTO pellet. a) Cu 2p XP spectra, b) Bi 4f XP spectra, c) W 4f XP spectra. Red traces correspond the fitted peaks for Cu 2p, Bi 4f and W 4f regions.

The UP spectrum of CBTO (Figure 13) was measured at a sample bias (V_b = -5 V). The work-function of a semiconductor surface (ϕ_s) is given by $\phi_s = h\nu - E_{SE} - V_b$, where $h\nu$ represents the energy of the photons used to probe the band-structure (21.2 eV in our case), E_{SE} is the secondary electron cut-off energy and V_b is the sample bias. The work function of the CBTO was found to be 5.15 eV and the energy of the top of the valence band (VBM) of CBTO was found to be -5.81 eV vs. vacuum (Figure 13c). Based on our UPS results, the VBM is very close to the theoretical calculation value (~ -5.75 eV).[8]

Future CBTO-based photovoltaic devices necessitate depositing CBTO on current collectors such as TCOs. We have evaluated thin films of interconnected CBTO particles on ITO and on quartz by SEM and XRD, and studied the microscopic photoconductivity on interconnected CBTO films on quartz using optical pump-THz probe spectroscopy. For this, 3 times purified CBTO powders were dispersed in a mixed solvent including 14 mL 1-butanol (99.9%, Sigma Aldrich), 1 mL chloroform (99.5%, Sigma Aldrich) and 1 mL methanol (99.9%, Sigma Aldrich) to make a suspension. After 10 min sonication, the suspension was filtered through 2 μm pore size filter papers, and the filtrate was drop cast on quartz and ITO substrates. The samples were then annealed in sealed Cu boxes in a tube furnace at 500 °C for 9 hours with
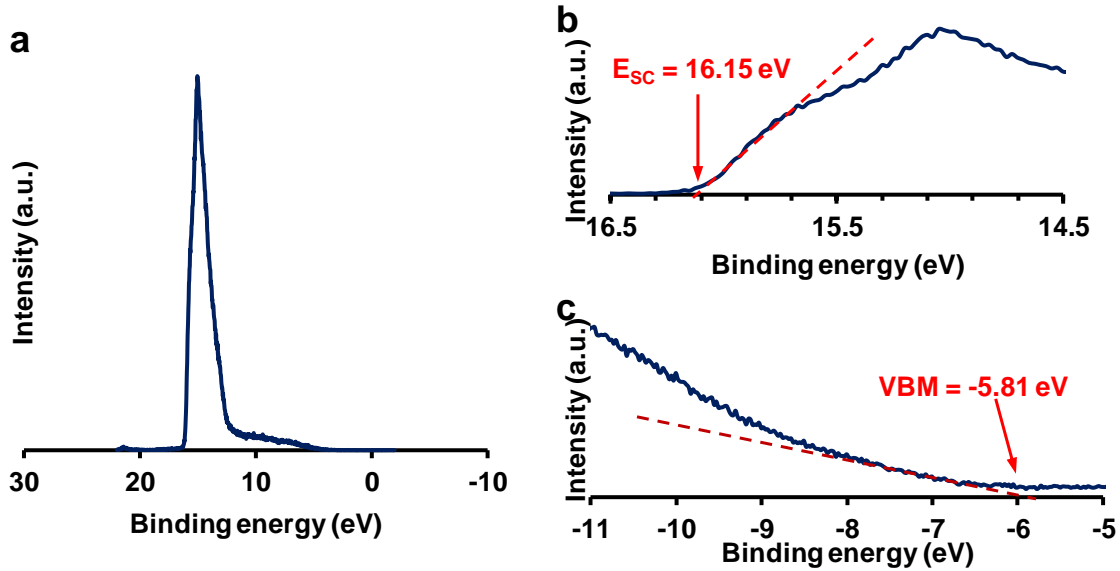
Figure 13. a) ultraviolet photoelectron spectroscopy (UPS) spectrum of 3 times purified CBTO pellet, b) UPS spectrum of 3 times purified CBTO pellet in secondary electron cut off region, c) UPS spectrum of 3 times purified CBTO pellet in the valence band region.

500 sccm flow rate of argon. This annealing temperature of 500 °C is lower than the 600 °C temperature used to synthesize the CBTO particles initially. This temperature reduction is needed to minimize rapid diffusion of Cu into the ITO and glass substrate and subsequent decreaseg in substratetransparency and the formation of impurity phases in CBTO that occur at 600 °C. At lower temperature, we observed no change in appearance of the ITO or quartz substrates and no changes in the XRD patterns(Figure 14). However, SEM (Figure 15) showed that the particle size and inter-connectedness of CBTO particles in the films increased after annealing due to sintering Such changes are likely to improve electrical properties of CBTO films by forming pathways for long-range transport of carriers. To assess the effect of higher inter-particle connectivity in the annealed films composed of connected CBTO particles compared to un-annealed films composed of separated CBTO particles, we have studied transient microscopic THz photoconductivity in the two films on quartz substrates. Optical pump – THz probe spectroscopy (OPTP) is a contact-free technique sensitive to motion of photoexcited carriers on picoseconds time scales[54-59]. With THz photon energy in meV range, OPTP is particularly sensitive to free (mobile) carriers. Unlike the Hall Effect that measures carrier transport over macroscopic distances between the electrical contacts, and can detect slow

carrier transport that proceeds by hopping and carrier trapping and de-trapping, OPTP probes carrier transport over tens and hundreds of nanometers, thus allowing us to follow behavior of photoexcited free carriers within individual CBTO particles.
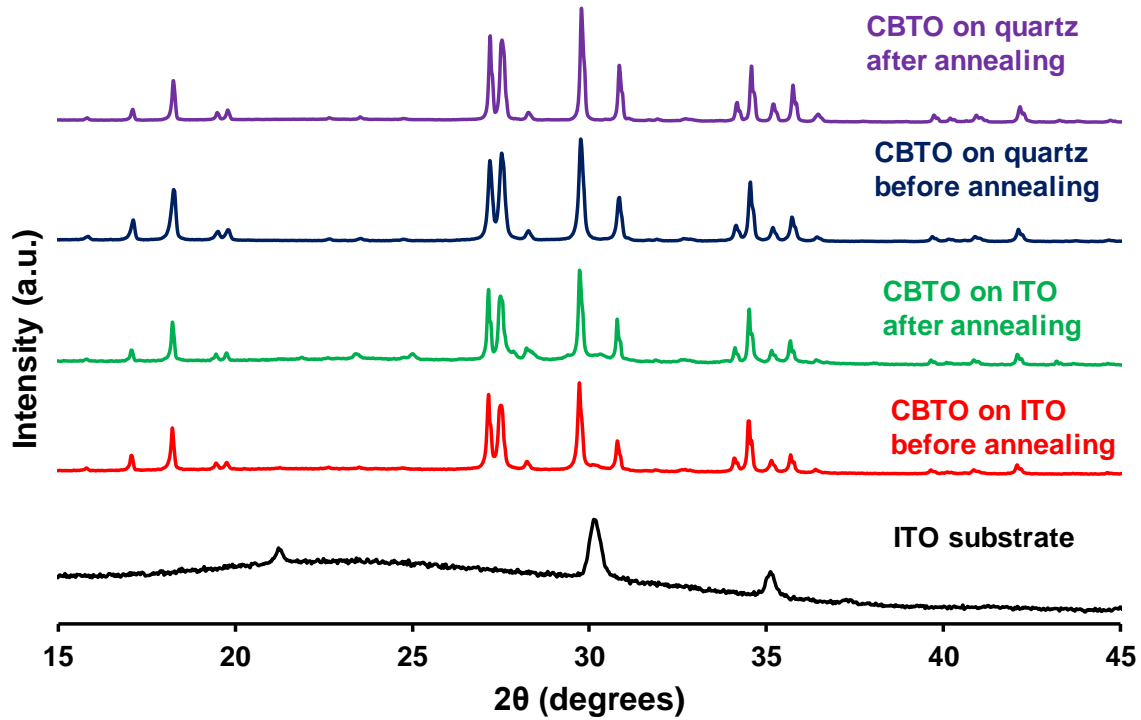
Figure 14. X-ray diffraction of ITO substrate (black), CBTO powders on quartz before (red) and after (green) annealing, CBTO powders on ITO before (blue) and after (purple) annealing.

Annealed and unannealed CBTO films on quartz were excited by ~ 100 fs duration, 400 nm, 0.5 $\mu J/cm^2$ pulses from a regeneratively amplified 1 kHz repetition rate Ti:sapphire laser at normal incidence as described previously[57, 58]. The sample was placed behind a 1.5 mm aperture in the center of a ~ 3 mm 400 nm beam spot to ensure uniform excitation of the studied portion of the film. THz probe pulses were generated using optical rectification of the 800 nm pulses from the same laser source in a 1 mm thick [110] ZnTe crystal and focused onto the sample by off-axis parabolic mirrors. Transmitted THz pulses were detected using electro-optic sampling in the second [110] ZnTe crystal. Figure 16a shows the normalized change in transmission of the
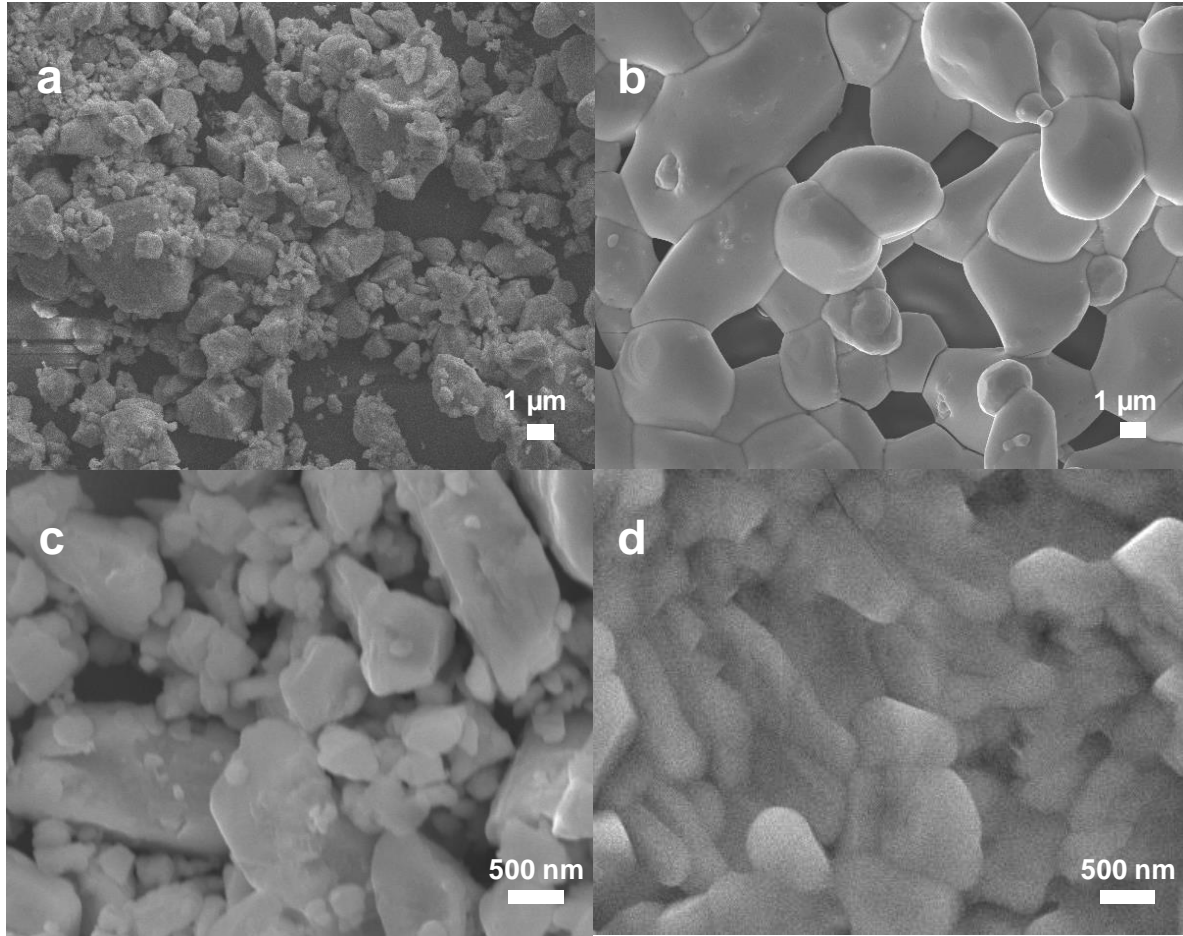
Figure 15. Scanning electron microscopy (SEM) top images of CBTO powders on quartz a) before and b) after annealing, CBTO powders on ITO c) before and d) after annealing.

main peak of the THz probe pulse as a function of 400 nm pump- THz probe delay time. In the limit of low relative pump-induced change in transmission, −ΔT(t) is proportional to the transient pump-induced photoconductivity.[60-62] We find that in both CBTO films, photoconductivity after an initial fast increase due to the photoexcitation, exhibits a bi-exponential decay with one decay time in the picoseconds, and another one in tens of picoseconds. The two decay times represent two different mechanisms of free carrier trapping. Both fast and slow decay components are faster in the un-annealed film, at 1 ps vs 2 ps and 16 ps vs 40 ps as free carriers are more likely to encounter grain boundary and bulk defects in smaller particles of the un-annealed film. The fast decay component is also less pronounced in the un-annealed CBTO film compared to the annealed one. As the major difference between the film is interconnectedness of the CBTO

particles, fastest trapping time may be due to the inter-grain trap states. Here is it important to underscore the difference between the lifetime of free, mobile carriers measured by the OPTP spectroscopy and a much longer radiative lifetime measured by the TRPL spectroscopy. Over the initial picoseconds to tens of picoseconds after optical excitation, THz pulses are absorbed by the free, band-like carriers. As they get trapped at defect states, they can still contribute to slow, trapping and de-trapping as well as hopping transport that can be detected by the Hall effect but not OPTP spectroscopy. Eventually, photoexcited carriers recombine, and the radiative recombination lifetime determined by the TRPL spectroscopy (~ 1 ns) provides a good estimate of the overall lifetime of the photoexcited carriers provided that the non-radiative recombination is not a major contributor. As such, OPTP and TRPL spectroscopy provide complementary information and allow us to re-construct a more complete picture of photoexcited carrier dynamics: photoexcitation generated free, mobile carriers that become trapped in defect states over the initial tens of picoseconds; after that, a small fraction of carriers in shallow trap states continues contributing to the long-range conductivity with a low mobility of 0.32 $cm^2V^{-1}s^{-1}$. To estimate initial mobility of the free carrier population soon after optical injection, we have also measured frequency-resolved complex photoconductivity in both CBTO film on quartz. The complex conductivity is extracted from photoexcitation-induced changes in the amplitude and the phase of the THz pulse waveform transmitted through the sample.[54, 60, 63, 64]Real and imaginary conductivity spectra at 2 ps after excitation of the annealed and un-annealed films are shown in Figs. 6(b) and 6(c), respectively. In general, behavior of free carriers in granular and nanostructures materials can be described by the Drude-Smith model, a phenomenological modification of the Drude model for free carrier conductivity, that accounts for the charge carrier confinement over mesoscopic length scales.[62, 64-72] In the Drude-Smith model, the complex conductivity is given to the first order by

$$\hat{\sigma}(\omega) = \frac{\sigma_0}{1-i\omega\tau_{DS}}\left[1+\frac{c}{1-i\omega\tau_{DS}}\right] \tag{9}$$

where σ_0 is the scaling factor dependent on carrier density and c-parameter characterizes the degree of carrier localization due to the presence of grain boundaries. For c = 0, this model reduces to the Drude model for free carriers and σ_0 becomes the long-range, DC conductivity, while c = −1 describes situations in which carriers are completely localized within individual grains, and the long-range, inter-granular conductivity is completely suppressed. The global fits

of real and imaginary components of the photoconductivity to the Drude-Smith model are shown in Figure 16 (b and c) as lines. We find that annealing CBTO film on quartz that results in the increase in film connectivity observed in SEM leads to a dramatic improvement in long-range mobility of free carriers, as c-parameter goes from nearly -1 to 0. Another parameter in the Drude-Smith model, the effective scattering time τ_{DS} takes into account intrinsic electron-lattice scattering (τ_{int}), collisions with grain boundaries ($\tau_{boundary}$) and carrier-carrier scattering in the case of high excitation densities. [61, 73] We find that τ_{DS} is ~ 80 fs in the annealed film, improved from ~ 60 fs in un-annealed film. Shorter scattering time in an-annealed film composed of
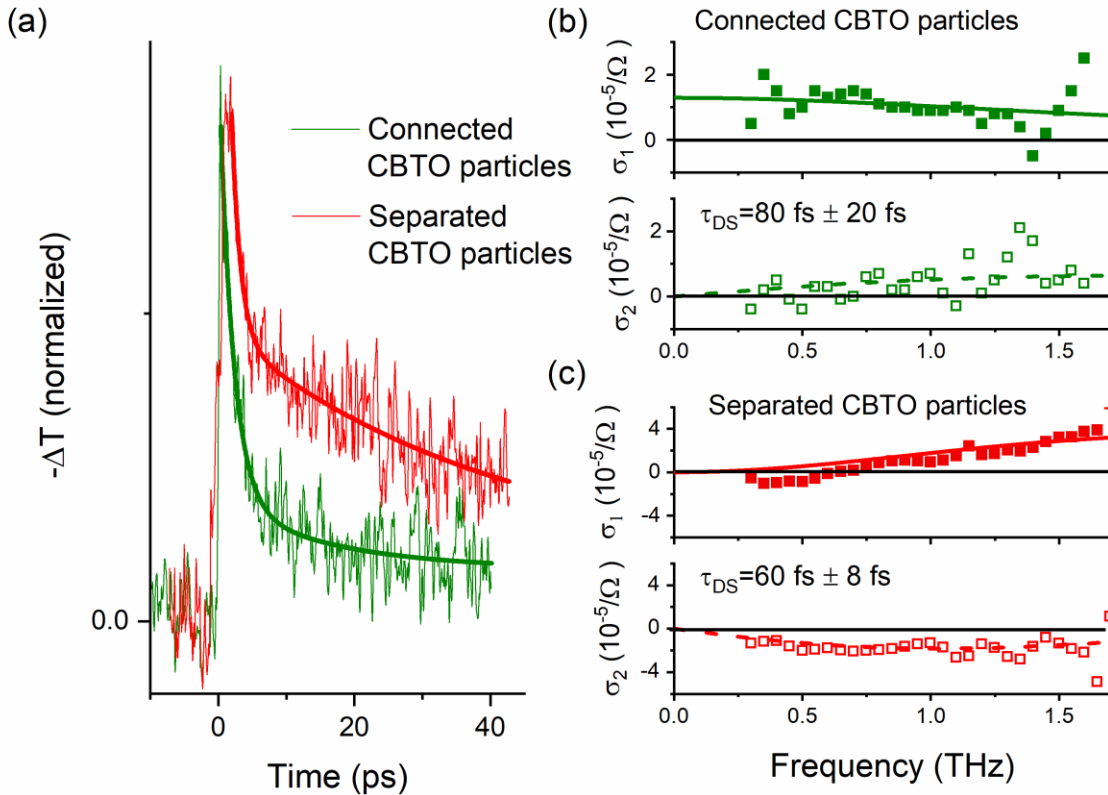
Figure 16. Optical pump – THz probe spectroscopy. (a) Picosecond dynamics of photoconductivity in annealed (connected CBTO particles) and un-annealed (separated CBTO particles) films following photoexcitation with 400nm, ~ 100 fs pulses. (b, c) Real (solid squares) and imaginary (open squares) photoconductivity for two the two films 2 ps after photoexcitation. The lines in (b) and (c) represent a global fit of real and imaginary components of the conductivity to the Drude-Smith model (Eq. 9).

separated CBTO particles likely reflects additional scattering from grain boundaries as well as bulk defects. Finally, we can use τ_{DS} to calculate free carrier mobility (limited to the intra-grain mobility in the case of the un-annealed film), and we find that it ~ 150 cm^{2}v^{-1}s^{-1} for the annealed and ~ 110 cm^{2}v^{-1}s^{-1}. The free, band-like carriers in the annealed film have the long-range the mobility $\mu_{long-range}$=$\frac{e}{m^*}\tau_{DS}(1+c)$ that is almost three orders of magnitude larger that observed Hall mobility have a very short lifetime, picoseconds vs nanoseconds, resulting in the diffusion lengths that are comparable. This improvement in the long-range free carrier transport underscores that annealing films of CBTO particles indeed results in material in which free carrier transport and not only slow hopping and trapping/de-trapping transport can be harnessed.

4.5 Conclusions of CBTO Light Absorbers

In conclusion, the quaternary metal oxide semiconductor CBTO was successfully synthesized by a tailored Cu-rich solid state synthesis method, in which Bi_2O_3, Cu_2O, WO_3 powders were mixed, annealed and reacted in a Cu-rich argon environment. The optical, electrical and photoelectrical properties of CBTO have been measured and studied. To the best of our knowledge, this is the first time CBTO has been successfully synthesized, and is the first study of these properties for CBTO. CBTO is found to be a p-type semiconductor with indirect band gap of 1.46 eV and direct band gap of 1.92 eV, optical absorption coefficient of 2.1 $\times 10^4$ cm^{-1} for 1.65 eV photons, carrier mobility of 0.32 cm^{2}V^{-1}s^{-1} and carrier lifetime of 1.12 ns. These results indicate that CBTO is a promising light absorber. However, the carrier diffusion length of CBTO (31.0 nm) is shorter than the optical absorption depth (100-200 nm), which means that nanostructured heterojunctions with n-type materials such as ZnO will likely be needed to achieve high efficiency solar energy conversion.

Reference

［1］   Cao, D.; Nasori, N.; Wang, Z.; Mi, Y.; Wen, L.; Yang, Y.; Qu, S.; Wang, Z.; Lei, Y. *Journal of Materials Chemistry A* **2016,** 4, (23), 8995-9001.

［2］   Alfaro, S. O.; Martínez-de la Cruz, A. *Applied Catalysis A: General* **2010,** 383, (1), 128-133.

［3］   Jing, L.; Qingzhu, S.; Yan, C.; Ming, S. *IOP Conference Series: Earth and Environmental Science* **2017,** 100, (1), 012030.

［4］   Berglund, S. P.; Abdi, F. F.; Bogdanoff, P.; Chemseddine, A.; Friedrich, D.; van de Krol, R. *Chemistry of Materials* **2016,** 28, (12), 4231-4242.

［5］   Zhu, X.; Guan, Z.; Wang, P.; Zhang, Q.; Dai, Y.; Huang, B. *Chinese Journal of Catalysis* **2018,** 39, (10), 1704-1710.

［6］   Wang, F.; Septina, W.; Chemseddine, A.; Abdi, F. F.; Friedrich, D.; Bogdanoff, P.; van de Krol, R.; Tilley, S. D.; Berglund, S. P. *Journal of the American Chemical Society* **2017,** 139, (42), 15094-15103.

［7］   Li, J.; Griep, M.; Choi, Y.; Chu, D. *Chemical Communications* **2018,** 54, (27), 3331-3334.

［8］   Sarker, P.; Prasher, D.; Gaillard, N.; Huda, M. N. *Journal of Applied Physics* **2013,** 114, (13), 133508.

［9］   Liu, Y.-j.; Cai, R.; Fang, T.; Wu, J.-g.; Wei, A. *Materials Research Bulletin* **2015,** 66, 96-100.

［10］   Peng, Y.; Yan, M.; Chen, Q.-G.; Fan, C.-M.; Zhou, H.-Y.; Xu, A.-W. *Journal of Materials Chemistry A* **2014,** 2, (22), 8517-8524.

［11］   Lee, S. J.; Kim, Y.; Hwang, J.-Y.; Lee, J.-H.; Jung, S.; Park, H.; Cho, S.; Nahm, S.; Yang, W. S.; Kim, H.; Han, S. H. *Scientific Reports* **2017,** 7, 3131.

［12］   Krüger, T. F.; Müller-Buschbaum, H. *Journal of Alloys and Compounds* **1992,** 190, (1), L1-L3.

[13]   Chen, S.; Walsh, A.; Gong, X.-G.; Wei, S.-H. *Advanced Materials* **2013,** 25, (11), 1522-1539.

[14]   Hohenberg, P.; Kohn, W. *Physical Review* **1964,** 136, (3B), B864-B871.

[15]   Sarker, P.; Al-Jassim, M. M.; Huda, M. N. *Journal of Applied Physics* **2015,** 117, (3), 035702.

[16]   Kresse, G.; Furthmüller, J. *Computational Materials Science* **1996,** 6, (1), 15-50.

[17]   Kresse, G.; Furthmüller, J. *Physical Review B* **1996,** 54, (16), 11169-11186.

[18]   Perdew, J. P.; Chevary, J. A.; Vosko, S. H.; Jackson, K. A.; Pederson, M. R.; Singh, D. J.; Fiolhais, C. *Physical Review B* **1992,** 46, (11), 6671-6687.

[19]   Perdew, J. P.; Burke, K.; Ernzerhof, M. *Physical Review Letters* **1996,** 77, (18), 3865-3868.

[20]   Kohn, W.; Sham, L. J. *Physical Review* **1965,** 140, (4A), A1133-A1138.

[21]   Kresse, G.; Joubert, D. *Physical Review B* **1999,** 59, (3), 1758-1775.

[22]   Blöchl, P. E. *Physical Review B* **1994,** 50, (24), 17953-17979.

[23]   Methfessel, M.; Paxton, A. T. *Physical Review B* **1989,** 40, (6), 3616-3621.

[24]   Monkhorst, H. J.; Pack, J. D. *Physical Review B* **1976,** 13, (12), 5188-5192.

[25]   Anisimov, V. I.; Zaanen, J.; Andersen, O. K. *Physical Review B* **1991,** 44, (3), 943-954.

[26]   Anisimov, V. I.; Solovyev, I. V.; Korotin, M. A.; Czyżyk, M. T.; Sawatzky, G. A. *Physical Review B* **1993,** 48, (23), 16929-16934.

[27]   Solovyev, I. V.; Dederichs, P. H.; Anisimov, V. I. *Physical Review B* **1994,** 50, (23), 16861-16871.

［28］   Zhou, F.; Marianetti, C. A.; Cococcioni, M.; Morgan, D.; Ceder, G. *Physical Review B* **2004,** 69, (20), 201101.

［29］   Ganduglia-Pirovano, M. V.; Hofmann, A.; Sauer, J. *Surface Science Reports* **2007,** 62, (6), 219-270.

［30］   Zhang, S. B.; Wei, S.-H.; Zunger, A.; Katayama-Yoshida, H. *Physical Review B* **1998,** 57, (16), 9642-9656.

［31］   Persson, C.; Zhao, Y.-J.; Lany, S.; Zunger, A. *Physical Review B* **2005,** 72, (3), 035211.

［32］   Nagoya, A.; Asahi, R.; Wahl, R.; Kresse, G. *Physical Review B* **2010,** 81, (11), 113202.

［33］   Wang, W.; Guo, M.; Lu, D.; Weimin, W.; Wang, H., *Effect of HNO_3 Concentration on the Morphologies and Properties of Bi_2WO_6 Photocatalyst Synthesized by a Hydrothermal Method*. 2016; Vol. 6, p 75.

［34］   Sun, Z.; Guo, J.; Zhu, S.; Mao, L.; Ma, J.; Zhang, D. *Nanoscale* **2014,** 6, (4), 2186-2193.

［35］   Deng, F.; Cao, H.; Liang, L.; Li, J.; Gao, J.; Zhang, H.; Qin, R.; Liu, C. *Optics Letters* **2015,** 40, (7), 1282-1285.

［36］   Patterson, J.; Bailey, B., Optical Properties of Solids. In *Solid-State Physics: Introduction to the Theory*, Springer Berlin Heidelberg: Berlin, Heidelberg, 2010; pp 545-590.

［37］   Akkus, H.; Mamedov, A. M. *Journal of Physics: Condensed Matter* **2007,** 19, (11), 116207.

［38］   Gajdoš, M.; Hummer, K.; Kresse, G.; Furthmüller, J.; Bechstedt, F. *Physical Review B* **2006,** 73, (4), 045112.

［39］   Nolan, M.; Elliott, S. D. *Physical Chemistry Chemical Physics* **2006,** 8, (45), 5350-5358.

［40］   Nayak, A.; Ohno, T.; Tsuruoka, T.; Terabe, K.; Hasegawa, T.; Gimzewski, J. K.; Aono, M. *Advanced Functional Materials* **2012,** 22, (17), 3606-3613.

［41］ Han, D.; Sun, Y. Y.; Bang, J.; Zhang, Y. Y.; Sun, H.-B.; Li, X.-B.; Zhang, S. B. *Physical Review B* **2013,** 87, (15), 155206.

［42］ Abdi, F. F.; Savenije, T. J.; May, M. M.; Dam, B.; van de Krol, R. *The Journal of Physical Chemistry Letters* **2013,** 4, (16), 2752-2757.

［43］ Giménez, S.; Bisquert, J., *Photoelectrochemical solar fuel production: From basic principles to advanced devices*. 2016; p 1-559.

［44］ Haber, J.; Machej, T.; Ungier, L.; Ziółkowski, J. *Journal of Solid State Chemistry* **1978,** 25, (3), 207-218.

［45］ Ghijsen, J.; Tjeng, L. H.; van Elp, J.; Eskes, H.; Westerink, J.; Sawatzky, G. A.; Czyzyk, M. T. *Physical Review B* **1988,** 38, (16), 11322-11330.

［46］ Moretti, G.; Fierro, G.; Lo Jacono, M.; Porta, P. *Surface and Interface Analysis* **1989,** 14, (6‐7), 325-336.

［47］ Sacher, E.; Klemberg-Sapieha, J. E.; Cambron, A.; Okoniewski, A.; Yelon, A. *Journal of Electron Spectroscopy and Related Phenomena* **1989,** 48, (2), C7-C12.

［48］ Kazushige, O.; Kenji, Y.; Masatoshi, A.; Yoshiaki, T.; Hisao, H. *Japanese Journal of Applied Physics* **1992,** 31, (7B), L953.

［49］ Ismail, F. M.; Hanafi Z, M., Some Physico-Chemical Properties of Bismuth Chalcogenides x-Ray Photoelectron and Diffuse Reflectance Spectra. In *Zeitschrift für Physikalische Chemie*, 1986; Vol. 267O, p 667.

［50］ Shi, J.; Allara, D. L. *Langmuir* **1996,** 12, (21), 5099-5108.

［51］ McGuire, G. E.; Schweitzer, G. K.; Carlson, T. A. *Inorganic Chemistry* **1973,** 12, (10), 2450-2453.

［52］ Chowdari, B. V. R.; Tan, K. L.; Chia, W. T. *Solid State Ionics* **1992,** 53-56, 1172-1178.

［53］ Halada, G. P.; Clayton, C. R. *Journal of Vacuum Science & Technology A* **1993,** 11, (4), 2342-2347.

[54]   Jepsen, P. U.; Cooke, D. G.; Koch, M. *Laser & Photonics Reviews* **2011,** 5, (1), 124-166.

[55]   Baxter, J. B.; Richter, C.; Schmuttenmaer, C. A. *Annual Review of Physical Chemistry, Vol 65* **2014,** 65, 423-447.

[56]   Regan, K. P.; Koenigsmann, C.; Sheehan, S. W.; Konezny, S. J.; Schmuttenmaer, C. A. *Journal of Physical Chemistry C* **2016,** 120, (27), 14926-14933.

[57]   Butler, K. T.; Dringoli, B. J.; Zhou, L.; Rao, P. M.; Walsh, A.; Titova, L. V. *Journal of Materials Chemistry A* **2016,** 4, (47), 18516-18523.

[58]   Kushnir, K.; Chen, K.; Zhou, L.; Giri, B.; Grimm, R. L.; Rao, P. M.; Titova, L. V. *The Journal of Physical Chemistry C* **2018,** 122, (22), 11682-11688.

[59]   Titova, L. V.; Cocker, T. L.; Cooke, D. G.; Wang, X.; Meldrum, A.; Hegmann, F. A. *Physical Review B* **2011,** 83, (15).

[60]   Hegmann, F. A.; Ostroverkhova, O.; Cooke, D. G., Probing Organic Semiconductors with Terahertz Pulses. In *Photophysics of Molecular Materials*, Wiley-VCH Verlag GmbH & Co. KGaA: 2006; pp 367-428.

[61]   Titova, L. V.; Cocker, T. L.; Cooke, D. G.; Wang, X.; Meldrum, A.; Hegmann, F. A. *Physical Review B* **2011,** 83, (8), 085403.

[62]   Schmuttenmaer, C. A. *Chemical Reviews* **2004,** 104, (4), 1759-1780.

[63]   Baxter, J. B.; Guglietta, G. W. *Anal. Chem.* **2011,** 83, (12), 4342-68.

[64]   Baxter, J. B.; Schmuttenmaer, C. A. *Journal of Physical Chemistry B* **2006,** 110, (50), 25229-25239.

[65]   Smith, N. *Physical Review B* **2001,** 64, (15).

[66]   Mics, Z.; D'Angio, A.; Jensen, S. A.; Bonn, M.; Turchinovich, D. *Appl. Phys. Lett.* **2013,** 102, (23), 231120.

［67］   Knab, J. R.; Lu, X.; Vallejo, F. A.; Kumar, G.; Murphy, T. E.; Hayden, L. M. *Opt. Mater. Express* **2014,** 4, (2), 300-307.

［68］   Cocker, T. L.; Baillie, D.; Buruma, M.; Titova, L. V.; Sydora, R. D.; Marsiglio, F.; Hegmann, F. A. *Physical Review B* **2017,** 96, (20), 205439.

［69］   Parkinson, P.; Lloyd-Hughes, J.; Gao, Q.; Tan, H. H.; Jagadish, C.; Johnston, M. B.; Herz, L. M. *Nano Lett.* **2007,** 7, (7), 2162-2165.

［70］   Cooke, D. G.; Meldrum, A.; Uhd Jepsen, P. *Appl. Phys. Lett.* **2012,** 101, (21), 211107.

［71］   Zhou, Q.-l.; Shi, Y.; Jin, B.; Zhang, C. *Appl. Phys. Lett.* **2008,** 93, (10), 102103.

［72］   Alberding, B. G.; DeSario, P. A.; So, C. R.; Dunkelberger, A. D.; Rolison, D. R.; Owrutsky, J. C.; Heilweil, E. J. *Journal of Physical Chemistry C* **2017,** 121, (7), 4037-4044.

［73］   Turner, G. M.; Beard, M. C.; Schmuttenmaer, C. A. *J. Phys. Chem. B* **2002,** 106, (45), 11716-11719.

Chapter 5 Publications to Date and Planned Publications

5.1 Publications to Date:

1. *L. Zhou, C. Zhao, B. Giri, P. Allen, X. Xu, H. Joshi, Y. Fan, L. V. Titova and P. M. Rao, "High Light Absorption and Charge Separation Efficiency at Low Applied Voltage from Sb-Doped SnO2/BiVO4 Core/Shell NanorodArray Photoanodes", Nano Letters, 16 (6), 3463–3474, 2016.* **(Impact factor: 12.080 (2017). Total citations to date: 61)**

2. *L. Zhou, Y. Yang, J. Zhang, and P. M. Rao, "Photoanode with Enhanced Performance Achieved by Coating BiVO4 onto ZnO-Templated Sb-Doped SnO2 Nanotube Scaffold", ACS Applied Materials & Interfaces, 9 (13), 11356– 11362, 2017.* **(Impact factor: 8.097 (2017) Total citations to date: 16)**

3. *B. Lamm, L. Zhou, P. Rao, M. Stefik, ALD of Space-Efficient SnO2 Underlayers for BiVO4 Host-Guest Architectures for Photoassisted Water Splitting. ChemSusChem 2018.* **(Impact factor: 7.411 (2017))**

4. *K. T. Butler, B. J. Dringoli, L. Zhou, P. M. Rao, A. Walsh and L. V. Titova, "Ultrafast carrier dynamics in BiVO4 thin film photoanode material: interplay between free carriers, trapped carriers and low-frequency lattice vibrations", Journal of Materials Chemistry A, 4, 18516, 2016* **(Impact factor: 9.931 (2017) Total citations to date: 15)**

5. *Z. Zhu, P. Sarker, C. Zhao, L. Zhou, R. L. Grimm, M. N. Huda and P. M. Rao, "Photoelectrochemical Properties and Behavior of α-SnWO4 Photoanodes Synthesized by Hydrothermal Conversion of WO3 films", ACS Applied Materials & Interfaces, 9 (2), 1459−1470, 2017.* **(Impact factor: 8.097 (2017) Total citations to date: 6)**

6. *P. Allen, L. Cai, L. Zhou, C. Zhao and P. M. Rao, "Rapid Synthesis of Thin and Long Mo17O47 Nanowire-Arrays in an Oxygen Deficient Flame", Scientific Reports, 6, 27832, 2016* **(Impact factor: 4.122 (2017) Total citations to date: 4)**

7. *K. Kushnir, K. Chen, L. Zhou, B. Giri, R. L. Grimm, P. M. Rao, and L. V. Titova: 'Dynamics of Photoexcited Carriers in Polycrystalline PbS and at PbS/ZnO Heterojunctions: Influence of Grain Boundaries and Interfaces', The Journal of Physical Chemistry C, 2018, 122, (22), pp. 11682-11688* **(Impact factor: 4.484 (2017) Total citations to date: 1)**

8. *Z. Zhu, S. K. Iyemperumal, K. Kushnir, A. D. Carl, L. Zhou, D. R. Brodeur, R. L. Grimm, L. V. Titova, N. A. Deskins and P. M. Rao, "Enhancing the solar energy conversion efficiency of*

solution-deposited Bi2S3 thin films by annealing in sulfur vapor at elevated temperature", Sustainable Energy & Fuels, 1, 2134-2144, 2017 **(Impact factor: NA (2017) Total citations to date: 4)**

9. *Caicai, Y.; Yang, Y.; Jing, Z.; **Lite, Z**.; Tao, Y.; Binod, G.; Sindy Paola Palma, S.; Hao, F.; Apoorva, S.; Arjan, G.; Pratap Mahesh, R., Materials Research Express 2019.* **(Impact factor: 1.151 (2017))**

5.2 Planned Publications:

1. *Synthesis of Promising Metal Oxide Light Absorber CuBiW$_2$O$_8$ (CBTO) by Cu-Rich Solid State Method and Measurement of Optoelectronic Properties. **Lite Zhou**, Binod Giri, Maryam Masroor, Guangjiang Li, Edan Bainglass, Alexander Carl, Ronald L. Grimm, Muhammad N. Huda, Lyubov V Titova, and Pratap M. Rao* (ready to submit to Journal of Materials Chemistry A)

Chapter 6 Conclusions and Future Recommendations

6.1 Summary and Discussion

Novel Sb:SnO$_2$ nanorod and nanotube electron collectors have been synthesized to couple with promising light absorber BiVO$_4$ to simultaneously improve light absorption efficiency and charge separation efficiency in BiVO$_4$ PEC cells and PV cells. In addition, a new promising quaternary metal oxide semiconductor CBTO was successfully synthesized by a tailored Cu-rich solid state synthesis method and its optoelectronic properties have been investigated.

This work set up several records in BiVO$_4$-based photoanodes and PV cells. The performance of Sb:SnO$_2$ nanotubes/BiVO$_4$ photoanode achieved a new record for the product of light absorption and charge separation efficiencies ($\eta_{abs} \times \eta_{sep}$) of ~ 57.3% and 58.5% under front- and back-side illumination at 0.6 V$_{RHE}$. Sb:SnO$_2$/BiVO$_4$ liquid junction PV cell achieved a new record for the solar conversion efficiency of 1.22%.

The novel Sb:SnO$_2$ nanorod electron collector have been proven to have good conductivity and high transparency, and the novel Sb:SnO$_2$ nanotube electron collector has a controllable length and packing density. Both of them can possibly be used widely to improve PEC and PV performance of other semiconducting materials which have similar optoelectronic properties as BiVO$_4$.

CBTO is found to be a p-type semiconductor with indirect band gap of 1.46 eV and it is capable to absorb up to 850 nm wavelength light. CBTO has optical absorption coefficient of 2.1 $\times 10^4$ cm^{-1} for 1.65 eV photons, carrier mobility of 0.32 cm^{2}V^{-1}s^{-1} and carrier lifetime of 1.12 ns. The material cost of CBTO is potentially low, and the synthesis process of CBTO is easy and carried out at relatively low temperature (600 °C). All of these results indicate that CBTO is a promising light absorber.

6.2 Future Recommendations

6.2.1 Recommendation for BiVO₄ Photoanodes

The influence of $Sb:SnO_2$ nanotube length on the PEC performance shows that under back-side illumination, as the growth time increased to get longer nanotubes, the PEC performance of the $Sb:SnO_2/BiVO_4$ nanotube photoanode decreased, which indicated the interfacial recombination became the main factor for limiting charge separation. It will be interesting to study charge transfer and interfacial recombination at $Sb:SnO_2/BiVO_4$ interface.

6.2.2 Recommendation for BiVO₄ PV Cells

The solar conversion efficiency of liquid junction $BiVO_4$ PV cells can be improved by using a redox couple electrolyte with more positive redox potential.[1] In order to obtain high efficiency $BiVO_4$ PV cells, more efforts are necessary to make to find a redox couple electrolyte that not only have more positive redox potential, but also compatible to $BiVO_4$.

6.2.3 Recommendation for CBTO Light Absorbers

Firstly, even though the purity of CBTO light absorber can be improved by repeating the ball milling mixing and heat treatment processes, the small amount of the BiW_2O_6 and CuO impurities which can not be eliminated from the purification process can still cause carrier recombination and limit the solar conversion efficiency. The synthesis and/or the purification processes of CBTO light absorber still need to be modified to get higher purity of CBTO. Secondly, the carrier diffusion length of CBTO (31.0 nm) is much shorter than the optical absorption depth (100-200 nm), in order to achieve high charge separation efficiency and high light absorption efficiency at the same time, a nanostructured n-type semiconductor or hole collector scaffold with suitable band position may be necessary to couple with CBTO. Thirdly, Considering the high volatility and mobility of Cu at high temperature in CBTO, interdiffusion may happen after coupling CBTO and scaffold. Therefore, to obtain an efficient CBTO solar cell, a low temperature deposition technique is needed to couple CBTO with the scaffold.

Reference

［1］   Xiang, C.; Kimball, G. M.; Grimm, R. L.; Brunschwig, B. S.; Atwater, H. A.; Lewis, N. S. *Energy & Environmental Science* **2011,** 4, (4), 1311-1318.